1-1-2013

Interrogation of Single Asperity Electrical Contacts Using atomic force Microscopy With Application to Nems Logic Switches

Graham E. Wabiszewski
University of Pennsylvania, gwabiszewski@gmail.com

Recommended Citation

Wabiszewski, Graham E., "Interrogation of Single Asperity Electrical Contacts Using atomic force Microscopy With Application to Nems Logic Switches" (2013). *Publicly Accessible Penn Dissertations*. 935.
http://repository.upenn.edu/edissertations/935

Interrogation of Single Asperity Electrical Contacts Using atomic force Microscopy With Application to Nems Logic Switches

Abstract

Energy consumption by computers and electronics is currently 15% of worldwide energy output, and growing. Aggressive scaling of the fully-electronic transistor, which is the fundamental computational element of these devices, has led to significant and immutable energy losses. Ohmic nanoelectromechanical systems (NEMS) logic switches have been recognized as a potential transistor replacement technology with projected energy savings of one to three orders of magnitude over traditional, fully-electronic transistors. However, the use of conventional, adhesive contact materials (i.e. metals) in NEMS switches electrical contacts leads to permanent device seizure or the formation of insulating tribofilms that inhibits commercialization of this technology. Of critical need is a method to efficiently identify and interrogate low adhesion, chemically stable electrical contact material pairs under conditions and scales relevant to NEMS logic switch contacts. This thesis presents the development of two electrical contact testing methods based on atomic force microscopy (AFM) to interrogate electrical contact materials under contact forces and environments representative of NEMS logic switch operating conditions. AFM was used to mimic the interaction of Pt/Pt NEMS logic switch electrical interfaces for up to two billion contact cycles in laboratory timeframes. Contact resistance before cycling significantly exceeded theoretical predictions for clean Pt/Pt interfaces due to adsorbed contaminant films and increased up to six orders of magnitude due to cycling-induced insulating tribopolymer growth. Sliding of the contact with microscale amplitudes lead to significant recovery of conductivity through displacement of the insulating films. Based on this observation, AFM was then used to investigate the role of load, shear, electrical bias, and environment on the electrical robustness of Pt/nitrogen-incorporated ultrananocrystalline diamond (N-UNCD) and Pt/Pt interfaces. N-UNCD was selected because similar diamond films have demonstrated low adhesion, chemical inertness, and compatibility with NEMS logic device fabrication. Pt/N-UNCD interfaces subjected to low loads during sliding demonstrated significant increases in contact resistance due to insulating film formation that was not observed at larger loads. Taken in concert, these finding demonstrate the capability of AFM to investigate nanoscale electrical contact phenomena without the need for time-consuming and expensive integration of unproven materials in NEMS logic switches.

Degree Type
Dissertation

Degree Name
Doctor of Philosophy (PhD)

Graduate Group
Mechanical Engineering & Applied Mechanics

First Advisor
Robert W. Carpick

Second Advisor
Gianluca Piazza

Keywords
Atomic force microscopy, Electrical contacts, Nanoelectromechanical systems, Tribology, Tribopolymer

Subject Categories
Electrical and Electronics | Mechanical Engineering

INTERROGATION OF SINGLE ASPERITY ELECTRICAL CONTACTS USING ATOMIC FORCE MICROSCOPY WITH APPLICATION TO NEMS LOGIC SWITCHES

Graham E. Wabiszewski

A DISSERTATION

in

Mechanical Engineering and Applied Mechanics

Presented to the Faculties of the University of Pennsylvania

in

Partial Fulfillment of the Requirements for the

Degree of Doctor of Philosophy

2013

Supervisor of Dissertation	Co-supervisor of Dissertation
Robert W. Carpick, Professor and Chair of Mechanical Engineering and Applied Mechanics	Gianluca Piazza, Associate Professor of Electrical and Computer Engineering, Carnegie Mellon University

Graduate Group Chairperson

Jennifer R. Lukes, Associate Professor and Graduate Group Chair of Mechanical Engineering and Applied Mechanics

Dissertation Committee:

John L. Bassani, Richard H. and S.L. Gabel Professor of Mechanical Engineering and Applied Mechanics

Robert W. Carpick, Professor and Chair of Mechanical Engineering and Applied Mechanics

Daniel S. Gianola, Skirkanich Assistant Professor of Materials Science and Engineering

Gianluca Piazza, Associate Professor of Electrical and Computer Engineering, Carnegie Mellon University

INTERROGATION OF SINGLE ASPERITY ELECTRICAL CONTACTS USING ATOMIC FORCE MICROSCOPY WITH APPLICATION TO NEMS LOGIC SWITCHES

To my parents, grandparents, brother, and Christine. Thank you for your help and support.

ACKNOWLEDGMENTS

Thank you, first and foremost, to my advisors, Professor Robert W. Carpick and Professor Gianluca Piazza. Your guidance, patience, and direction have helped me immensely over the course of my graduate education and research.

Thank you, Rob, for taking me under your wing. You have been a great friend, mentor, and advocate. You have shown me, through example, how to be a scientist and engineer. Your positivity and love for engineering is infectious. I am forever indebted to you.

I would also like to thank my committee members, Professor John Bassani and Professor Daniel Gianola, for their time, input, and help over the course of my graduate studies.

While the work presented in this thesis bears the name of a single author, none of it would have been possible without the support and help of many individuals. I would like to thank Dr. Augusto Tazzoli for his help in creating the logarithmic current amplifier that enabled the majority of the work presented here. I would like to thank Dr. Andrew Konicek for his PEEM work, revisions on my written work, and endless encouragement. I thank Dr. Anirudha Sumant for the growth of N-UNCD and useful discussions. I thank Frank Streller for his consistent review of my work, help with fabrication and instrumentation, and useful discussions. I would like to thank Dr. Filippo Mangolini for his help with XPS measurements and guidance. I thank Dr. Tevis Jacobs, Alex Goodman, and Peter Rockett for their work on the design and fabrication of the TEM multiprobe holder. I also thank Dr. Nipun Sinha for performing many Pt and Au film depositions that enabled the development of the methodologies presented in this thesis.

Many other individuals have contributed heavily to the work described in this thesis. I would like to thank Dr. Vahid Vahdat, Dr. Erin Flater, Dr. David Grierson, Dr. Qunyang Li, and Dr. Christian Greiner for helpful, useful, and interesting discussions. I would like to thank Peter Szczesniak for his willingness to machine anything in a pinch. I thank Maryeileen Banford Griffith, Olivia Brubaker, Susan Waddington Pilder, and Desirae Johnson for their help with administrative requirements during my graduate school process.

Funding from DARPA grant MIPR 06-W238 for the development of low power piezoactuated NEMS logic, phase III program is acknowledged.

Use of the University of Pennsylvania Nano/Bio Interface instrumentation is acknowledged.

Use of the facilities of the Pennsylvania Regional Nanotechnology Facility is acknowledged.

Use of the Center for Nanoscale Materials was supported by the U.S. Department of Energy, Office of Science, Office of Basic Energy Sciences, under Contract No. DE-AC02-06CH11357.

ABSTRACT

INTERROGATION OF SINGLE ASPERITY ELECTRICAL CONTACTS USING ATOMIC FORCE MICROSCOPY WITH APPLICATION TO NEMS LOGIC SWITCHES

Graham E. Wabiszewski

Professor Robert W. Carpick

Professor Gianluca Piazza

Energy consumption by computers and electronics is currently 15% of worldwide energy output, and growing. Aggressive scaling of the fully-electronic transistor, which is the fundamental computational element of these devices, has led to significant and immutable energy losses. Ohmic nanoelectromechanical systems (NEMS) logic switches have been recognized as a potential transistor replacement technology with projected energy savings of one to three orders of magnitude over traditional, fully-electronic transistors. However, the use of conventional, adhesive contact materials (*i*.*e*. metals) in NEMS switches electrical contacts leads to permanent device seizure or the formation of insulating tribofilms that inhibits commercialization of this technology. Of critical need is a method to efficiently identify and interrogate low adhesion, chemically stable electrical contact material pairs under conditions and scales relevant to NEMS logic switch contacts. This thesis presents the development of two electrical contact testing methods based on atomic force microscopy (AFM) to interrogate electrical contact materials under contact forces and environments representative of NEMS logic switch operating conditions. AFM was used to mimic the interaction of Pt/Pt NEMS logic switch electrical interfaces for up to two billion contact cycles in laboratory timeframes. Contact resistance before cycling significantly exceeded theoretical predictions for clean Pt/Pt interfaces due to adsorbed contaminant films and increased up to six orders of magnitude due to cycling-induced insulating tribopolymer growth. Sliding of the contact with microscale amplitudes lead to significant recovery of conductivity through displacement of the insulating films. Based on this observation, AFM was then used to investigate the role of load, shear, electrical bias, and environment on the electrical robustness of Pt/nitrogen-incorporated ultrananocrystalline diamond (N-UNCD) and Pt/Pt interfaces. N-UNCD was selected because similar diamond films have demonstrated low adhesion, chemical inertness, and compatibility with NEMS logic device fabrication. Pt/N-UNCD interfaces subjected to low loads during sliding demonstrated significant increases in contact resistance due to insulating film formation that was not observed at larger loads. Taken in concert, these finding demonstrate the capability of AFM to investigate nanoscale electrical contact phenomena without the need for time-consuming and expensive integration of unproven materials in NEMS logic switches.

TABLE OF CONTENTS

LIST OF TABLES

LIST OF FIGURES

CHAPTER 1: INTRODUCTION

Nanoelectromechanical systems (NEMS) switches have been identified as a potential next-generation transistor [1] with far lower power consumption than existing electronic integrated circuits [2], a critical technological need. These switches are nanoscale moving devices that convert an electrical input signal into motion to close a conductive contact [3]. NEMS switches are therefore a mechanical version of a transistor with topologies that often mimic larger microelectromechanical systems (MEMS) switches. However, NEMS switches require small dimensions for the fast, competitive switching speeds (<100 ns) desired in computer logic applications. The nanoscale dimensions and complex operating conditions at the electrical contact make NEMS logic switches susceptible to tribologically-mediated failure mechanisms that currently render the technology commercially unviable. In particular, the low contact and restoring forces of NEMS switches may lead to device “stiction” (device permanently stuck closed), or intolerable increases in switch contact resistance due to the formation of insulating tribopolymer (TP) films. It may be possible to overcome these problems with the integration of contact materials that demonstrate low adhesion and resist the formation of insulating TPs. To find suitable contact materials, different contact material candidates are usually tested by fabricating a N/MEMS device and testing its reliability - a very time consuming process. There is significant need to find an efficient way to test different M/NEMS contact material candidates without costly device fabrication.

This thesis details the development of an electrical contact testing method using atomic force microscopy (AFM) to evaluate the robustness and adhesion of nanoscale electrical contacts. Pt/Pt contacts, an electrical interface commonly used for micro- and nanoscale switches, were cycled for up to two billion interactions using this method. Cycling was performed in a variety of environments that represent potential operating environments of NEMS logic electrical contact interfaces to demonstrate the versatility of the method and its ability to resolve tribofilm formation, changes to adhesion, and changes to contact resistance. Transmission electron microscopy (TEM) was then used to observe the formation of insulating low density materials, referred to here as TP, at the contact interface.

It is then shown that the application of shear loading of the nanoscale electrical contact removes insulating TP resulting from contact cycling – a potential actuation mechanism that could be integrated into NEMS switch design to improve electrical performance. AFM and chemical spectroscopy were then used to evaluate changes to the conductivity and chemistry of nitrogen-incorporated ultrananocrystalline diamond, a potential next-generation, nanomechanical switch contact material, and compared to that of Pt interfaces under load, shear, and electrical bias.

1.1 The Need for Low Power Computation

Sustained growth in computing power in conjunction with a decrease in computing cost has led to the proliferation of devices utilizing integrated processors in the last half century. These integrated processors are overwhelmingly based on fully-electronic complementary metal-on-oxide semiconductor (CMOS) technology with physics underpinned by a mid-20th century, semiconductor-based technology. While this technology has proven exceptional for decreasing transistor real estate and increasing speed in the last half century [4], it is currently encountering a “power crises.” [1] Further scaling of CMOS leads to intractable increases in power loss per computation due to irreversible processes inherent to the physics controlling device operation [4], [5], [6], [7]. Analysis of production level integrated circuits from Intel between 1989 and 2000 show power requirements per chip increasing drastically from 5 W to 75 W [8].

Recent analysis of worldwide energy consumption has attributed 15% of the overall power grid load to home computers and electronics [8], [9] with 10-17% of that load attributed to just the computer processor [8]. Analysis in the United States has revealed that servers alone account for ~1.2% of the national energy use [10]. The significant power requirements of computer processors, the power crisis of conventional CMOS, trends towards smart devices [8], the increasing penetration of home and laptop computers [8], the desire for longer lasting battery-operated devices [11], and power consumption requirements of CMOS outpacing battery capacities [12] motivates the need to explore lower power transistors. Recognizing the physical limitations of existing CMOS technology, the International Technology Roadmap for Semiconductors (ITRS), a guiding document for the semiconductor industry, has included nanoelectromechanical systems (NEMS) switches as a possible disruptive, low-power technology to cohabitate or usurp the conventional, fully electronic transistor [1].

1.2 NEMS Switches as an Alternative to the Transistor

NEMS ohmic switches utilize mechanical motion to modulate the distance between two conductive contacts referred to as the source (S) and drain (D) electrodes. Figure (A) shows the topology and working principal of a NEMS switch prototype fabricated at the University of Pennsylvania and under continued development and downscaling at Carnegie Mellon University [13], [14]. The device is in an “off-state” when the source and drain electrodes are separated by a physical gap and the “on-state” when the source and drain electrodes are closed with sufficient force to establish an electrical connection. The space separating the switch electrodes in the off-state is often referred to as the switch “gap”. The source electrode of the switch is biased with a voltage potential during operation. In an ideal NEMS switch, closure of the source and drain electrodes results in current flow from the source to drain while contact release results in an infinitely resistive junction. Successful operation of a NEMS switch is dependent on reliably and repetitively making and breaking the source and drain electrodes while maintaining a conductive contact in the device on-state and a high resistance in the off-state.

An input voltage, the gate (G) signal, is converted to mechanical motion to modulate the source-drain electrode separation distance. This motion can be achieved through various means of transduction using many topologies – most notably, ohmic NEMS switches utilizing electrostatic [15], [16], [17] and piezoelectric [14], [18], [19] actuation have been demonstrated that employ topologies such as flexible beams [14], [18], [19] , anchorless bridges [20], nanowires [21] and nanotubes [22], [23], [24], thin films such as graphene [25], and tethered structures [15].

Despite the variation in topologies and transduction mechanisms, all ohmic NEMS switches rely on the closure and separation of a conductive interface in order to achieve switching functionality.

Ohmic NEMS switches provide the same functionality as the conventional metal-oxide-semiconductor field-effect transistor (MOSFET), the fundamental building block of CMOS used in modern integrated circuits. In both technologies, the application of a gate signal results in current transfer from the source to drain. However, CMOS relies on a fully-electronic, semiconductor junction to achieve this functionality whereas NEMS logic switches rely on the mating of conductive contacts (see figure 1.1). The application of a voltage potential to the gate of the MOSFET results in a “field effect” that alters the resistance along a normally insulating layer separating the device source and drain to allow conduction between the two terminals.

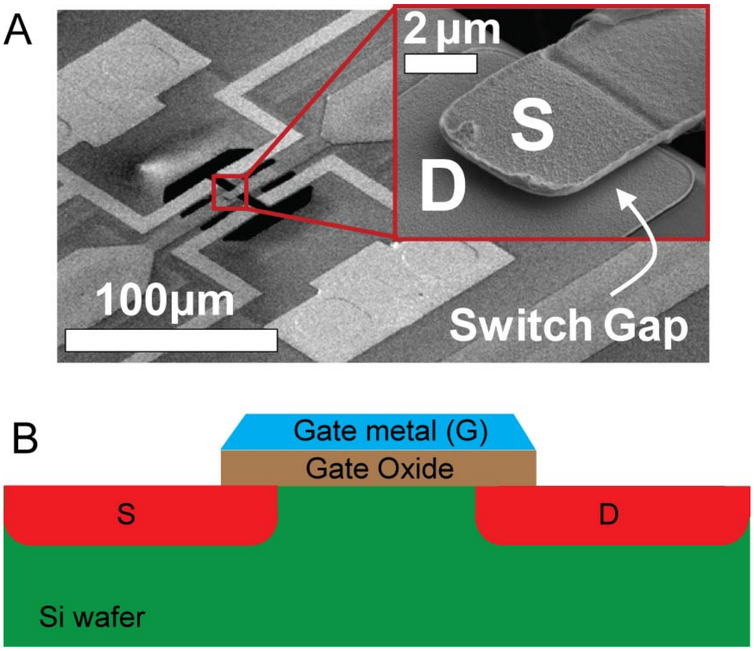

Figure 1.1: (A) Scanning electron microscope image of a prototype piezoelectric ohmic NEMS switch courtesy of Nipun Sinha, University of Pennsylvania. (Inset) Expanded view of the source and drain of the NEMS switch showing the presence of an air gap, (B) Cross-section of an FET (conventional transistor) identifying elements common to both NEMS switches and the FET. The source, drain, and gate structures are labeled, S, D, and G, respectively.

CMOS is currently facing a scaling and power crisis [1]. Digital logic been aggressively scaled in size since its inception in the mid-20th century in order to meet the demands of faster switching times, increased aerial density, and lower operating voltages. This trend, referred to as Moore's Law [26], has seen the density of transistors per chip double every 18 months since the 1960's [27] . However, continued scaling has contributed to increasing amounts of device leakage resulting in significant power loses even when switching is not occurring [28]. Furthermore, a breakdown of Moore's law is predicted by approximately 2020 as critical dimensions of MOSFET exceed physical limitations of scaling [4], [29]. Ohmic NEMS logic switches that reduce power draw per computation have been identified in the ITRS as a potential next-generation technology to cohabitate or usurp FETs [1], [30], [31]. Comparisons between NEMS relay-based logic to conventional CMOS has revealed that energy savings of one to three orders of magnitude may be achieved with NEMS relays due to the low power consumption at the individual switch level [32], [33], [34] and design advantages unique to mechanical relays that reduce the number of switches necessary to perform CMOS-like operations [35].

The reduced power consumption afforded by NEMS logic switches when compared to conventional CMOS is a consequence of the physics underpinning device operation [30]. Figure 1.2 demonstrates these power savings by comparing the source to drain current of NEMS and CMOS switches as a function of gate voltage. Increasing the gate voltage from negative or zero to the threshold turn on voltage (V_{th}) results in current transfer from the source to drain.

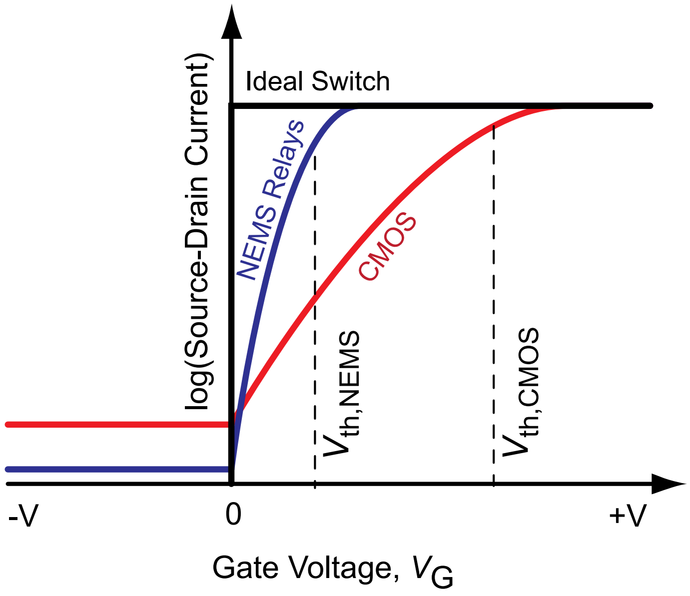

Figure 1.2: Voltage-current (I-V) plot comparing ohmic NEMS switch, CMOS, and ideal switch performance. The gate voltage, V_G, is used to turn the device on resulting in current flow from source to drain. The higher sub-threshold slope of NEMS switch technology allows for the use of lower control voltages that reduce device power consumption per switching event.

The power consumption of a digital switch is characterized by power dissipated during both the device off-state (V_G<0) and on-state (V_G>0). The former is the static power draw of the device and is known as sub-threshold leakage, while the latter is the dynamic switching power termed the sub-threshold swing voltage. NEMS logic switches afford potential power savings in both of these regimes [36], [37].

Sub-threshold leakage in CMOS is dominated by source-drain and gate leakage that scales unfavorably with decreasing device dimensions [30]. This is seen as a current offset for voltages below the turn on threshold voltage, $V_{t,CMOS}$, in figure 1.2. This leakage is due shorter and thinner oxide gate channels necessary to continue Moore’s Law scaling. Sub-threshold leakage in CMOS currently represents ~50% of the total microprocessor power density [30] with standby leakage currents of 1 nA/transistor having been reported at 250 nm gate-width node. This leakage is dominated by gate leakage through the thin gate oxide [6] and continues to increase with device downscaling. NEMS logic relays have already demonstrated leakage values five orders lower than MOSFET at the single device level [38]. These lower leakage values owe to the presence of a physical gap between the source and drain of NEMS relays that eliminates source to drain leakage so long as the gap is > 2 nm [4]. Unique to mechanical relays, physical gaps between gate structures and less leaky gate materials (in the case of piezoelectrically-actuated devices) reduce gate leakage to near zero.

NEMS relays offer far lower dynamic switching power than CMOS. The sub-threshold swing of a logic device describes the inverse slope of the I-V curve and represents the voltage necessary to attain a decade change in current from source to drain [39]. Lower sub-threshold swings correspond to lower turn-on voltages that confer lower active transistor power consumption. The sub-threshold swing of CMOS is fundamentally, thermodynamically limited by its operating mechanisms of electron drift and diffusion to 60 mV/dec [28] with current CMOS demonstrating sub-threshold swings of 70 – 100 mV/dec [30], [39]. This translates to CMOS turn on voltages of 0.3 – 1 V [40], which is several orders of magnitude larger than the minimum voltage (a few mV) necessary for communication. NEMS prototype logic relays offer the lowest sub-threshold slope of potential transistor replacement devices [30] with sub-threshold slopes of 0.03 – 2 mV/dec having already been demonstrated [19], [38], [41], and which translate to a threshold voltage of just a few mV [19].

In addition to their lower power consumption, NEMS logic relays are amenable to application spaces not accessible by CMOS. The functionality of CMOS relies critically on delicate doping levels that require a low thermal budget and minimization of heat generation due to device leakage is of current critical concern. Because NEMS logic does not rely on delicate doping levels, these devices may be amenable to high temperature computing, which would allow for smart sensors in previously inaccessible, harsh environments such as temperatures up to 500 ˚C [2], [42], [43]. Furthermore, co-integration of NEMS relays with CMOS – which is possible due to the low thermal budget of typical NEMS processing [4] – has lead to the exploration of programmable gate array logic based on NEMS relays and traditional MOSFET [44], [45]. The presence of physical gaps in NEMS relays also confers robustness against electromagnetic shocks [2], [42] , which makes these transistors attractive in military applications where radiation-hard attributes are desired. Adhesion between the electrical contacts of NEMS relays may also be used for nonvolatile memory applications where the switch retains its last state (open or stuck closed) [46], [47]. NEMS relays are also amenable to three dimensional integration, which could increase functional density per given real-estate of a microchip to continue Moore's Law scaling [47], [48].

1.3 The Nanoscale Electrical Contact is the Achilles Heel of NEMS Logic Switches

Despite the potential benefits of NEMS logic switches, tribological failure mechanisms at the electrical contact interface currently limit commercial viability of the technology [4]. Transistor functionality is critically dependent on maintaining high isolation in the off-state (switch open) and low resistance in the on-state (switch closed). Failure due to stiction that results in permanent welding of the switch interface, wear of contact materials, adsorbed layers of insulating contaminant films on free surfaces, and insulating tribopolymer (TP)[1] formation of mechanochemical origin have been observed in microscale and nanoscale electrical contacts testing [31], [50].

The effects of stiction, insulating contaminant layers, and TP formation are expected to increase as NEMS relays are scaled down in size. This is a consequence of the dominance of surface forces and the limited closure and separation forces available to NEMS relays. Figure 1.3 compares the closure and separation forces of micro- and nanoscale electrical switches and the necessary separation force for single (the fundamental unit of contact in nanoscale switches) to multiple contacting asperities indicative of multiasperity, microscale contacts. This approximation shows that the surface forces of NEMS relay contacts will outpace the relative generative force of the device. Microscale switches with soft, low hardness metallic electrical contacts (*e.g.* Au) have

---

[1] The term tribopolymer (TP) is used in this document in place of the more commonly used term "friction polymer". Friction polymers were first observed in sliding electrical contacts. However, it has since been observed that such polymer formation can be achieved under normal stresses (absence of significant shear stresses)[49].

been particularly susceptible to stiction due to electromigration or softening that results in contact area growth [51]. Consequently, highly adhesive materials must be avoided to prevent stiction.

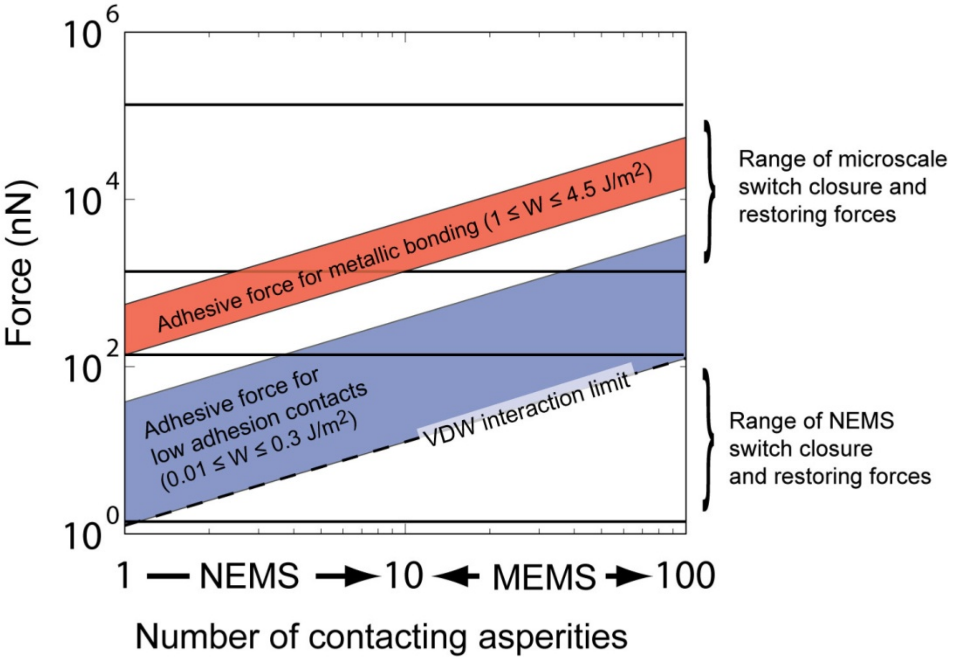

Figure 1.3: Separation force of electrical contacts of various work of adhesion ranges, *W*, as a function of the number of simultaneously interacting surface asperities. The adhesive interaction of the asperity is treated with DMT contact mechanics (eq. 2.8). Microscale MEMS contacts involve several to hundreds of contacting asperities while the ultimate limit of a NEMS contact is the single asperity. The adhesive force of nanoscale electrical contacts exceeds the restoring force of the actuator for small devices. NEMS logic switch contact materials favor low adhesion in order to limit stiction.

Inhibiting the formation of insulating TPs is expected to be the greatest challenge facing nanoscale electrical contacts and is considered to be a function of the surrounding environment, mechanical, electrical, and chemical properties of the electrical contact materials, and the electrical power through the contacts. Figure 1.4 shows the effect of repetitive making and breaking of microscale, multiasperity noble metal contacts under both cold cycling (voltage and current applied only after contact is made) and hot cycling conditions. Even for these typically non-reactive materials, increases in contact resistance after 10^5 to 10^8 cycles can be seen and are attributed to the formation of short-chain carbon and oxygen contaminants [50]. The origin of this effect appears to be mechanochemical in nature – the presence of free surfaces, environmental contaminants, and pressure activate bond formation and chain lengthening. Even hermetically-sealed devices have demonstrated similar behavior [49]. Recent evidence suggests that operation of contacts in reducing environments such as oxygen can significantly reduce TP buildup [52]. However, such device packaging can be costly to implement and limit the operation space of the device. Ultimately, conductive and non-reactive electrical contact materials must be sought.

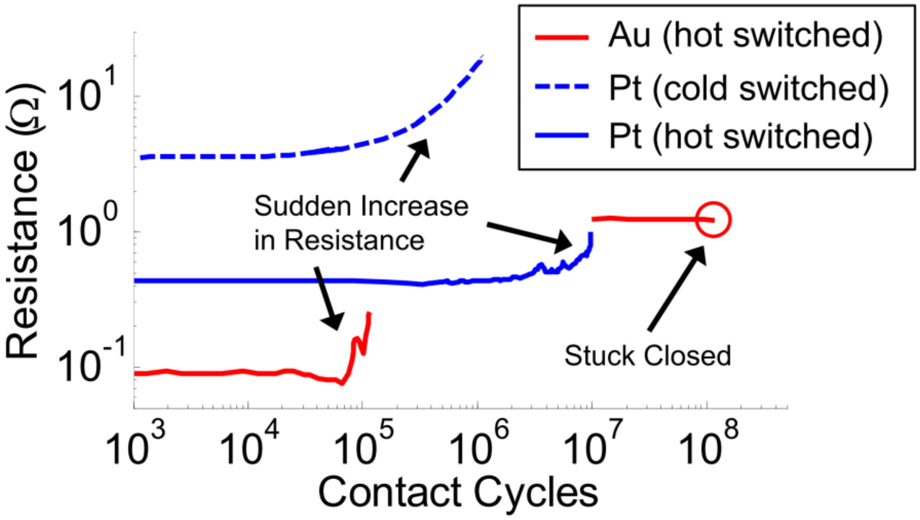

Figure 1.4: Contact resistance as a function of make/break cycles for microscale noble metal electrical contacts of Au and Pt from various sources [50], [51], [53]. The formation of insulating TP results in a dramatic increase in contact resistance after a critical number of cycles. The use of highly adhesive contact materials can also lead to stiction of the switch.

1.4 Scaling Down: The Operational Requirements of NEMS Logic Switches with Comparison to MEMS Switches

The emphasis of this thesis is the study of nanoscale electrical contacts with application to low power NEMS relay logic. However, NEMS relay topologies and most recent work on electrical switch contact behavior borrows from MEMS switches. It is necessary to identify how the local conditions at the electrical switch contact vary between the two technologies – especially in terms of expected failure mechanisms and scaling considerations – when discussing the need for the new contact test method described here.

MEMS relays have been implemented for power savings and superior functionality in radio frequency systems [54], are now considered a mature technology [4], and several have been commercially deployed. Many of the lessons learned for the contact behavior of conventional switch materials (*i.e.* metals), like that shown in figure 1.4, can be attributed to work focused on microscale, multiasperity MEMS contacts. The fundamental unit of contact, the single asperity, which is the ultimate limit of NEMS contact can also be viewed as a single element of a multiasperity contact (see figure 1.5). **Error! Reference source not found.** lists the salient differences between the contact environment and lifetime needs of NEMS and MEMS relays.

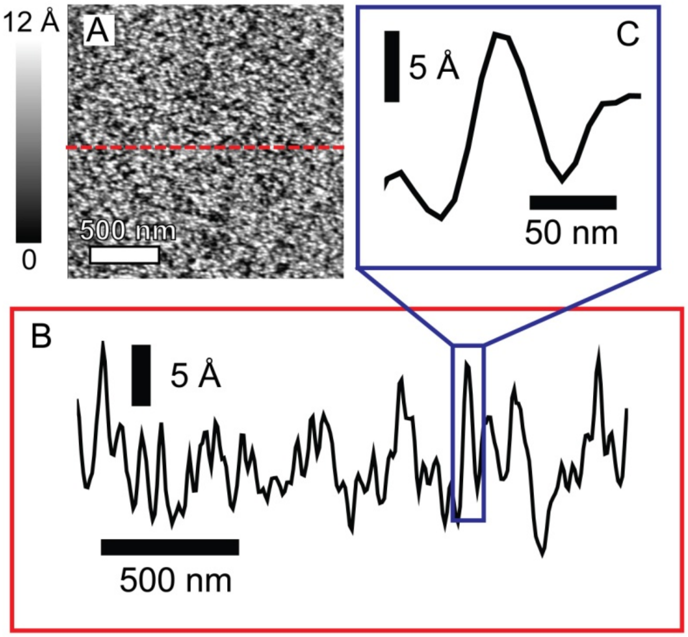

Figure 1.5: Surfaces, even those that are highly polished and smooth to the eye demonstrate nanoscale roughness. (A) A 2 x 2 μm^2 atomic force microscopy scan of a smooth Pt surface with a mirror-like finish. (B) A two-dimensional cross section from (A) shows significant nanoscale roughness. (C) A single asperity from the two-dimensional cross-section from (B). The work in

this thesis focuses on single asperity surface interactions that represent the fundamental unit of contact of a rough surface or the ultimate limit of contact size for NEMS logic switches.

Table 1.1: Comparison of the operational requirements of MEMS RF switches vs. NEMS logic switches.

	MEMS RF Switches	**NEMS Logic Switches**
Required lifetime (cycles)	10^{8} – 10^{11} [54], [55]	10^{15} - 10^{16} [4]
Contact area of conductive contacts (m^2)	10^{-8} - 10^{-12}	10^{-17} - 10^{-18}
Adhesion	Not explicitly treated	Primary concern (impacts energy consumption and reliability) [4]
Device contact/restoring force	μN – mN [54]	5 – 150 nN
Voltage across the contact	2 – 70 V	Several mV to V
Current through the device conact	50 – 150 mA [54]	nA - μA
Current density at the contact (A/m^2)	10^{9} – 10^{14}	10^{5} - 10^{11}
Power (mW)	<500 [54]	<1
Maximum contact resistance (Ω)	0.5 – 2 [54]	$<10^{6}$
Dominant contact materials selection characteristics	High conductivity and non-fouling	Moderate conductivity, non-fouling, and low adhesion

The lifetime requirements for NEMS logic switches differs substantially from RF MEMS switches. Ohmic RF MEMS switches are designed as interrupts for radio frequency transmission lines. While the contacts of these devices carry RF signals up to GHz frequencies, making and breaking of the contact happens far less frequently, usually on the order of kHz or less, requiring 10^{8}-10^{11} cycles before failure in commercially viable applications [54], [55]. NEMS logic relays carry a DC signal and their interruption of that signal determines the clock frequency of the device

– thus, NEMS relays that are competitive with CMOS must exhibit nanosecond closure times, which requires upwards of 10^{16} operating cycles without failure [4].

The electrical constraints and power handling requirements of the electrical contacts of NEMS switches also differ substantially those of ohmic RF MEMS. Commercially viable ohmic RF MEMS switches demand contact resistances from 0.5 - 2 Ω [54, p. 5] in order to minimize insertion loses, which limits possible set of contact materials to high conductivity metals. Permissible NEMS logic relay contact resistances have a broader range – from several kΩ up to 100 kΩ, depending on device topology and the electrical time constants of the implementation – such that alternative, novel, and previously unconsidered materials (*e.g*. conductive oxides [56] and conductive diamond-like materials [24]) could be implemented at the contact. Furthermore, the power across ohmic RF MEMS contacts often reaches 100+ mW with power being transferred across the contact after closure (cold switching). NEMS logic relays are expected to experience, at most, a few mW of power across the contact and operate in a hot-switched mode (bias applied across the contact during closure) with <1 V across the contacts during switching. These differing switch contact environments ultimately affect the local conditions at the contacting asperities that could change the degradation mechanisms of the contact. For instance, the high voltages (10 V and higher) across the contacts of MEMS devices can lead to field evaporation [57] that may not be a significant degradation mechanism in nanoscale NEMS switch contacts.

1.5 Existing Methods to Test Electrical Contact Reliability at the Microscale and the Need for a New Nanoscale Electrical Contact Test Method

Testing of electrical contacts for micro- and nanoscale electrical switches has been typically achieved via two routes. New contact materials may be integrated directly into switch designs or electrical contact materials are isolated and tested using mechanical testing apparatuses that mimic the making and breaking of a switch. The former is generally time-consuming and costly, requiring several months to years of fabrication. Often, unique, but potentially superior, contact materials are avoided in lieu of materials that have proven ease of fabrication. The use of mechanical test apparatuses are preferred for isolating the contact material. However, as will be discussed in the following, previous microscale electrical contacts suffers present several shortcomings that the work in this thesis addresses.

Evaluation of electrical contact materials at the microscale and outside of the device has been achieved using modified scanning probe microscopy setups and nanoindentation. However, these methods are time consuming and do not yield the number of interaction cycles expected for NEMS switch electrical contact materials. Chen *et al*. [58] utilized a custom fabricated cantilever that was brought into contact with various counter surfaces to investigate contact resistance changes to noble metal contacts of ~5 μm radius for up to 10^7 contact cycles. While they were able to show significant increases in contact resistance (due to TP formation) for contacts of Ir, Ru, and Au, the method the employ is limited to 800 cycles/sec., which means that only ~70 million contact cycles would take 1 day of testing. Similarly, Yang *et al*.[57] investigated Au/Au microcontacts using a flexible cantilever terminating in microscale, multasperity contact in contact with a flat counter surface to reveal significant material transfer under hot switching conditions. This test was performed with 1 ms switching times, which translates to ~86 million cycles in a 24 hour period. Nanoindentation methods are even more limited in cycling throughput. Dickrell and Dugger [59] utilized a modified nanoindenter of radius 1.6 mm in contact with a flat counter surface to investigate Au/Pt contacts for up to 100 cycles. Measurements in their work spanned several seconds per contact event significantly limiting the total number of cycles that could be achieved.

While existing work on electrical contacts has revealed the role of contact materials and switching environment on the longevitity of electrical contacts, it suffers from several issues that limit applicability to nanoscale electrical contacts. Throughput is low, allowing only hundreds to hundreds of millions of cycles per day of testing. Contacts are multiasperity with surfaces consisting of many contacts points. The true contact area, forces, and stresses experienced by the contact are obscured by the roughness of the surface. Finally, the adhesiveness of the interface, which is a critical parameter for NEMS switches, is often not acquired or reported.

To date, methods to evaluate electrical contact degradation have focused on microscale, multiasperity contacts. These tests have been largely geared towards MEMS devices that have large generative and separation forces and require on the order of 10^8 contact cycles to demonstrate contact material viability. Relatively little is known about the evolution and failure mechanisms of nanoscale contact. This thesis describes a testing methodology for single asperity contacts based on atomic force microscopy (AFM) that permits the investigation of several billion contact events in laboratory timeframes. Testing based on this method could allow for the rapid investigation of new and unproven contact materials before costly and time consuming integration into switches.

CHAPTER 2: EXPERIMENTAL METHODS

This chapter details instrumentation and methods used for the interrogation of changes to the contact resistance, adhesion, and chemistry of nanoscale electrical contacts subjected to switch-like cycling and load, shear, and electrical power. First, atomic force microscopy (AFM), an instrument that enables high-fidelity measurements of interaction forces, adhesion, and conductivity between nanoscale contacts, is described. Second, electron microscopy used to observe the shape of the nanoscale electrical contact is described. Third, methods used to investigate the chemical nature of electrical contact films and the method of depositing these films are described. Fourth, a protocol developed to simulate several billion NEMS switch-like interactions of nanoscale electrical contacts that leverages the capabilities of AFM is detailed. Finally, a protocol to evaluate changes to the conductivity and surface chemistry of electrical contacts exposed to shear contact, load, and electrical bias is described.

2.1 Atomic Force Microscopy with Application to Nanoscale Electrical Contacts

Atomic force microscopy (AFM) was used extensively in this thesis to interact with electrical contacts of nanoscale dimensions under nN loads. AFM enables high fidelity characterization of adhesion, conductivity, and surface geometry of these contacts. This section motivates the use of AFM for the study of single asperity and NEMs logic-scale electrical contacts. Two modes of AFM employed in these studies - static mode and dynamic mode AFM (dAFM) - are defined. Methods to characterize the loading force during both interaction modes are then presented.

2.1.1 Atomic Force Microscopy as Enabling Instrumentation for Electrical Contact Characterization

Atomic force microscopy has been a highly successful technique for imaging, manipulating, and interrogating the fundamental physics of nanoscale surfaces since its advent in 1986 [60]. The basic principle of AFM relies on the interaction of a tip of nanoscale dimensions with a counter surface. Unlike scanning tunneling microscopy, which requires the use of conductive tips and substrates, AFM is amenable to insulating materials. This is particularly useful when interacting with surfaces of varying conductivity like those investigated here.

AFM utilizes mechanical amplification of surface forces to interrogate nanoscale tip-surface forces with sub-nN precision. Figure 2.1 shows a schematic of a representative conductive atomic force microscopy (C-AFM) setup used to interrogate electrical phenomena. This deviates from standard AFM in that a voltage source, current amplifier, and a series resistor is included for electrical characterization of nanoscale electrical interfaces. There are four main elements to an AFM that confer its high force resolution: 1) a flexible cantilever terminating in a sharp tip, often with a hemispherical or rounded profile of nanoscale (<100 nm) radius, 2) a piezoelectric scanner, 3) a photoluminescent diode or laser, and 4) a quadrant photodetector.

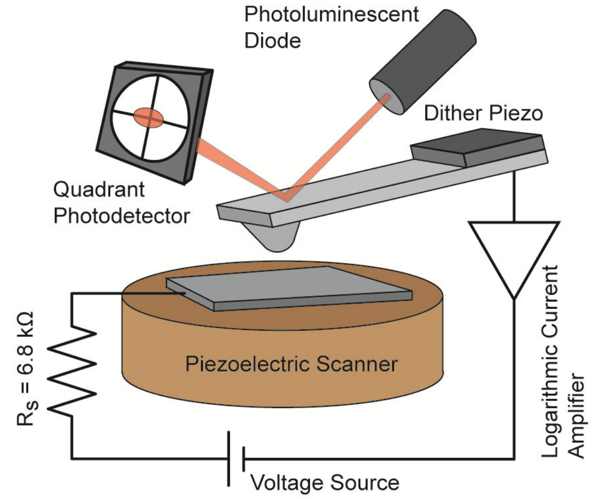

Figure 2.1: A general schematic of the working components of a typical conductive AFM setup. The components that confer the core functionality of an AFM are labeled here. This diagram includes a DC voltage source, current amplifier, and series resistor utilized for conductive AFM.

The flexible cantilever is the central force sensing element of the AFM. A canonical AFM cantilever consists of a larger chip body used for ease of handling, a flexible cantilever of engineered stiffness attached to the chip body, and a pyramidal tip fabricated at the end of the cantilever that terminates in an apex of nanoscale dimensions. Most commercially produced AFM probes and those employed in this work are fabricated out of Si using conventional microfabrication techniques and have tip radii from several to tens of nm.

Interaction between the cantilever tip and a substrate is achieved using piezoelectric scanner, amplification of the cantilever angle, and a sophisticated feedback loop. The piezoelectric scanner provides the relative tip-surface motion and, in most systems, allows for movement of nanoscale precision in three axes. This functionality enables a diverse array of tip surface interactions - including pulsing into and out of a surface at a specific location (known as a force versus distance measurement, FvD) or lateral scanning to reveal the frictional interaction of the tip and surface, surface topography, and, in the case of C-AFM, conductivity of the interface.

Interaction of the cantilever tip with a counter sample causes bending of the cantilever. A luminescent diode or laser impinging on the back of the cantilever is directed into a photodetector. Through specific design of the optical dimensions of the system, changes to the cantilever bend angle result in displacement of the laser path at the plane of the photodetector. Photodetectors of most modern AFM systems allow permit detection of in-plane cantilever bending due to normal loading of the cantilever and lateral (torsion) of the cantilever resulting from frictional interaction at the tip surface-interface. The piezoelectric scanner and photodetector are coupled by a controller (not shown in figure 2.1) that provides feedback on the position of the probe. The user specifies a load or feedback parameter that the AFM should track. The controller then varies control voltages sent to the piezoelectric scanner to modulate the tip-surface interaction based on variations in topographical features.

C-AFM was used in this thesis to interrogate the robustness of nanoscale electrical contacts. A DC voltage source establishes an electric potential between the tip and surface. This voltage may also be referred to as the “bias”. The geometry of the nanoscale probe tip and protuberances (roughness) on the sample surface lead to a constriction resistance, R_{const}, and ultimately limits the current through clean, conducting surfaces. Insulating films due to adsorbed contamination on the sample surface or the growth of nonconductive layers may also lead to an additional series resistance, R_{film}, that can be greater in value than the constriction resistance. The sum of constriction and insulating resistances define the total contact resistance, R_c, of the interface. The current through the contact is recorded using a current-voltage amplifier. A series resistor, R_s, was employed in the work here to prevent large current flow that could melt or vaporize the contact under the application of unintended, large voltages or short the amplifier in the event of unintended interaction of bias leads. R_s is subtracted from all measurements when quoting contact resistance.

2.1.2 Descriptions of AFMs Used in This Thesis

Two AFMs were employed in the studies presented in this thesis. An Asylum MFP-3D with an ARC2 controller (Asylum, an Oxford Instrument Company, Santa Barbara, CA, United States) was used for single asperity cycling of Pt/Pt contacts presented in section 2.6 and for lateral scanning of conductive diamond in section 2.7.1. A Veeco Dimension 3100 (formerly Veeco, now Bruker, Santa Barbara, CA, United States) was used to laterally scan conductive diamond for chemical interrogation described in section 2.7.2. Both AFMs feature a clamshell design, a metalized chamber wall to improve electrical isolation, and access for gas flow purging of the internal environment. Electrical measurements on the MFP-3D were achieved with a custom-built logarithmic current amplifier (described in section 2.2) while those on the Dimension 3100 were taken using an add-on extended TUNA module supplied by Veeco. Controlled environment studies in both systems were achieved by purging the system with N_2 blowoff from 80 L nitrogen dewars from Airgas (Airgas East, Malvern, PA, United States).

2.1.3 Static and Dynamic AFM

Two modes of AFM are used in the data obtained here – static mode AFM and dynamic mode AFM (dAFM). Static mode AFM was used to interact with surfaces over slow time periods (typically seconds to minutes) while making direct contact between the tip and sample. Scanning of a surface (tracking topography), interrogation of tip-surface conductivity, frictional forces between the tip and surface, and the adhesive tip-surface interaction may all be probed using this mode. dAFM is used to cycle electrical contacts with tip surface interactions occurring at kHz frequencies with intimate tip-surface contact occurring over nanosecond windows.

FvD measurements underpin much of the data presented in this thesis and are, therefore, explained in detail. FvD measurements obtained using static mode AFM reveal the adhesion of the tip-surface interface and, in the case of C-AFM, the conductivity of the tip-surface interface as a function of load. Figure 2.2 shows a canonical FvD measurement obtained with a Pt-coated AFM cantilever on a Pt substrate. The FvD measurement begins with the probe free of the counter surface. The relative separation between the probe tip and sample surface is the reduced until contact occurs. Tip-sample forces and the compliance of the cantilever lead to an instability, referred to as snap-in. This condition occurs when the derivative of the tip-surface forces with respect to vertical position exceeds the stiffness of the cantilever and results in a jump to contact condition. The cantilever is then loaded to a user specified force or displacement. After achieving the user specified displacement or load, the cantilever is retracted from the surface back to its original out-of-contact position. During retraction, adhesion between the tip-surface results in a second instability referred to as pulloff. Knowledge of the tip shape and force of adhesion during pulloff may be used to extract the work of adhesion between the two surfaces.

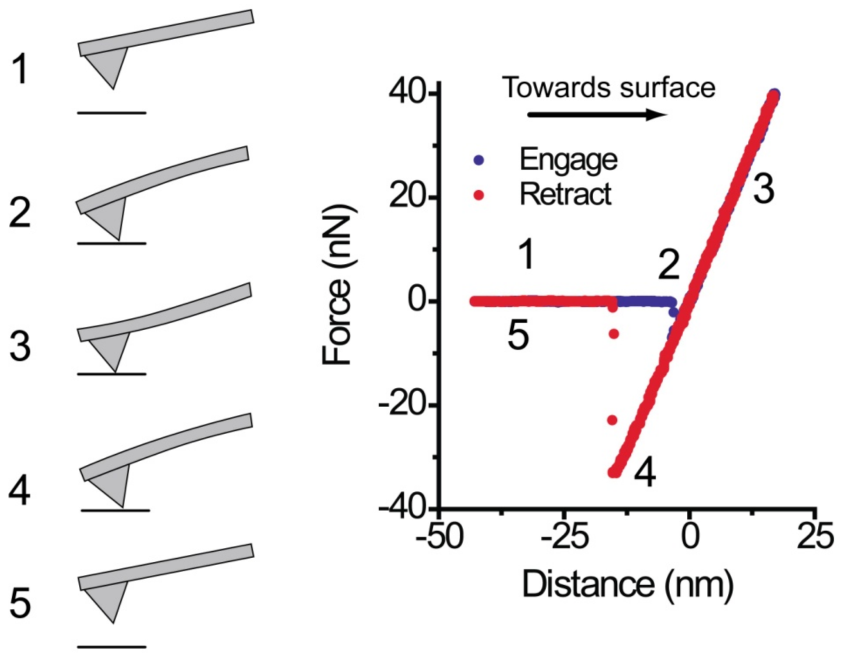

Figure 2.2: A force versus distance (FvD) measurement obtained with a Pt-coated AFM probe on a Pt surface. (Left) A vignette showing a magnified representation of cantilever-sample interaction during an FvD measurement and (right) the FvD data. Relevant interactions are labeled 1 – 5. (1) The probe starts in a retracted state from the surface and the relative tip-sample distance is decreased until snap-in occurs (2). External loads are applied (3) up to a load or distance specified by the user. The probe is then retracted from the surface. Hysteresis during unloading is due to adhesive interactions between the tip and sample. Pull off (4) occurs when the bending force of the cantilever exceeds to interaction force of the tip and sample. (5) Retraction is continued until the tip is free from the surface.

Amplitude modulated AFM (AM-AFM) is a form of dAFM used in this thesis to both image surfaces and cycle electrical contacts. AM-AFM utilizes a dither piezo element located near the base of the probe chip to acoustically excite resonances in the AFM probe. Typical probe resonances range from 2 kHz for soft cantilevers to 350 kHz for stiff cantilevers. AM-AFM measurements begin by tuning the cantilever at or near its resonance frequency while the tip is retracted from the surface (free of tip-surface forces) to a free air amplitude, A_0. The resulting deflection profile of the probe is sinusoidal. The probe is then advanced towards the surface where tip-surface forces act as an additional load on the cantilever tip resulting in a damped amplitude, A_d. Feedback in open air AFM systems utilize a lock-in to keep driving the cantilever at its resonance frequency and adjust the tip-surface separation to maintain A_d. The user specifies both A_0 and A_d, with the ratio of the amplitudes, the type of cantilever, and the nature of the tip surface interaction determining the maximum load between the tip and surface. Section 2.1.5 discusses the details of determining tip-surface forces during AM-AFM.

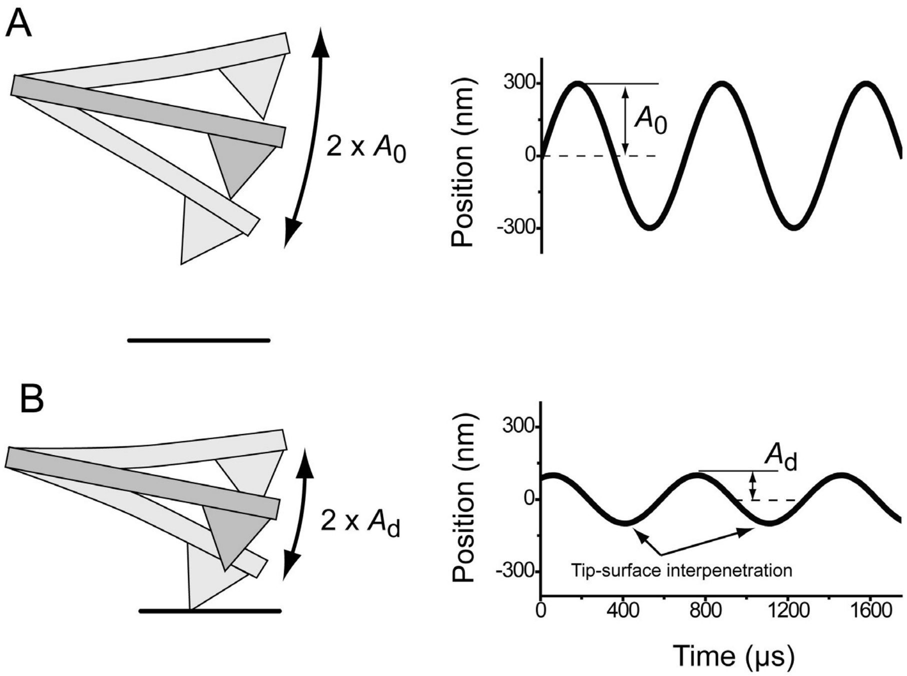

Figure 2.3: The working principle of AM-AFM. (A) A probe is excited in the vertical plane at or near its resonant frequency to an amplitude of A_0 at a distance far enough from the sample surface to ensure negligible tip-surface interaction forces. (B) The relative tip-sample separation is then decreased until tip-surface forces cause a reduction in the probe amplitude, resulting in damped amplitude A_d. Both the driving signal and the cantilever deflection profile are sinusoidal. Proper selection of A_0 and A_d ensures that interpenetrating tip-surface interaction will occur at the trough of the cantilever response.

2.1.4 Calibrating AFM Stiffness for Static AFM

In order to quantitatively quote force values during tip-surface interaction, accurate calibration of the AFM cantilever stiffness and displacement is essential. The stiffness of typical AFM cantilevers is linear for small displacements used in typical interaction regimes. Thus, to high accuracy, the tip-sample force is treated as a linear spring and is a product of the cantilever stiffness and deflection. Bending of the cantilever results in deflection of the laser signal in the plane of the photodiode, which is reported to the AFM system in units of volts, V_{pd}. Calibration of two values of interest – deflection sensitivity, S, and cantilever spring stiffness, K_{cant} - must be determined to accurately quote tip-surface interaction force, $F_{\mathrm{t-s}}$. The tip-surface interaction force can be represented as

$$F_{t-s} = K_{cant}\delta_{cant} = K_{cant}\left(V_{pd}S\right) \qquad \text{Eq. 2.1}$$

where δ_{cant} is the cantilever deflection.

The normal stiffness of an AFM cantilever can be determined by many methods, such as interrogating the thermal fluctuations of the probe, observing is driven damped amplitude in a fluid (liquid, air, etc), changes to resonance with the addition of mass, calculation using geometry and material properties, or by using a traceable reference cantilever. Each method offers a varying degree of uncertainty and complexity [61]. The two most popular methods, due to their ease of use, implementation in many commercial AFM systems, and the accuracy are thermal [62] and Sader [63] calibration. These two calibration methods were used in this thesis.

Thermal calibration takes advantage of Brownian noise inherent in mechanical structures of a finite temperature. Cantilever stiffness is related to thermal vibrations of the cantilever using equipartition theorem and is described as [62]

$$K_{cant} = \alpha\frac{k_B T}{\left\langle \delta^2 \right\rangle} \qquad \text{Eq. 2.2}$$

where k_B is the Boltzmann's constant, T is temperature, $\left\langle \delta^2 \right\rangle$ is the mean square cantilever displacement, and the prefactor, α, accounts for nonidealities and the mode shape of the cantilever. In accordance with the findings of Walters *et al*. [64][2], α is taken to be 0.917 here. In practice, the amplitude of the cantilever thermal response, A, is fit using a simple harmonic oscillator model (Lorenztian) of the form [66]

$$A^2 = \frac{\left(\frac{A_{dc}}{\omega_r}\right)^2}{\left(\frac{1}{\omega_r} - \omega_r\right)^2 + \frac{1}{Q^2}} + A_{wn}^2 \qquad \text{Eq. 2.3}$$

where $\omega_r = \frac{\omega}{\omega_0}$, ω is frequency, ω_0 is the fundamental resonant frequency of the probe, A_{dc} is the amplitude scaling factor, Q is the cantilever thermal quality factor, and A_{wn} is a factor that accounts for white noise in the thermal data. This method [64] deviates from earlier approaches in that the amplitude of the function is fit instead of integrating the cantilever response curve and results in reduced low-frequency noise and the occlusion of higher oscillation modes. The fit function may then be related back to the mean square displacement for extraction to the cantilever stiffness using the expression from [64]

$$\left\langle \delta^2 \right\rangle = \frac{\pi}{2} f_0 Q A_{dc}^2 \qquad \text{Eq. 2.4}$$

Sader calibration utilizes the hydrodynamic response of a cantilever to determine the normal cantilever stiffness. Using this method, the cantilever is driven using a fixed dither piezo amplitude and the driving frequency swept around the resonant frequency of the cantilever. The resulting photodiode amplitude response is tracked using a lock-in amplifier – now standard on

---

[2] Walters *et al*. provide a well-motivated justification for the correction factor 0.917 based on the work of Butt and Jaschke [65].

most commercial AFM systems. Calculation of the stiffness only requires knowledge of the planeview dimensions of the cantilever and the density and kinematic viscosity of the surrounding fluid. This relationship is shown by Sader *et al*. [63] to be

$$K_{cant} = 7.5246 \rho_f w^2 L Q f_0 \Gamma_i \left(\frac{2\pi \rho_f f_0 w^2}{4\eta_f} \right) \qquad \text{Eq. 2.5}$$

where ρ_f is the density of the surrounding fluid medium, *w* is the cantilever width, *L* is the cantilever length, η_f is the kinematic viscosity of the surrounding fluid, and *Γ* is a hydrodynamic function that depends on the Reynold’s number (quantity in brackets) of the cantilever.

In practical use, the amplitude of the driven cantilever response is fit to the same simple damped-driven harmonic model shown in eq. 3.5 to extract the quality factor. Q may also be estimated more simply by dividing the width of the resonance peak at $\frac{1}{\sqrt{2}}$ factor of the peak amplitude by the cantilever resonance frequency. The former is more accurate, has been integrated into the software of several commercial AFMs, and is used here.

Thermal calibration is typically favored with probes of low stiffness (<1 nN/nm) while Sader calibration is favored for probes of high stiffness (> 5 nN/nm). The probes used in the studies reported here have a stiffness <3 nN/nm. Therefore, the final stiffness used during testing was most often taken as the thermally-calibrated stiffness when thermal data capture was possible. A combination of Sader and thermal calibration was also used to determine both the approximate deflection sensitivity and stiffness of the cantilever without touching the surface and is explained in the following section.

The deflection sensitivity of the cantilever is the second piece of information necessary to perform calibrated force interaction using AFM. This quantity relates voltage output from the photodiode to physical units cantilever deflection. Typically, and in this work, the most accurate deflection sensitivity used to extract force from cantilever interaction is determined from the loading portion of an FvD measurement (part 3 of figure 2.2). This assumes a well-calibrated piezoelectric scanner such that an accurate relationship between piezoelectric scanner displacement and cantilever deflection can be correlated. In order to ensure this, the calibration of the piezoelectric scanner in the AFM measurements here was periodically checked with height reference standards.

Typically, a user would perform a Sader calibration to determine K_{cant} and then perform an FvD measurement to determine S. However, if S is underestimated during first contact with the surface (when engaging the probe tip with the surface), large forces may be unknowingly applied to the probe tip. Because of the delicacy of nanoscale electrical contacts, initial loading of the cantilever (determination of both K_{cant} and S) was approximated without touching the surface. To do so, Sader calibration was first performed to determine K_{cant} and was followed by thermal tuning with a known K_{cant} to solve for S. S is then refined by performing an FvD measurement and fitting the engage slope of an FvD measurement and, in some cases, K_{cant} refined by performing a final thermal tune with well-described S.

2.1.5 Quantifying Peak Interaction Force and Stress during Dynamic AFM

dAFM was employed to cycle contacts in order to mimic nanoscale electrical interface contact of a NEMS switch. Consequently, maximum tip-surface interaction forces mirroring those expected for NEMS logic switches (several to hundreds of nN) need be prescribed. While the loading force in static AFM only requires knowledge of the deflection sensitivity and stiffness of the probe, tip-surface interaction during dAFM requires modeling of the cantilever dynamics. Selection of user prescribed variables such the free air amplitude (A_0), the damped amplitude (A_d), and the stiffness of the cantilever couples with the mechanical and electrical properties of the tip-surface interaction to yield a maximum force at the trough of each dAFM cycling period. In the work here, a voltage is applied between tip and substrate to mimic hot switching (voltage applied between counter surfaces during closure and separation) as it might be encountered in a

NEMS logic switch. Tip-surface interaction in the case of an applied bias and resulting in interpenetration of the interface has not been treated in literature. This section describes the extension of an existing tip-surface interaction model for dAFM that includes additional force terms resulting from a voltage applied between the cantilever, tip, and surface.

Models of tip-surface interaction forces for dAFM have developed in the past few decades. The most popular and widely used models represent the AFM probe tip-surface interaction as a single degree of freedom damped harmonic oscillator [67] as shown in figure 2.4.

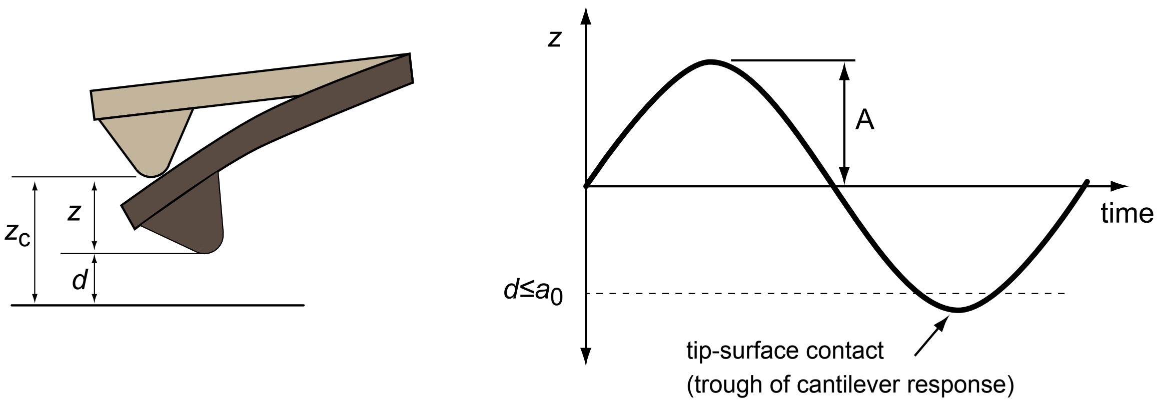

Figure 2.4: (A) The tip-surface interaction during dAFM is described using a single degree of freedom harmonic oscillator model. (B) Tip-surface interaction under the appropriate selection of cantilever stiffness, A_0, and A_d results in interpenetrating interaction at the trough of the cantilever response that mimics asperity interaction in a nanoscale electrical switch contact.

Harmonic models of dAFM tip-surface interaction have found success in describing bi-stabilities encountered during imaging [68], the minimization of interaction forces during biological imaging [69], and, more recently, in the analysis of wear of AFM probe tips [70]. Closed form equations to quantitatively predict interaction forces [71] and an online dAFM tip-surface force calculator [72] have also been developed. However, tip-surface forces have only been investigated under the action of van der Waals (vdw) interactions, single asperity contact mechanics interactions when the tip and sample touch, and electrostatic forces in the absence of tip-surface interpenetration [73]. However, dAFM used to cycle contacts in this work involves interpenetration of the contact with an applied bias in order to mimic hot switching in a NEMS logic contact – a situation that has not been addressed in previous dAFM tip-surface force models. The analysis presented here is motivated by the calculations that show that electrostatic forces due to an imposed tip-surface voltage can exceed vdw force contributions for large tip-surface biases (see figure 2.5). This is supported by experimentally by the observation of significant contributions from the electrostatic load imposed by a cantilever-surface and tip-surface potentials in both static AFM [74], [75] and non-contact dAFM [73]. Therefore, an additional loading term due to a tip-surface and cantilever-surface voltage, like that used in [76], has been integrated into the dynamic model of dAFM interaction [68] and extended to the case where interpenetrating contact occurs. The development of this model is now described in detail.

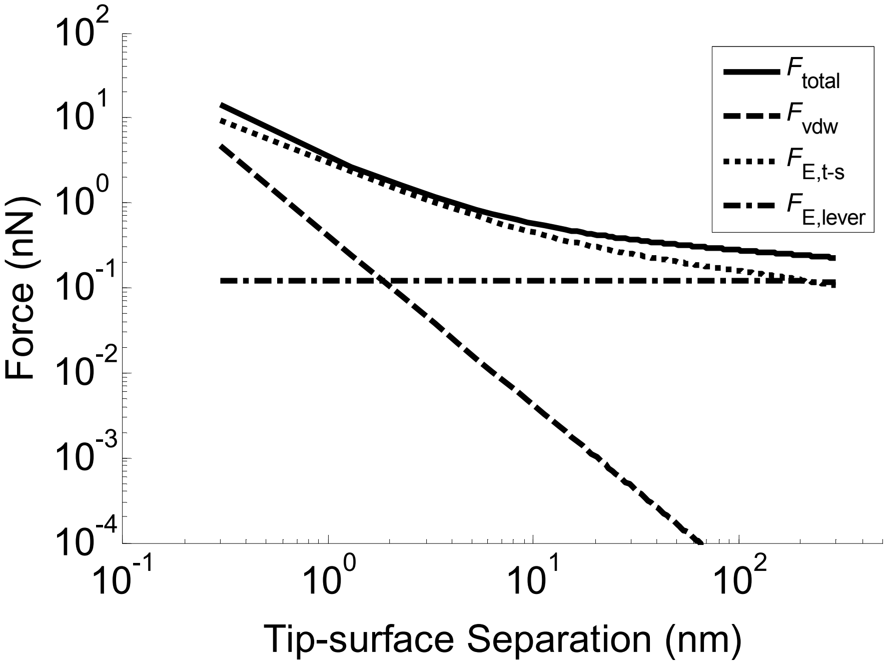

Figure 2.5: Contribution to tip-surface and cantilever-surface loading force in the presence of a voltage applied between the tip and surface. The total interaction force, F_{total}, interaction force due to vdw components, F_{vdw}, electrostatic tip-surface force, $F_{\text{E,t-s}}$, and electrostatic cantilever-surface force, $F_{\text{E,lever}}$, are included. The plot uses parameters reasonable for testing performed in this thesis with R = 25 nm, θ = 19˚, α = 11˚, L = 225 μm, w = 30 μm, h_t = 14.8 μm, H = 1x10-19 J, and

a tip-surface voltage of 2 V. The plot shows that voltage applied between the tip and surface leads an additional and non-negligible electrostatic tip-surface interaction force.

The harmonic model shown in figure 2.4 assumes an AFM tip of radius *R* that interacts with a surface at an instantaneous separation of *d*. A time varying force, F_0, applied to the base of the cantilever by a dither piezo results in cantilever oscillations with an instantaneous positional difference from the static equilibrium position of *z*. The height of the cantilever equilibrium position above the sample surface is z_c. Interactions between the tip and sample are included using a generalized tip-sample force, F_{t-s}, that varies with tip-surface separation. The dynamic equation of a single degree of freedom damped harmonic oscillator as developed in by Garcia and San Paulo [68] is

$$m_e \frac{dz^2}{d^2t} = -k_c z - \frac{m_e \omega_0}{Q}\frac{dz}{dt} + F_{t-s} + F_0 \cos\left(\omega t\right) \qquad \text{Eq. 2.6}$$

where m_e is the effective mass of the cantilever [77, p. 416], which includes mass contributions from the AFM tip, ω is the driving frequency, and *t* is time. The effective mass is related to parameters measureable using AFM through the following

$$m_e = \frac{K_{cant}}{\omega_0^2} \qquad \text{Eq. 2.7}$$

where ω_0 is the resonant frequency of the cantilever.

The tip-sample force is most commonly expressed as a combination of vdw interaction between a hemisphere of radius *R* and a flat surface when out of contact ($d>a_0$) and vdw plus single-asperity interactions during contact ($d \leq a_0$). Here, a_0 is the equilibrium separation between the tip and surface at incipient contact (in the absence of external load). While several variations of single asperity contact mechanics during tip-surface interaction have been investigated

(Hertzian contacts that exclude adhesion, JKR [78], and DMT [71]), DMT contact mechanics are exclusively considered in this work due to the use of relatively hard contact materials and small asperity radii[3]. Figure 2.6 shows all relevant tip-surface and cantilever-surface force interactions referenced in the development of the tip-surface force interaction model presented here. The tip-surface interaction as a function of tip-surface separation is shown compactly as

$$F_{t-s} = \begin{cases} -F_{vdw}\left(z_c + z\right) & d > a_0 \\ -F_{vdw}\left(a_0\right) + F_{DMT,rep}\left(a_0 - z - z_c\right)^{3/2} & d \le a_0 \end{cases} \qquad \text{Eq. 2.8}$$

where F_{vdw} is the vdw force between the tip and substrate and $F_{\text{DMT,rep}}$ is the repulsive DMT contact force during tip-surface interpenetration, which can be written as

$$F_{DMT,rep}\left(z^*\right) = \frac{4}{3} E^* R^{1/2} \left(z^*\right)^2 \qquad \text{Eq. 2.9}$$

where z^* is a generalized tip-surface separation parameter and E^* is the combined modulus of the tip, t, and surface, s, that depends on Young's modulus, E, and Poisson's ratio, v, through

$$E^* = \left(\frac{1-\nu_t^2}{E_t} + \frac{1-\nu_s^2}{E_s} \right)^{-1} \qquad \text{Eq. 2.10}$$

The strength of vdw tip-surface interactions in eq. 2.8 assumes sphere on flat interaction [80] and can be represented compactly as

---

[3] The Tabor parameter, μ_T, defines the appropriate contact treatment of a single asperity contact. For $\mu_T < 0.09$, DMT contact mechanics dominate while for $\mu_T > 5$, JKR contact mechanics dominate. For all contacts investigated in this thesis $\mu_T < 0.2$, which places contact in a transition regime [79] that is either close to or well within the DMT regime.

$$F_{vdw}\left(z^*\right) = \frac{HR}{6\left(z^*\right)^2} \qquad \text{Eq. 2.11}$$

where *H* is the Hamaker constant, which contains information on the adhesiveness of the contact. *H* can be determined from AFM measurements by relating the description of the adhesive force of a DMT contact to the vdw force at the instance of tip-surface separation through

$$F_{adh} = 2\pi RW = \frac{HR}{6a_0^2} \qquad \text{Eq. 2.12}$$

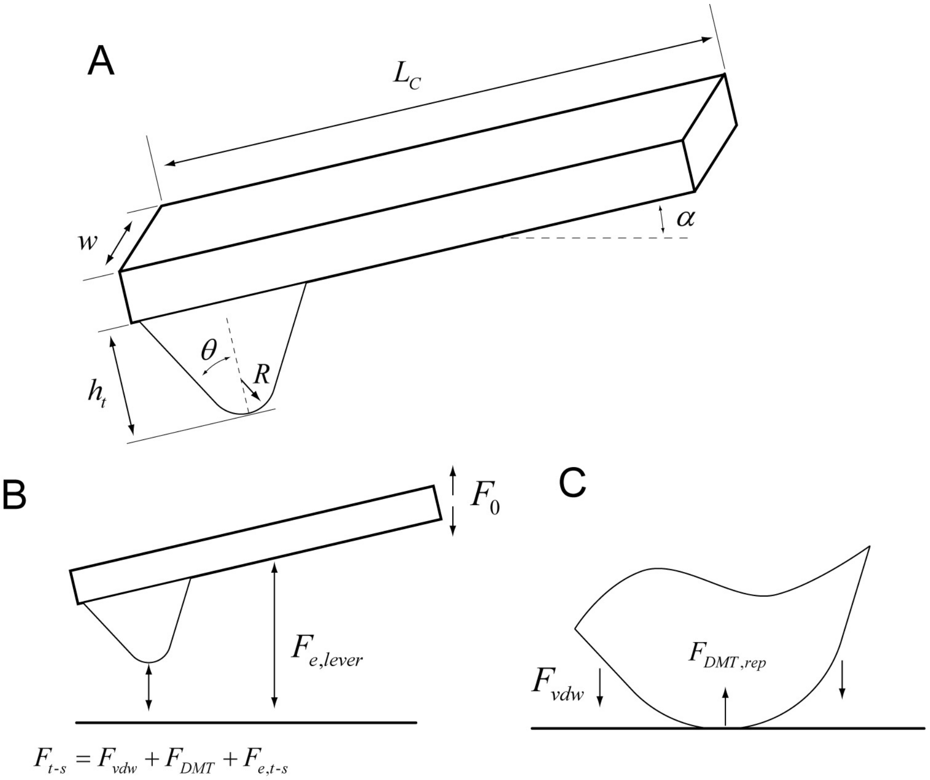

Figure 2.6: (A) Relevant cantilever dimensions used for modeling tip-surface force interaction during dAFM electrical contact cycling. The cantilever tilt angle, α, is 11˚ for the Asylum MFP-3D used in electrical contact cycling. The set of possible, generalized tip-surface, cantilever-surface, and driving force interactions in (B) the out of contact and (C) interpenetrating tip-surface states. (C) Focuses on the tip-surface interaction, which includes both vdw and repulsive DMT interaction forces, but for visualization purposes does not show the electrostatic cantilever interactions that exist in the persistent electrostatic (PE) solution described below.

The tip-surface interactions in eq. 2.8 and the dynamic expression of system motion in eq. 2.6 do not include electrostatic cantilever-sample and tip-sample forces. An additional term to account for electrostatic interaction between the cantilever and sample, $F_{\text{e,lever}}$, is added to the equation of motion to yield

$$m_e \frac{dz^2}{d^2t} = -k_c z - \frac{m_e \omega_0}{Q}\frac{dz}{dt} + F_{t-s} + F_{e,lever} + F_0 \cos(\omega t) \quad \text{Eq. 2.13}$$

The tip-surface force expression is then modified to include the tip-surface electrostatic component, $F_{\text{e,t-s}}$,

$$F_{t-s} = F_{vdw} + F_{DMT} + F_{e,t-s} \quad \text{Eq. 2.14}$$

The specific form of the electrostatic tip-sample interaction used here was developed by Hudlet *et al*.[75] and has been previously used to investigate electrostatic effects during static AFM measurements by Law and Rieutord [76]. This electrostatic tip-surface force expression is a simplification of the exact, but more computationally intensive solution, for the electrostatic force between a sphere and a flat, infinite plane based on the method of images. Hudlet *et al.* [75] showed that this simplified expression matches within 10% of the exact solution for tip-surface separations of 1 Å to 1 μm with the largest deviations for large separations (>10 nm) that are expected to have a negligible impact on tip-surface dynamics. This representation of tip-surface electrostatic interaction also integrates terms for the electrostatic force due to a conical tip shank and is shown as

$$F_{e,ts}\left(z^*\right) = -\pi\varepsilon_0 V^2 \times \left[\left(\frac{1}{\ln\left(\tan\theta\right)}\right)^2 \left(\ln\left(\frac{h_t}{z^* + Ru}\right) + \frac{R\cos^2\theta}{\sin\theta\left(z^* + Ru\right)} - 1\right) - \frac{R^2 u}{z^*\left(z^* + Ru\right)}\right] \quad \text{Eq. 2.15}$$

and, $u = 1 - \sin\theta$

where ε_0 is the permittivity of free space, V is the voltage difference between the tip and surface, θ is the cone angle of the AFM probe tip shank, and h_t is the height of the tip shank.

Hudlet *et al*. [75] found that the electrostatic interaction of the cantilever and the surface can have a measureable effect on cantilever-surface force interactions. The magnitude of this interaction approaches that of the tip-surface vdw interaction in the presence of sharp tips and high voltages (see figure 2.5). Using the formulation presented by Hudlet *et al*. [75], the cantilever-surface force expression is

$$F_{e,lever}\left(z^{*}\right)=-\pi\varepsilon_{0}V^{2}\frac{1}{2\pi}\frac{L_{C}w}{\left(z^{*}+h_{t}\right)^{2}}\left(1+\frac{L_{C}}{z^{*}+h_{t}}\tan\alpha\right)^{-1} \qquad \text{Eq. 2.16}$$

where L_c is the length of the cantilever and α is the angle of the cantilever with respect to the sample.

Two cases are considered that depend on the nature of the electrical time constant of the contact. If the capacitance, inductance, and resistance at the contact are sufficiently high – for instance, due to large tip-surface resistances and the presence of the logarithmic current amplifier described in section 2.2 – then contact time during tip-surface interaction may not sufficient for the surface charges to equilibrate. This situation is termed a persistent electrostatic (PE) interaction here, meaning the influence of tip-surface electrostatic interaction persists while the tip and surface are both separated and experiencing interpenetrating contact. If the electrical time constant is low and interaction occurs over time periods exceeding the electrical time constant of the circuit, then the potential difference across the contact will equilibrate with the ultimate lower bound for infinitely conductive contact expressing no voltage/charge differential between the tip and surface, $\Delta V_c = 0$. This is termed a non-persistent electrostatic (NE) interaction. These two scenarios bound the possible ranges to tip-surface interaction force under the influence of an electrostatic force.

When the instantaneous position of the cantilever is such that the probe tip is not in direct contact with the surface, both the PE and NE solution take the same form

$$F_{t-s} = F_{vdw}\left(z\right) + F_{e,ts}\left(z\right) + F_{e,lever}\left(z\right) \qquad d > a_0 \qquad \text{Eq. 2.17}$$

However, upon tip-sample contact, the expressions for the PE and NE solutions diverge and are written as

$$F_{t-s} = \left\{ \begin{matrix} F_{vdw}\left(a_0\right) + F_{DMT}\left(z\right) + F_{e,ts}\left(a_0\right) + F_{e,lever}\left(a_0\right) & \text{PE} \\ F_{vdw}\left(a_0\right) + F_{DMT}\left(z\right) & \text{NE} \end{matrix} \right\} \quad d \leq a_0 \qquad \text{Eq. 2.18}$$

Solutions of the equations of motion developed here were implemented in Matlab using the nonstiff, low order ODE45 solver. An iterative approach with increasing time resolution was implemented in order to minimize computation time while maintaining high solution accuracy. With this approach, solution time steps were iteratively increased from 2^4 steps/period to 2^9 steps/period with a window of 5 periods for each solver step. The relative tolerance of the ODE solver was set to 1×10^{-7} and the absolute tolerance of position and velocity were both set to 1×10^{-8}.

Solutions of the ODE at a particular time step were carried out until steady state response was achieved. Convergence of the peak repulsive force and peak repulsive stress were tracked. It was found (see figure 2.7) that approximately 30 evaluations at each evaluation resolution resulted in convergence. Therefore, 35 evaluations at each step were used for all data presented in this work. In order to ensure accurate determination of contact phenomena, the contact zone of the final solution was linearly interpolated to 40,000 points. Contact forces, stresses, time, tip-surface interpenetration, contact radius at peak load, and contact time were then tabulated. Typical solution times were on the order of 30 sec. to several minutes.

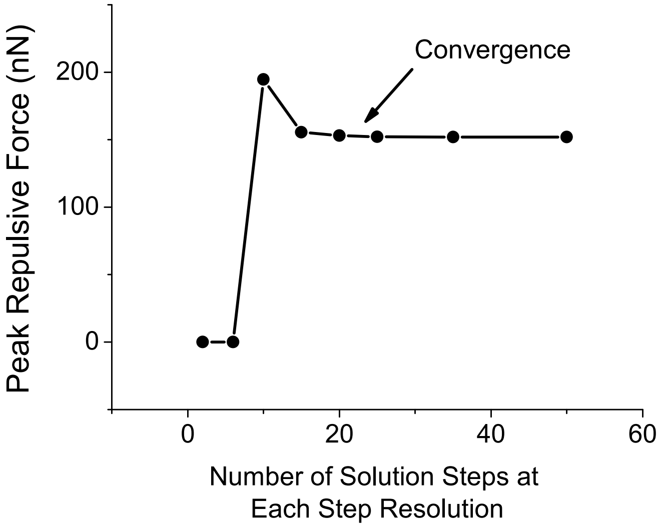

Figure 2.7: Convergence of A_d for tip-surface interaction modeled in Matlab for tip-surface interaction parameters corresponding to measurement D1 in section 3.4.1.

2.2 Current Amplification during Atomic Force Microscopy

Two current amplifiers were used to collect electrical data during C-AFM data collection. An add-on module, the extended TUNA module (Brukar, Camarillo CA, formerly Veeco) was used to measure current on the Dimension 3100 AFM and a custom-built logarithmic amplifier was used with the Asylum MFP-3D AFM. The TUNA module has a linear response function with a noise floor of approximately 1 pA, selectable amplification of 10^8 and 10^{10} V/A, a bandwidth of 160 Hz, and a maximum current response of 1 nA and 100 nA that depends on the gain range selected. The logarithmic amplifier has a nearly log-linear response function at large currents (>15 nA) but is nonlinear at low currents. For this reason, a lookup table was used to convert the amplifier voltage output to current during data collection post processing using Matlab-based routines. The logarithmic amplifier features a noise floor of approximately 40 pA and a 3 dB bandwidth of approximately 176 Hz. Figure 2.8 shows the transfer function, Bode gain plot, and a circuit diagram of the logarithmic amplifier.

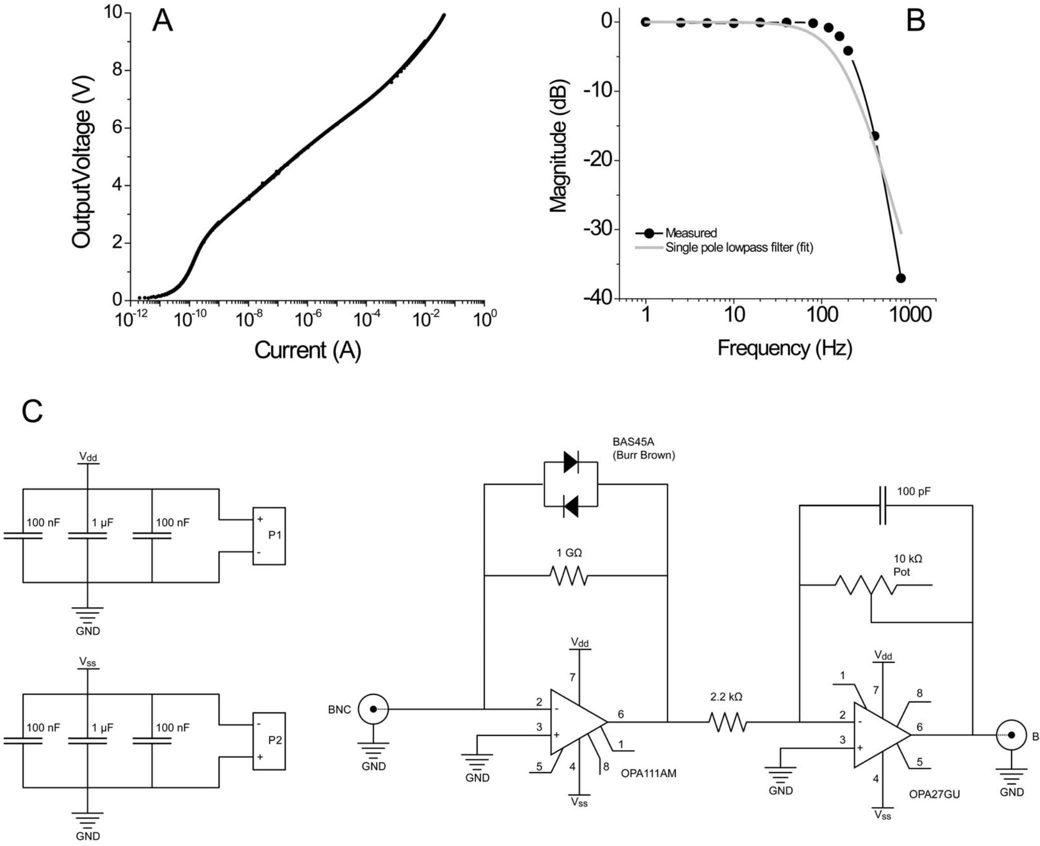

Figure 2.8: (A) Plot of the current-voltage transfer for a custom built-logarithmic amplifier used in this thesis and (B) a bode gain plot of the amplifier response using a 500 MΩ test resister, (C) and a schematic of the logarithmic amplifier circuit.

2.3 Observing the Cantilever Probe Tip Shape

Observation of AFM probe tip enables the extraction of the work of adhesion during AFM-based adhesion measurements, can reveal wear or gross changes to the probe tip apex due to mechanical interaction [70], [81], [82], failure of conductive films [83], and contamination.

Transmission electron microscopy (TEM) was used to determine the AFM probe tip profile along the long axis of the probe using a specialized holder for the contact cycling described in section 2.6. This technique is useful because it provides direct observation of electrical coatings (or lack thereof) and low density contaminants resulting from tip-surface interaction. Fig. 2.9 shows a typical series of images obtained using TEM. The TEM employed was a JEOL 2010with a LaB6 thermionic filament resulting in a 0.25 nm point-to-point resolution. Images were acquired at 200 keV under a vacuum state of 10^{-8} – 10^{-7} Torr.

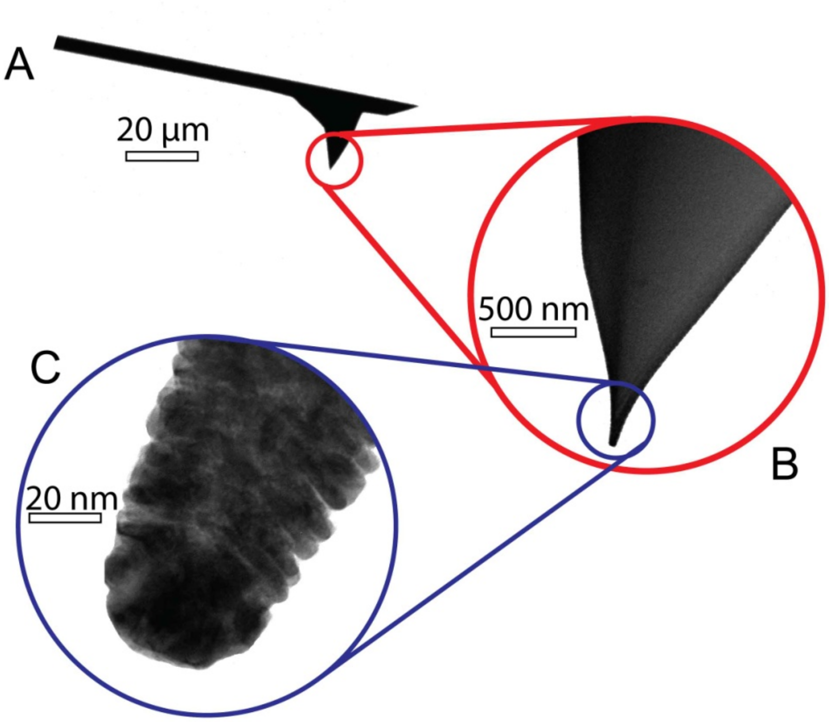

Figure 2.9: (A) Side profile of a Pt-coated AFM probe, (B) an expanded view of the tip shank, and (C) a high-resolution TEM micrograph of the probe tip apex. The angle of the probe tip profile (A) is measured to determine the orientation of the probe tip with respect to the contact surface during AFM. These images are corrected for the probe tip profile as it would make contact with a counter surface in AFM.

A novel fixture was developed to ensure repeatable imaging of probe tip profiles and increase imaging throughput. Several researchers have demonstrated the capability of imaging AFM probe tip apexes using electron imaging techniques [81], [82], [84], [85], [86], [87], [88], [89]. While the probe mounting method utilized in [84], [85], [86], [87], [88], [89] is not clear, Liu *et al*. [81], [82] utilized a custom fabricated aluminum insert to view probe tip profiles. This probe mounting method suffered from several drawbacks. Fixture of the AFM probe utilized carbon tape, which can act as a source of contamination in the TEM that, when combined with the imaging beam energy, could result in deposition of carbonaceous contamination on the tip. The vertical alignment of the probe body was subject to placement by the researcher on the carbon tape complicating repeatable viewing of the same profile position. Additionally, the fixture only provided a slot for a single probe tip meaning time consuming insertion, pumpdown, and extraction of the probe tip needed to be performed for each probe tip imaged.

The new fixture developed at the University of Pennsylvania[4] reduces previous sources of error and contamination. The fixture includes 3 slots for AFM probes and a cutout for holey carbon grids used in instrument alignment. This time-saving feature means that alignment of the instrument and subsequent imaging of 3 tips can be performed before extraction and re-insertion of the probes. The AFM probes are secured in their imaging positions using set screws eliminating the need for carbon tape. The channels into which the probe bodies are inserted were milled flat to serve as a fiducials resulting in repeatable tip profiles and circumventing errors due to in-plane angle alignment differences. Cutouts on each side of the AFM body slot allow access to tweezer tips for easy insertion and removal of the probe chips. An aluminum TEM holder mount was also fabricated to stabilize the TEM probe holder during insertion and extraction of probe tips. This mount includes a channel to hold the AFM chip with a tweezer access channel running to either side and below the chip. This allows the user to choose a tweezer grip on the cantilever that is most suitable for the mounting position desired.

---

[4] The TEM multiprobe holder was developed in collaboration with Dr. Tevis Jacobs (University of Pennsylvania) and Alex Goodman (then a senior at The Haverford School, Haverford, PA).

Extraction of the tip profile was performed using Matlab processing of the TEM images. Because the probe is fixed at an 11˚ angle with respect to the sample surface in the AFM, images were obtained using low resolution TEM (2000X) of the cantilever to align the AFM profile to that of its orientation in the AFM. High resolution, angle corrected profiles of the TEM probe tip were then traced with user selected points in Matlab. A least squares fit to the user selected points was then extracted to determine probe tip radii. Upper and lower bounds of tip radii were calculated from tip profile fits from points 0.3 to 5 nm depth into the cantilever tip and with an angle rotation of +/-1˚ to account for inaccuracies in position between TEM and AFM mounting. The average probe tip profile was then determined from the average of all measurements under rotation and evaluation depth.

2.4 Observing the Chemical State of Electrical Contact Surfaces using Chemical Spectroscopy

Both X-ray photoelectron spectroscopy (XPS) and photoemission electron microscopy (PEEM) were used to interrogate the chemical identity of counter surfaces tested in this thesis. XPS was used to measure the thickness and chemical constituents of adsorbed contaminants on Pt surfaces used for AFM cycling experiments. PEEM was employed to observe the chemical state of nitrogen-incorporated ultrananocrystalline diamond (N-UNCD) exposed to load, shear, and electrical bias. This section describes the instrumentation and normalization methods used during these measurements.

2.4.1 XPS Spectroscopy to Interrogate Surface Chemical Composition of Platinum Films

XPS was employed to interrogate the chemical composition of flat Pt surfaces[5] used as counter-samples in electrical cycling tests described in section 2.6. XPS is a surface sensitive spectroscopy technique that reveals the elemental composition of the first few nm (~10 nm) of a surface [90]. The details of the XPS system used in the present work can be found in [91]. Briefly, Al K*α* X-rays, produced by bombarding an Al source with a highly-focused electron beam, are focused by a quartz-crystal monochromator onto the sample surface. The X-ray beam size is approximately 1 x 3 mm^2. The electrons photoemitted from the sample are collected with an electrostatic lens. After passing the hemispherical analyzer, the photoelectrons are detected by a MCP/CCD detector.

Survey scans were first performed with a 200 eV pass energy, 1 eV step size, and a 1.3 mm straight analyzer entrance slit. These were followed by high resolution scans of the carbon, oxygen, and platinum peaks captured with a 100 eV pass energy, 0.05 eV step size, and a 0.8 mm curved analyzer entrance slit. In all cases, the X-ray source was run at 30 mA current and 12 kV accelerating voltage, while the analyzer was operated in constant-analyzer-energy mode. The pressure in the analysis chamber was maintained below $8x10^{-9}$ Torr. The XPS system was calibrated in accordance with ISO 15472:2001 to an accuracy of ±0.05 eV. The high resolution spectra were processed using CasaXPS software (v2.3.16, Casa Software Ltd., Wilmslow, Cheshire, U.K.). An iterated Shirley-Sherwood background subtraction was applied before peak fitting using a linear least-squares algorithm.

Since the samples under investigation exhibited a layered structure, *i.e.*, a first layer made of platinum and an overlayer made of carbon and oxygen that derives from the exposure of the specimen to air, a model was applied to estimate the thickness and composition of the overlayer (the substrate was assumed to be semi-infinite and to consist of pure platinum). Seah [92, Ch. 13] and Fadley [93] developed equations that correlate the areas of the photoelectron

---

[5] This work was performed in conjunction with Dr. Filippo Mangolini (University of Pennsylvania).

peaks to the concentration of the corresponding element in the case of multilayer systems, under the assumption that electrons from a discrete layer are attenuated by the layer itself and any overlayers (Beer-Lambert law). Such analysis has been performed for similar systems of engineering materials [94]. The model also assumes each layer to be homogeneous in thickness and composition. The system of non-linear equations were solved numerically using Mathematica (Wolfram Research, Champaign, Illinois, US), allowing the thickness and composition of the overlayer to be computed. In the present case, the integrated intensity of the peaks contributing to the high resolution spectra were corrected, after background subtraction, using sensitivity factors calculated from the Scofield photoionization cross-section [95], the angular asymmetry factor [96], the spectrometer transmission function, and the inelastic mean free path [92, Ch. 11].

2.4.2 PEEM Spectromicroscopy to Interrogate the Surface Chemical Composition of Conductive Diamond Films

PEEM was used in section 2.7 to investigate changes to the surface chemistry of N-UNCD arising from interaction with Pt-coated AFM probes under load, shear, and electrical bias[6]. PEEM measurements were undertaken at the Advanced Light Source (ALS) in Berkeley, CA using the PEEM2 end station located on beamline 7.3.1.1. The measurement technique consists of directing a beam of monochromated X-rays at a sample under high negative bias (-10 to 15 kV). By varying the energy of the incident X-rays, the total number of emitted Auger and secondary electrons increases if the core electron is excited into an unoccupied state, giving a peak. The excitation energy (peak location) gives detailed information on the identity of the excited atom and its chemical state. Because Auger and secondary electrons have low kinetic energy and quickly lose this energy due to inelastic collisions, chemical information is obtained from the surface (top 3 - 10 nm) of the sample surface [97]. By collecting the spatially resolved

---

[6] This work was performed in collaboration with Dr. Andrew R. Konicek (now with Exxon Mobil Research & Engineering Company, Corporate Strategic Research, Annandale, NJ and formerly with the department of Physics and Astronomy, University Pennsylvania).

intensity of emitted electrons at each point on the sample surface, a three dimensional cube of data is formed that represents distance in the x-y dimensions and incident x-ray energy in the z-dimension. Using this technique, chemical spectra can be resolved for regions down to a lateral resolution of 50 nm [97]. Previous measurements, using PEEM at the ALS, of un-doped UNCD surfaces have successfully identified differences in sp^2 and sp^3 bonding as reported by Konicek *et al*. [98].

Chemical spectra were obtained for th C1s, O1s, and N1s edges of N-UNCD corresponding to energy ranges of 270 – 300 eV, 520 – 570 eV, 385 – 435 eV, respectively. Spectra collected at different time points and different sample surface locations are subject to variations in the beam dispersion, synchrotron ring current, monochromator, and system contamination. Therefore, the normalization technique described by Konicek [99] was used in order to quantitatively compare spectra obtained at different test locations. Briefly, a Pt-coated silicon sample was used as normalization. Spectra were obtained on this sample using identical conditions to all other measurements. Spectrum normalization was achieved by extracting a spectrum from a sample data stack, and the using the exact same region of interest on the platinum data stack in order to account for beam energy dispersion. Both the raw N-UNCD and Pt spectra were divided by the average value of the pre-edge region of the spectrum. N-UNCD spectra were then divided by the normalized Pt spectra and pre edge set to zero.

2.5 Deposition of Electrical Contact Materials

Thin films of platinum and nitrogen-incorporated ultrananocrystalline diamond (N-UNCD) were employed extensively in this thesis. Pt films <100 nm in thickness were utilized in all major studies here. Section 2.7 describes testing primarily focused on N-UNCD, a conductive variant of diamond with potential for use in ohmic switching systems. This section describes the methods used to deposit Pt and N-UNCD.

2.5.1 Sputtering of Platinum films

All Pt films investigated in this thesis were deposited via sputtering. Both a bench-top vacuum sputter coater, EMITech K575X (Quorum Technologies, Ashford, Kent, United Kingdom), and a standalone full-wafer sputter system, Denton Explorer14 (Denton Vacuum, Moorestown, NJ), were employed. Pt targets with a purity of 99.99% were employed for Pt deposition in both the EMITech K575 and Explorer14 sputter coaters. Depositions in the EMITech K575X were performed with a sputtering current of ~40 mA, with a pressure during deposition of approximately 3×10^{-3} Torr, and a deposition rate of 1 – 2 Å/sec. All depositions in the Explorer14 were performed with a sputtering power of 450 W, an Ar gas flow rate of 25 sccm, were begun after reaching a base pressure of 2×10^{-6} – 5×10^{-6} Torr, and the deposition rate was measured to be ~4.3 Å/sec. The Explorer14 sputterer features a rotating turntable that was set to a rotation speed of 50% for all depositions. The deposition rates for each system were determined from patterned step edges measured with a Zygo New View 3100 white light interferometer (Zygo Corporation, Middlefield, CT, United States).

2.5.2 MPECVD Deposition of Nitrogen-incorporated Ultrananocrystalline Diamond

The N-UNCD film investigated in section 2.7 was deposited using a Cyrranus I large-area reactor from IPLAS (Innovative Plasma Systems, gmbh, Troisdorf, Germany). Growth was performed at 1189W for 50 mins. with a substrate temperature of ~796˚C, resulting in an expected N-UNCD film thickness of 1 µm. This film is referred to as 5% N-UNCD, owing to a 5 sccm (5% of total gas flow) of N_2 during the growth process [100], which included 94.2 sccm of Ar and 0.8 sccm of CH_4 all at 112 Torr. The addition on N_2 during the growth process changes the electronic structure of the grain boundaries that renders this normally insulating film conductive [100], [101]. The expected concentration of N in the resulting film was expected to be ~1.7 atoms/cm^3 or ~0.2% total content by weight. The film was deposited on a quartz wafer.

2.6 Method for the Gigacycle Interrogation of Single Asperity Electrical Contacts Using Atomic Force Microscopy

Existing electrical contact characterization techniques suffer from low throughput, are limited in the types of contact materials that can be tested, are amenable to only microscale, multiasperity contacts, or can only achieve a fraction of the number of interaction cycles necessary for demonstration of materials performance for MEMS and NEMS switches. This section describes the development of a high-throughput, low cost technique to investigate electrical contacts at the fundamental limit of the contact – the single asperity – using AFM for up to several billion cycles. This method is particularly attractive because the types of materials that can be investigated are only dependent on the ability to deposit them as thin films on AFM probes and flat substrates. Furthermore, the ubiquity of AFM instrumentation at most research facilities lends the method described here to wide adoption. While the testing described here is performed in laboratory air or N_2 purged environments at standard pressure, the existence of highly, isolated ultra high vacuum systems could enable extension of this methodology to ultraclean environments and testing under the addition of known contaminants with known partial pressures in order to simulate specific operating environments.

Of great interest for NEMS logic switch is the evolution of a single asperity electrical contact. This is the fundamental unit of a multiasperity contact and represents the ultimate limit of an ohmic NEMS logic switch contact. The contact resistance (conductivity) and adhesion of the contact has dramatic implications for device energy consumption and lifetime. High contact resistances result in undesirable power dissipation and slow electrical time constants. Contacts that are highly adhesive may exceed the restoring force of a NEMS logic switch resulting in permanent closure of the contact. Due to the nascent history of NEMS device development, no studies of nanoscale electrical contact reliability that mimic NEMS switching behavior exist. With this motivation, protocols were developed using C-AFM and dAFM to cycle a single asperity contacts up to several billion cycles in laboratory timeframes (10-16 hours) while observing changes to the conductivity and adhesion of the interface.

The contact cycling method described here attempts replicate the mechanical interaction that occurs in a typical nanoscale electrical switch contact. Closure of the electrical contact interface in most micro- and nanoscale switches occurs normal to the face of the contacts resulting in minimal lateral displacement. To replicate this behavior, experimental parameters and the AFM cantilever type have been selected to minimize shear displacement during testing within the limitations of the AFM systems employed. The AFM testing protocol is now be described in detail.

2.6.1 Detailed Single Asperity Cycling Test Protocol

Two protocols were developed to cycle electrical contacts, referred to in subsequent sections as “protocol 1” (P1) and “protocol 2” (P2) with P2 representing a mature, improved version of P1. Figure 2.10 shows a diagram of the two protocols from beginning to end and table 2.1 details improvements instituted for protocol P2. The protocols described below were performed on an Asylum MFP-3D AFM (see section 2.1.2 for a description of the instrument) and conductivity during the test was evaluated using a custom-built logarithmic amplifier described in section 2.2. The large current range of this amplifier permits the observation of conductivity changes over several orders of magnitude. The protocols used to interrogate the robustness and lifetime of electrical contact materials using AFM are now described in detail.

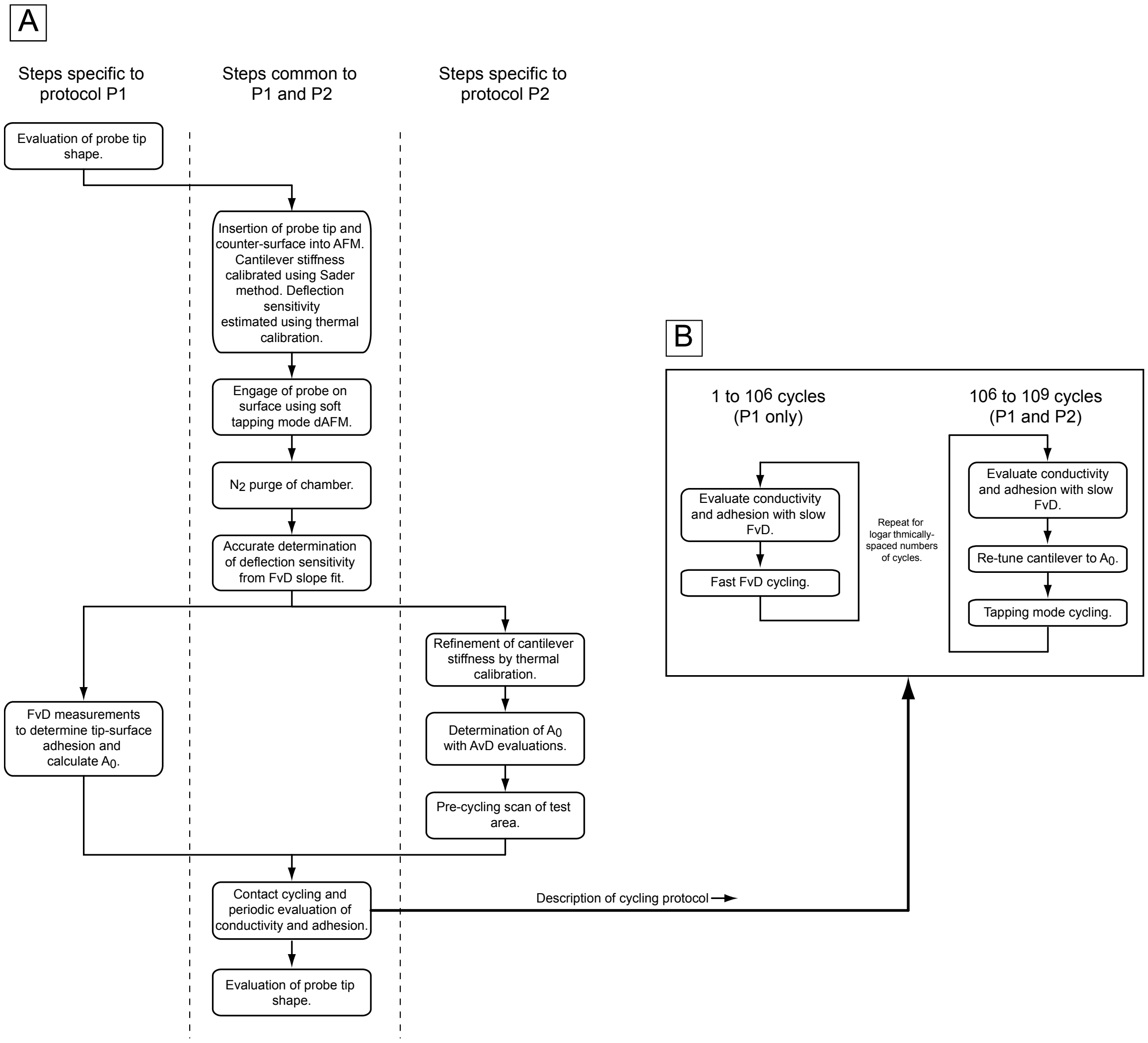

Figure 2.10: The protocol used to cycle and interrogate the conductivity and adhesion of nanoscale electrical contacts. (A) Details of the testing process from start to finish. Steps specific to protocol P1 (left), protocol P2 (right), and both protocols (center) are identified. (B) Details of the cycling and interrogation steps. The tip-surface contact is cycled at high speed and cycling stopped periodically to perform a low frequency evaluation of tip-surface conductivity and adhesion.

Table 2.1: Comparison of the two protocols used in the cycling of nanoscale electrical contacts for up to 2 billion cycles. Protocol 1 (P1) was used to investigate the contact from a few cycles up to several billion cycles. Protocol 2 (P2) focused on $10^6 – 10^9$ interaction cycles. The number of points during the periodic evaluation of interface conductivity and adhesion was increased substantially from P1 to P2 in order to improve the statistical interpretation of data.

Test feature	**Protocol P1**	**Protocol P2**
Early lifetime cycling ($<10^6$ cycles)	FvDs performed at ~10 Hz	None
Early lifetime cycling area	Single point	n/a
Maximum force during cycling FvDs (nN)	15	n/a
Maximum force during interrogation FvDs (nN)	15	40
Voltage between tip-sample during interrogation FvDs (mV)	50	200
Damping ratio during dAFM cycling	0.57, near peak repulsive force	0.25
Number of interrogation FvDs for each force map	25	1256
Size of lateral scan region before cycling	None	2 x 2 μm^2
Determination of K	Sader calibration using manufacturer's specification of cantilever dimensions	Thermal calibration

For protocol P1, testing began with TEM imaging of the probe tip profile to determine the contact radius. This radius was used in the closed form equation of Hu & Raman [71] to prescribe interaction force (by prescribing A_0) during dAFM testing. In order to increase throughput and ensure interpenetrating contact, this step was excluded from protocol P2 and A_0 was determined experimentally (discussed later). The AFM probe and counter sample were then loaded into the AFM and the laser and photodiode were aligned. At this juncture, both the stiffness, K_{cant}, and the deflection sensitivity, S, of the cantilever were unknown, which together determine the loading force during static tip-surface interaction. To avoid subjecting the probe to large or unknown forces, the method described in section 2.1.3 was used to estimate *K* and *S* without touching the sample surface.

The probe was then gently engaged with the surface. Setup of the probe and surface at this point had occurred with the probe retracted several millimeters from the sample surface. The cantilever must be brought into vertical registration with the surface using a coarse mechanical approach such that the piezoelectric scanner can control tip surface interaction (tip-surface separated by only several microns). Engagement of the surface using dAFM is preferred over static methods to decrease engage time and limit tip-surface interactions. dAFM is later used to cycle the contact, however, cycling at this juncture was not desired since deflection sensitivity and, in the case of protocol P2, lateral scanning of the surface, need to be performed. In order to avoid large tip-surface stresses, or rather, unintended cycling of the contact, a soft engage approach was employed [102].

The soft engage process was initiated by performing a frequency-amplitude sweep of the probe while retracted several mm from the surface (to ensure the cantilever was free of tip-surface forces). The free air amplitude, A_0, was then chosen low enough to ensure tip-surface forces were primarily in the attractive regime in order to minimize the effects of tip-surface cycling. Typically, a value of $A_0 < 70$ nm was sufficient to ensure attractive tapping interaction for the probes used in this study. A_d was specified as approximately $0.95 \mathrm{x} A_0$ and the relative tip-surface separation was reduced using manual coarse approach until this amplitude damping level was achieved. This represents a “false engage” of the surface as the tip was still several μm from touching the surface. In an alternating fashion, the coarse z-position of the tip was reduced and A_d swept from 1 to ~0.8 until evidence of intimate contact between the tip and sample was observed. Because A_0 was chosen to be relatively small, phase during this initial contact was >90˚, suggesting tip-surface forces are primarily adhesive and minimal. The cantilever was then retracted from the surface and the system purged with N_2.

The deflection sensitivity and stiffness of the probe were then refined. The slope of lightly loaded FvD measurements (load set lower than during testing, so as to not “cycle” or damage the interface) was fit to accurately determine the deflection sensitivity. The probe was then retracted and, in the case of P2, thermal calibration was performed to refine the probe stiffness calibration.

The free air amplitude during dAFM contact cycling was then determined by theory for protocol P1 and experimentally for protocol P2. For protocol P1, the initial adhesion of the interface was determined by performing a 6x6 measurement array of FvD measurements over a 1 x 1 μm^2 region of the test surface. The average adhesion and the probe tip radius from initial TEM measurements were then used to calculate the necessary free air amplitude during dAFM using the closed form equation of Hu and Raman [71] with A_r fixed to the location of peak interaction force of ~0.58.

The observation of phase angles above 90˚ during dAFM cycling in protocol P1, which infers attractive mode interactions, led to the adoption of an experimentally-based selection of A_0 in protocol P2. For protocol P2, amplitude versus distance curves (AvD) were performed with increasing A_0 to determine the transition from soft to hard tapping mode interaction before dAFM cycling. As shown in figure 2.11, an initial amplitude of 100 – 150 nm was specified and stepped by increments of 10 nm until a phase below 90˚ for $0.2 \leq A_r \leq 0.8$ was observed. The amplitude value at this point was then increased by 150% to ensure repulsive mode interaction. A_r during protocol P2 testing was fixed at 0.25, which although was not the A_r corresponding to maximum tip-surface force interaction, ensures hard tapping mode interaction for the duration of the test.

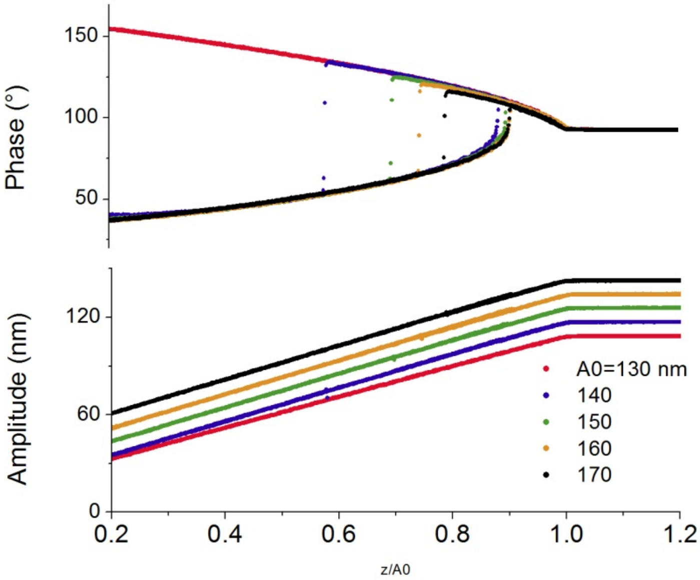

Figure 2.11: Amplitude (top) and phase (bottom) from amplitude versus distance (AvD) curves of increasing free air amplitude, A_0, taken before testing for cycling protocol P2 between a Pt-coated AFM probe tip and a Pt counter sample. The emergence of $\varphi < 90^\circ$ for $0.2<A_r<0.8$ suggests a transition from attractive tapping mode ($\varphi > 90^\circ$) to repulsive tapping mode ($\varphi < 90^\circ$). The final A_0 used for testing in protocol P2 was taken from the first, stable observation of $\varphi < 90^\circ$ for approximately $0.2<A_r<0.8$. This A_0 value was then increased by 150% to ensure hard tapping mode interaction for the duration of dAFM cycling.

Lateral scanning of the tip-surface interface before contact cycling was implemented in protocol P2. For protocol P1, it was observed that a significant number of initial tip-surface interactions demonstrated high resistance at the beginning of the test (these tests were abandoned and are not described in results chapter 3). This was hypothesized to originate from adsorbed contaminant layers on the tip and surface. Lateral cleaning scans were added to protocol P2 in order to agitate the tip/surface and improve the initial conductivity of the interface. Lateral AFM scans have previously demonstrated contaminant buildup at the edge of the scan. This occurs because the sudden change in the tip raster direction at the edge of the scan can result in deposition of contaminants that adhered to the tip during scanning. This can act as a source of contamination during tip-surface cycling that is not representative of contact fouling in a real switch electrical contact. Therefore, initial lateral scanning was performed over 2 x 2 μm^2 window, which places the edge of the cleaning scan outside of the cycling location. Figure 2.12 shows the relative locations of the cleaning scan window and the cycling regions. Three lateral scans were performed before cycling at 15 nN applied load, a scan rate of 1 Hz, and for 256 scan lines. Multiple scans were chosen so that steady state conductivity between the tip and surface was observed before beginning cycling.

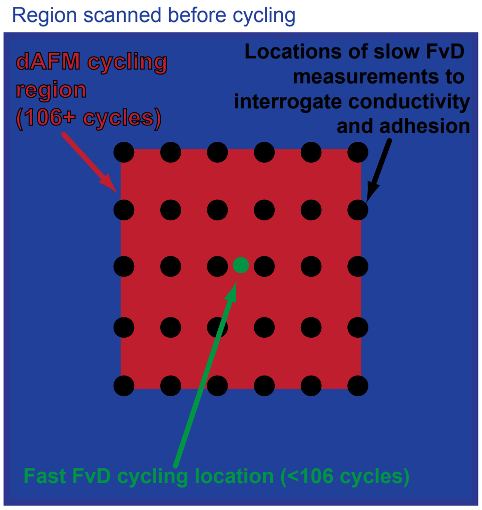

Figure 2.12: The relative location of cycling and conductivity and adhesion evaluations. dAFM cycling (red) was performed across a 1 x 1 μm2 window for protocol P2 and at the center of the test region (green circle) for protocol P1. Slow FvD interrogation measurements (black circles) were performed for both protocols P1 and P2. This representation shows 25 FvD measurements. However, up to 1156 FvD regularly spaced measurements were conducted during protocol P2. Lateral scanning of the test area (blue region) was performed before cycling during protocol P2.

Cycling of the contact and evaluation of tip-surface conductivity and adhesion was then undertaken. This process entailed cycling the contact for a specified number of contact cycles using fast FvD measurements (~10 Hz) for <10^6 cycles and dAFM interaction with the surface at the resonant frequency of the probe (~40-75 kHz) for >10^6 cycles. These fast cycling speeds ensure that upwards of 2 billion cycles can be achieved in a 10-16 hour testing period. At logarithmically-spaced cycling points, cycling of the tip is stopped and slower FvD measurements were performed to reveal the conductivity and adhesion of the interface. The need for slower FvDs to evaluate of the conductivity of the contact was ther esult of the limited bandwidth of the current amplifier such that collection of meaningful conductivity information could not be gained from measurements taken during fast FvD and dAFM cycling.

Cycling of the contact for 10^6 to several billion cycles was achieved using dAFM for both protocols P1 and P2. To do so, the probe was tuned to a user specified free air amplitude, A_0, at its resonant frequency (40-75 kHz for the probes used in this study) while several µm from the surface. This ensured that tip surface interactions are negligible. The probe was then engaged with the surface at a user specified damping ratio, A_r, at which point cycling had commenced. Knowledge of the probe tip radius, the mechanical properties of the interface, and the free air amplitude were used to determine the maximum loading force (peak interaction force) during the tip-surface interaction. Surface scans of Pt surfaces demonstrated variations in surface conductivity spanning several orders of resistance and having a periodicity of 10-20 nm. Thus, the dAFM cycling region was moved from a central location in protocol P1 to a 1 x 1 μm^2 window for protocol P2 in order to sample the average tip-surface condition. The raster rate and number of scan lines was adjusted to achieve a predetermined number of interaction cycles with a maximum scan rate of 5 Hz and a minimum of 64 scan lines.

Probe cycling was performed strictly with dAFM in protocol P2 in order to focus on changes that occurred from 10^6 – 10^9 cycles. However, protocol P1 included early lifetime cycling in order to demonstrate the ability to resolve changes to the nanoscale electrical contacts from just a few cycles up to several billion. Because the minimum number of cycles that may be achieved using dAFM-based cycling is on the order of 10^5 - 10^6 cycles[7], FvDs measurements

---

[7] In a dAFM measurement of a surface, simply engaging and retracting from the surface takes on the order of 1 second, which results in f_0 x 1 sec. interactions. For the probes used in this study, 40 kHz ≤ f_0 ≤ 75 kHz. Additionally, a maximum raster rate of 5 Hz was enforced to avoid instabilities in surface tracking that would result in unstable interaction forces over the measurement regions. The minimum number of scan lines during all measurements was 64. Therefore, the minimum number of interaction cycles achievable with during one interaction period using dAFM is

near the maximum displacement rate of the AFM system used here (~10 Hz, 4000 nm/s vertical displacement rate) were performed to determine early lifetime behavior and are referred to as "cycling FvDs". FvD cycling was performed at the center of the test location, although advanced programming of AFM functionality could enable FvD cycling over an array of locations like that achieved for dAFM cycling.

Slow FvD measurements (referred to here as "probing FvDs") at a speed of 100 – 200 nm/s in the vertical were performed to periodically evaluate the conductivity and adhesion of the interface. Because the Pt surfaces investigated with this test method demonstrated surface conductivity with a log-normal distribution, tip-surface conductivity and adhesion was evaluated using a regularly-spaced grid of measurements locations over a 1 x 1 μm^2 area. Thus, the average tip-surface condition is reported. For protocol P1, 25 points were recorded during each evaluation. In order to increase the statistical significance of the data, this was increased to 1156 points for protocol P2. A probing voltage, V_p, was applied between the tip and surface with the tip serving as the anode in order to evaluate the conductivity of the interface as a function of load. This voltage was chosen low enough so as to not modify the tip but large enough to detect measureable current flow. V_p was set to 50 mV for protocol P1 and increased to 200 mV for protocol P2. The maximum loading force during the probing FvDs was set to 15 nN in protocol P1 and 40 nN in protocol P2.

The final shape of the probe tip was then evaluated after approximately 2 billion contact cycles. For protocol P1, high-resolution TEM imaging was also used to inspect for evidence of wear or the formation of contamination (TP).

The test method employed for both protocol P1 and P2 were automated using Igor scripting on the Asylum MFP-3D.

$f_0 \times \left((\text{no. scan lines}) \times \frac{1}{\text{scan rate}} + \left(\text{time to engage and retract from surface} \right) \right)$, which corresponds to 5.5x10^5 to 1.0x10^6 cycles.

2.6.2 Removal of Insulating Films via Shear Displacement of the Contacts

Contaminant formation resulting in increased contact resistance due to tip-surface interaction was often observed during the single asperity cycling experiments. This contamination was observed to de-adhere from the AFM tip under the action of lateral sliding. In order to investigate the regeneration of nanoscale electrical conductivity under shear loading, a test was performed on a contaminated tip to see if high conductivity could be recovered. The tip was moved to a fresh location of the surface and scanned for 256 scan lines at a load of 15 nN over an area of 2 x 2 µm^2. A 34 x34 grid of FvD measurements were then collected over a 1 x 1 µm^2 area to determine the tip-surface current response after cleaning.

2.6.3 Selection of Cantilever Stiffness and Shear Displacement during Cycling

Practical implementation of cycling and interrogation of a nanoscale electrical contact as described in section 2.6.1 requires appropriate selection of cantilever stiffness. The cantilever stiffness has to be sufficiently soft so as to yield high resolution conductivity as a function of loading force and adhesion data, yet sufficiently stiff so as to achieve tip-surface interpenetration forces relevant to NEMS switch contact during dAFM. These two requirements define a range of acceptable cantilever stiffness.

Several considerations limit the type of AFM probe (probe stiffness) that may be selected for tip-surface electrical cycling contact studies. Because the electrical contact cycling method described here should rely on off-the-shelf components, fabrication of custom cantilevers or force sensing elements should be avoided. In this regard, the most salient considerations when selecting a commercially-produced AFM probe are the shear displacement of the cantilever due to the cantilever-counter surface angle of the AFM, the noise limit of the AFM system as it affects loading and adhesion measurements, and the capability the probe to achieve dAFM cycling under NEMS switch-like forces.

As will be shown in section 3.7, shear forces can have a profound effect on regenerating the conductivity of an electrical contact that has developed an insulating TP. In order to replicate typical NEMS switch functionality, which consists of contact in the normal direction only (no shear), relative lateral movement of the tip-surface should be avoided. Most commercial AFMs have a tilt angle between the tip and surface. For the MFP-3D used during the cycling studies here, this angle is approximately 11˚. Cannara *et al.* [103] have shown that the relative lateral displacement of an AFM probe as a function of vertical displacement when neglecting second order cantilever length effects is

$$\Delta x = \Delta z \tan\left(\alpha\right) \qquad \text{Eq. 2.19}$$

where Δx is the lateral displacement, Δz is the vertical displacement, and α is the cantilever tilt angle. Recall that the vertical displacement to achieve a given load is linearly related to the cantilever stiffness. This implies that stiff cantilevers should be employed to reduce shear effects. Lateral displacement for the largest loads utilized in electrical contact cycling here was limited to 10 nm.

Probes of high stiffness confer less lateral displacement during loading but are subject to increased noise sensitivity. Thermal fluctuations of the cantilever at a finite temperature confer a lower limit to the detectable force threshold, $F_{t,\min}$, of an AFM cantilever [66, p. 93] and can be calculated from equipartition theorem as

$$F_{t,\min} = \sqrt{\frac{2k_B T K_{cant} \Delta\omega}{\pi\omega_0 Q}} \qquad \text{Eq. 2.20}$$

where $\Delta\omega$ is the collection or feedback bandwidth of the AFM system. This minimum force represents the ultimate force sensing limit of any AFM system. In practice, AFM systems are subject to noise from external system vibrations, thermal variations, and noise from electronics that puts the minimum resolvable force orders of magnitude larger than $F_{t,min}$. Measurement of the normal force noise of the AFM system can be related to the minimum measureable force through

$$F_{noise} = K_{cant}\delta_{noise} \quad \text{Eq. 0.1}$$

where δ_{noise} is the measured vertical noise of the system. For the MFP-3D used in these studies, this was conservatively measured with an upper bound of ~0.5 nm.

Because dAFM is used to cycle contacts to replicate NEMS switch electrical contact under repulsive load, the possible range of tip-surface interactions must also be considered. The closed form equation for tip-surface interaction developed by Hu & Raman [71] and based on the simple harmonic model presented in section 2.1.5 provide a useful basis for estimating the maximum repulsive tip-surface interaction force during dAFM for a given cantilever stiffness. Their formulation shows that the peak interaction force increases with increasing K_{cant}. Thus, selection of a soft cantilever may prohibit repulsive forces that match interaction forces expected for NEMS logic switch contacts (several to 100 nN).

The selection criteria described above were used to map the range of interaction forces that may be achieved for a given cantilever stiffness (see figure 2.13). This map shows that the lower limit of cantilever stiffness is bound by concerns of large shear displacements and limitations of tip-surface repulsive force during dAFM. The upper bound of cantilever stiffness is dominated by system noise. However, there exists an optimal window (K_{cant} = 1 – 4 nN/nm) between which forces expected for NEMS switch-like interactions, the generative force during dAFM, lateral displacements limited to <10 nm, and system noise converge to a stiffness corresponding to commercially produced probes. Three major types of AFM cantilevers are commercially available – contact mode of $0.01 \leq K_{cant} \leq 0.4$ nN/nm, force modulation of $1 \leq K_{cant} \leq 5$ nN/nm, and tapping mode of $10 \leq K_{cant} \leq 50$ nN/nm. Force modulation probes of nominal K_{cant} ~ 2.8 nN/nm were, therefore, selected for these studies.

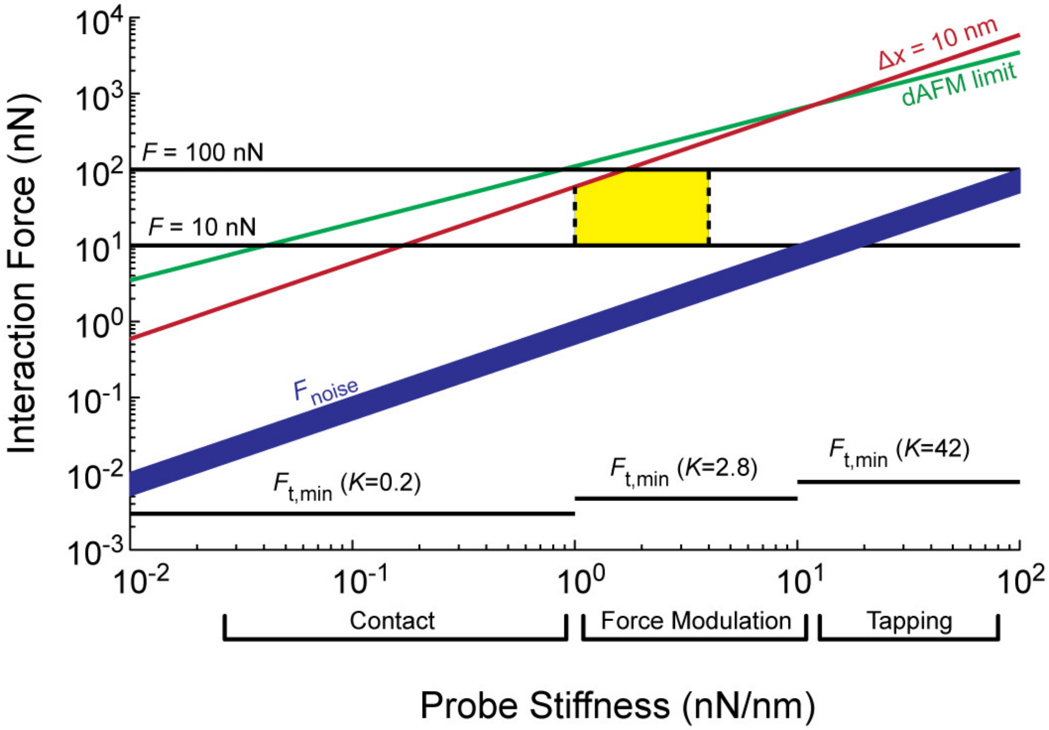

Figure 2.13: Interaction force as a function of AFM probe stiffness is subject to AFM system and lateral displacement constraints. Ranges of cantilever stiffness corresponding to various commercially produced probe styles are listed on the x axis. The requirements of both static AFM and dAFM measurements instruct the necessary probe stiffness for measurements that replicate NEMS switch contacts. The minimum noise floor of an AFM probe due to thermal fluctuations, $F_{t,min}$, is far below the interaction forces required to simulate NEMS contacts. While noise due to mechanical and electrical systems of the AFM, F_{noise}, is more appreciable than thermal noise, it does not limit the type of probe used. For investigations of electrical interfaces with forces from 10 to 100 nN the capability to produce tip-surface interactions using dAFM at reasonable cantilever oscillation amplitudes and the desire to restrict lateral sliding/shear during tip-surface interaction bounds the range of probe stiffness that may be used. The yellow area corresponds to the range of forces investigated and probe stiffness used in this work. For $F_{t,min}$, K_{cant} was fixed to 0.2, 2.8, and 42 nN/nm for contact, force modulation, and tapping cantilever types, respectively. $\Delta\omega$ was conservatively taken to be 100 kHz. A_0 was fixed to 400 nm for the dAFM limit and parameters

reasonable for the Pt/Pt contacts demonstrated in this study were used (R=50 nm, E_t=E_s=130 GPa, v_t=v_s=0.3, Q=200, and A_r=0.58). δ_{noise} was estimated from measurements of noise on the MFP-3D used in experiments presented here and is taken to be 0.5 nm.

Practical concerns not shown in figure 2.13 also bound the range of potential cantilever stiffness that may be employed. For instance, it has been found that performing a frequency amplitude sweep for dAFM on contact mode cantilevers can be problematic, especially with the addition of electrical coatings, which result in sub-optimal resonance peaks. The investigation here is performed at standard pressure. In the ultraclean, ultra high vacuum (UHV) environments, lower system noise would likely enable the use of stiffer (tapping mode) probes, reducing shear, but ringdown and responsiveness with high Q cantilevers would impose its own limit.

3.6.4 Materials Investigated

The electrical cycling protocol described here was used to investigate Pt/Pt interfaces. This material set was chosen because it has been extensively investigated with application to multiasperity, MEMS electrical contacts [50], [104]. In multasperity contacts, Pt has shown abrupt increases in contact resistance due to cycling during lifetimes ranging from 10^5 – 10^8 cycles, a phenomena that should be observable in the 10^9+ cycles achieved using the testing protocol here.

Commercial silicon cantilevers of type PPP-FM (Nanosensors, Neuchatel, Switzerland) were coated with Pt. Both the back (side of laser reflection) and then the front (tip side) of the probes were coated in order to reduce thin-film bending stresses that could render the probes unusable and to enhance the laser reflectivity on the probe. The tip-side of the probes was deposited last in order to avoid the development of sub-optimal Pt films on the tip. For protocol P1, Pt of 45 – 55 nm-thickness and approximately 70 nm-thickness was deposited using a

EMITech K575X bench-top vacuum sputter coater and Explorer14 sputter coater, respectively. In some cases, a thin Ti adhesion layer (2.5 – 5 nm) was deposited before Pt when using the Explorer14 sputter coater. For protocol P2, Pt of approximately 70 nm-thickness was deposited in the Explorer14 sputterer without a Ti adhesion layer.

Two counter-samples were investigated. Pt was deposited on glass cover slides to a thickness of ~50 nm using the Explorer14 sputterer for protocol P1 testing. Pt was co-deposited with probe tips (50 – 70 nm-thickness) on Si 100 wafers in the Explorer14 sputterer for protocol P2 testing. The Pt substrates were tested as deposited within several days to 4 months after deposition and were stored in a dessicator continuously purged with N_2 between testing.

2.6.5 Method to Investigate the Effect of Voltage and Environment on Nanoscale Electrical Contact Lifetime

Electrical contact failure has been observed to depend sensitively on the operating environment at of the contact. The power handling of the switch (voltage and current), the type of switching (mechanical, cold, or hot), and contaminants in the surrounding environment [105] can all have a profound effect on the contact degradation mechanisms and lifetime to failure. The AFM-based gigacycle protocols described in section 2.6.1 were used to investigate changes to the conductivity and adhesion of nanoscale electrical contacts over a wide range of environments in which NEMS logic switch electrical contacts might operate. For protocol P1, testing was performed exclusively in an N_2-purged environment (<4% RH) and voltage between the tip and surface was varied from 0 – 2 V during FvD and dAFM cycling in order to interrogate effects of hot cycling on contact lifetime. The effect of environment and voltage was investigated in protocol P2. Voltages between the tip and surface were set to 0 V (mechanical cycling) and 1 V (hot switching). As the size of NEMS logic switches decrease the operating voltage will trend towards mechanical cycling. Two environments were investigated in protocol P2 – cycling in laboratory air (high RH) and in a N_2-purged environment. Table 2.2 lists the environment during testing for all cycling tests present in this thesis.

Table 2.2: The contact materials, tip-surface voltages, and environment for various single asperity electrical contact cycling tests performed using the AFM-based gigacycle test method. Pt/Pt interfaces were investigated for all tests.

Test series	**Cycling protocol**	**Environment**	**Modification voltage, V_m (V)**
A	P1	N2-purged (<4% RH)	0 – 2
B	P2		0 (mech. cycling)
C	P2	Laboratory air	1 (hot switching)
D	P2	N2-purged (<4% RH)	0 (mech. cycling)
E	P2	Laboratory air	1 (hot switching)

2.6.6 Chemical Interrogation of Platinum Surfaces using X-ray Photoelectron Spectroscopy

XPS (described in section 2.4.1) was used to interrogate two flat Pt surfaces deposited in the Explorer14 sputter coater using the same methods as the AFM probes and substrates for gigacycle testing. One surface was measured as-deposited after approximately 4 months of storage in an N_2-purged desssicator while the other was cleaned with Piranha 10 minutes before insertion in the XPS system. The former represents a surface chemical composition that replicates surfaces interrogated during cycling tests. The latter was used to test the capability of aggressive cleaning to remove contaminant layers from the Pt surface. A Pirahna solution was used because it is known to be aggressive on organic contamination and Morganthaler [106, p. 46] had observed a decrease in surface contamination on Au using a similar cleaning method. In the piranha cleaning method here, the sample was sonicated for 10 min. in a 1:5 mixture of peroxide and sulfuric acid. The sample was then rinsed with DI water and stirred in a DI water bath for ~1 min. The sample was then dried using blowoff from an N_2 liquid dewar.

2.7 Overview: Method for the Evaluation of Nitrogen-incorporated Ultrananocrystalline Diamond and Platinum Exposed to Load, Shear, and Electrical Bias

In the single asperity cycling method presented in section 2.6, it was observed that shear loading of contacts, both in their as-deposited state and after the formation of insulating contaminant films, could be used to regenerate the conductivity of the interface. Shear wiping of the contact could potentially be integrated into NEMS logic switch technology to clean the contact to yield longer device lifetimes. However, it has been observed that shear of contacts can lead to TP formation even for noble metals [105]. Section 2.7.1 describes the investigation of changes to surface conductivity due shear loading and electrical bias using C-AFM for Pt and N-UNCD. N-UNCD is a conductive variant of ultrananocrystalline diamond that has demonstrated promising microscale electrical properties [101], [107], but its robustness under contact and electrical power has not been investigated from the perspective of a nanoscale electrical contact. Section 2.7.2 describes the study of surface chemical changes and reaction products of N-UNCD as a result of shear loading and electrical power through the contact. While changes to N-UNCD under shear and electrical bias were the focus of these studies, tests were also performed on Pt to provide a baseline for comparison to N-UNCD.

2.7.1 Protocol for the Evaluation of Nitrogen-incorporated Ultrananocrystalline Diamond and Platinum Exposed to Load, Shear, and Electrical Bias

In order to investigate the combined effects of shear loading and electrical bias on N-UNCD and Pt, a method to shear contacts while applying a voltage for a period of time over a selected region using C-AFM was developed. The test consists of repeatedly rastering a Pt-coated probe tip over a square surface region while tracking changes to conductivity scanned surface region while periodically evaluating the integrity of the probe tip. Fig. 2.14 shows a high level overview of the test steps.

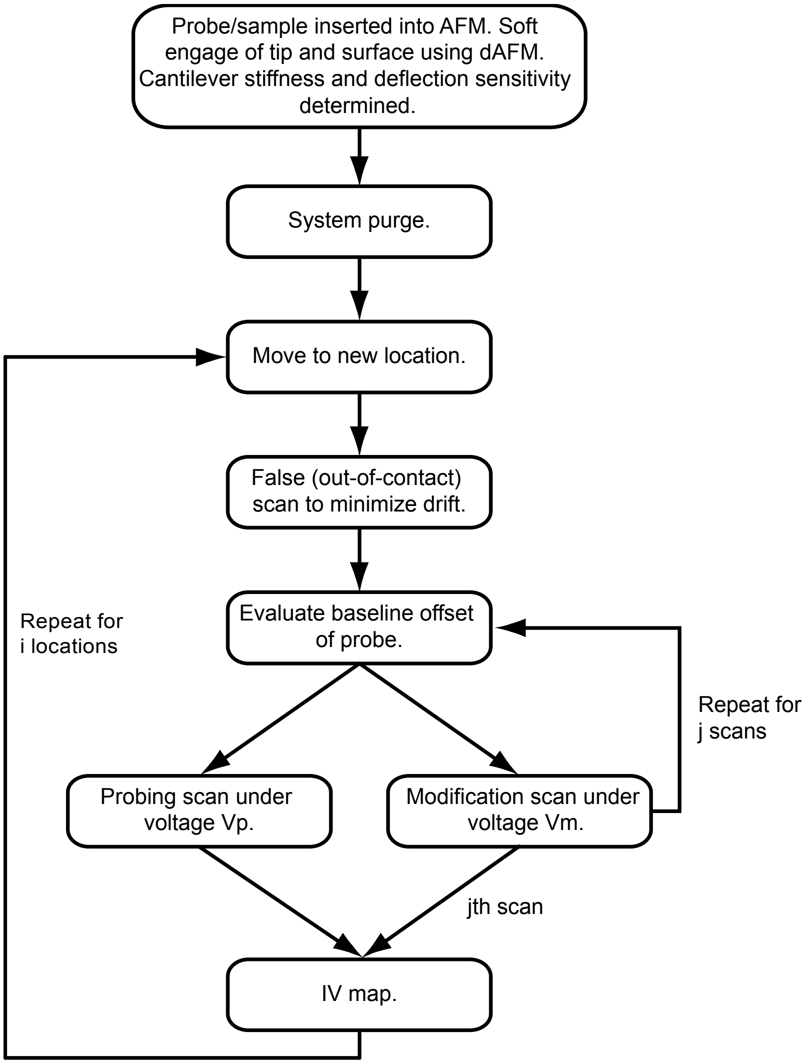

Figure 2.14: The AFM protocol used for evaluating changes to surface conductivity of N-UNCD and Pt exposed to load, shear, and electrical bias. Scans were performed at a new location for each probing scan and modification scan group. A total of i locations were scanned. Probing scans were performed before and after each modification scan to check electrical integrity of the probe tip. A total number of j modification scans are performed at each modification location.

Testing began with the insertion of the probe and sample into the AFM. The deflection sensitivity and the stiffness of the probe were initially overestimated to prevent unintended large loads from being applied during the engage process. A dAFM-based attractive-mode engage process, like that described in section 2.6.1 was then used to bring the tip and surface into contact without heavily cycling or disturbing the electrical integrity of the tip. The deflection sensitivity of the probe was fit from the slope of the in-contact portion of a lightly-loaded FvD measurement. The probe was then disengaged and thermal calibration (see section 2.1.4) was performed to determine the stiffness of the probe.

Scanning of the surface was then undertaken to evaluate the conductivity of the probe tip or to evaluate the response of the surface to prolonged exposure of load, shear, and electrical bias. The former is referred to here as a probing scan and the latter a modification scan. The probing scans were used to track probe tip conductivity at a new surface location to observe for loss of conductive tip material and to regenerate probe tip conductivity in the event that tribofilms resulting from modification scans adhered to the tip. The relative locations of probing and modification scans are shown in figure 2.15. A probing scan was performed before and to the left of every modification scan. A final probing scan was also performed to evaluate the final state of the tip. A gap of 1 μm was included between all scans so that any tribofilms or contaminants formed during scanning at one location would not affect evaluation at the next scan location.

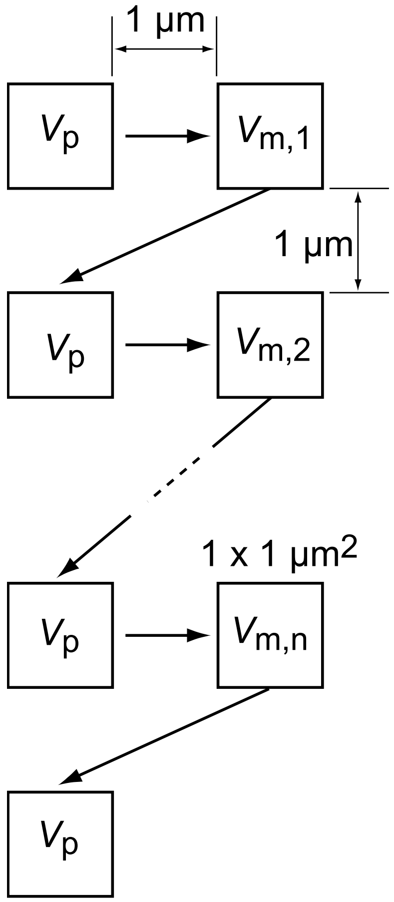

Figure 2.15: The relative location of probing and modification scans when testing the effect of load, shear, and electrical bias for Pt and N-UNCD contacts. A probing scan to evaluate the tip conductivity was performed before each group of modification scans. Scan locations are offset by 1 µm from one-another so that resultant tribofilms do not spread between test locations. The voltage during scanning is indicated at each location as the probing voltage, V_p, or the modification voltage at the ith test location, $V_{m,i}$. The tests terminated with a final probing scan.

The general process for both probing scans and modification scans involved four main components. The tip was first moved to a new, untouched location of the sample surface. A scan over the area of interest and for a duration of ~7 min. was then performed with the tip retracted several µm from the surface in order to reduce system drift at the new location. An FvD measurement was then performed to evaluate the baseline load offset from the out-of-contact portion of interaction. This ensured that the load applied to the tip-surface was not subject to deflection drift of cantilever and that quoted loads were within several percent of those intended. A single probing scan under probing voltage V_p or multiple scans under modification scan voltage V_m were then performed. V_p was selected to be just sufficient to yield statistically significant conductivity data on the probe state. The cantilever deflection offset was re-evaluated before each modification scan. An IV map was then taken inside the scan area after a probing scan or after a pre-determined number of contiguous modification scans to evaluate changes to the current-voltage response of the interface.

Both the probing scans and modification scans were performed over a 1 x 1 μm^2 area. The size of the area was chosen to be large enough to extract statistically-relevant conductivity data and to exceed drift of the MFP-3D AFM used for these studies (<100 nm per scan area) and yet small enough to ensure large electrical power density through the contact per unit scan time. The probing and modification scans were both performed at a rate of 0.2 Hz with 64 scan lines in the slow scan direction and 1024 points in the fast scan direction. All scans were performed at the same load for a specific probe, ranging from 25 – 50 nN depending on the particular test. Friction and conductivity in both the trace and retrace directions was collected with current amplification provided by the logarithmic amplifier described in section 2.2.

Two surfaces were interrogated under load, shear, and electrical bias using Pt-coated AFM probes. N-UNCD in the iPlas system at Argonne National Laboratory as described in section 2.5.2. Because of the age of the sample (several years), the sample was cleaned via sonication for 20 minutes each in acetone, methanol, and IPA. This was followed by drying using N_2 blowoff from a nitrogen dewar. A Pt surface similar to that tested in section 3.6 was also interrogated in an as-deposited state within several months of deposition and after storage in an N_2-purged dessicator. Contact mode probes of style PPP-CONT (Nanosensors, Neuchatel, Switzerland) and nominal stiffness of 0.2 nN/nm were coated with 70 – 85 nm of Pt using the Explorer14 sputterer. Deposition was performed on both the back and tip-side of the probes.

In order to study the effect of operating environment and electrical power on surface degradation of Pt/Pt and Pt/N-UNCD, tests were run in both laboratory air and under N_2 purging with V_m ranging from 0.25 to 8 V. In all cases, V_m was increased from $V_{m,1}$ to $V_{m,i}$, where i represents the total number of modification locations. A total of 7 and 12 contiguous modification scans at each location were used when investigating Pt/N-UNCD and Pt/Pt interfaces, respectively.

2.7.2 Interrogation of Chemical changes to N-UNCD

The contact resistance of Pt/N-UNCD interfaces exposed to low load, shear, and electrical bias was observed to increase. The method described in section 2.7.1 was modified to examine the surface chemistry of scanned regions using PEEM. The tip and back-side of AFM probes were coated with 45 – 55 nm Pt with the EMITech K575X sputter coater. Due to the geometry of the sample, scanning was performed in a Dimension 3100 AFM with current recorded using the extended TUNA module described in section 2.2. Five consecutive modification scans were performed in a single 4 x 4 μm^2 region while scanning for 512 lines and collecting 512 points per line for each scan with a scan rate of 0.2 Hz. After 5 modification scans, a probing scan was performed over an 8 x 8 μm^2 area encompassing the modification region so that changes in conductivity and friction due to tip-surface interaction could be compared between modified and unmodified surface regions. A new probe tip and surface location was used for each set of modification scans. Voltages ranging from 0 – 10 V and environments from <5% RH (N_2 purged) to 45% RH were investigated. Due to the low relative humidity of the laboratory at the time of testing, high RH was achieved by filtering N_2 through a humidifying chamber.

Fiducials were employed in order to find the modification scan locations during chemical measurements. Tantalum was deposited to a thickness of ~50 nm on the N-UNCD sample with a TEM grid serving as a shadow mask. Modification scans were then performed in the uncoated intersection points of the grid lines. The N-UNCD surface was cleaned by sonication for 20 min.

each in acetone, methanol, and IPA followed by drying with blowoff from an N_2 dewar both before and after Ta deposition. Focused ion beam milling (FEI Strata DB235 Focused Ion Beam) was used to label each scan location for easy discovery during PEEM.

CHAPTER 3: RESULTS AND DISCUSSION FOR THE GIGACYCLE TESTING OF PLATINUM/PLATINUM ELECTRICAL CONTACTS USING ATOMIC FORCE MICROSCOPY

3.1 Overview: Contact Cycling Experiments over Several Billion Cycles Using AFM

This chapter describes the results of cycling nanoscale electrical contact junctions for upwards of 2 billion contact cycles using AFM. This method was used to interrogate contacts as they would be employed in ohmic NEMS logic switches. The details of the extraction of conductivity and adhesion from force versus distance measurements are first described. It is then shown that contact resistance increased due to cycling and voltage between nanoscale Pt/Pt contacts. The next section extends these results to cycling under various tip-surface voltage conditions (with and without voltage applied during cycling) and environments (laboratory air and N_2). Finally, it is shown that shear between a probe tip and sample resulted in regeneration of the contact and that shear contact results in higher conductivity than contact normal to the the electrical interface.

3.2 Assessing the Conductivity of Single Asperity Contacts

Force versus distance (FvD) measurements were used to periodically evaluate the adhesion and conductivity of contacts cycled using AFM. Simultaneous collection of conductivity data, which will be referred to here as a current versus distance measurement (IvD), enables the observation tip-surface conductivity. Figure 3.1 shows a typical FvD/IvD measurement for a Pt-coated AFM probe in contact with a Pt counter surface from a protocol P2 cycling test as described in section 2.6.1.

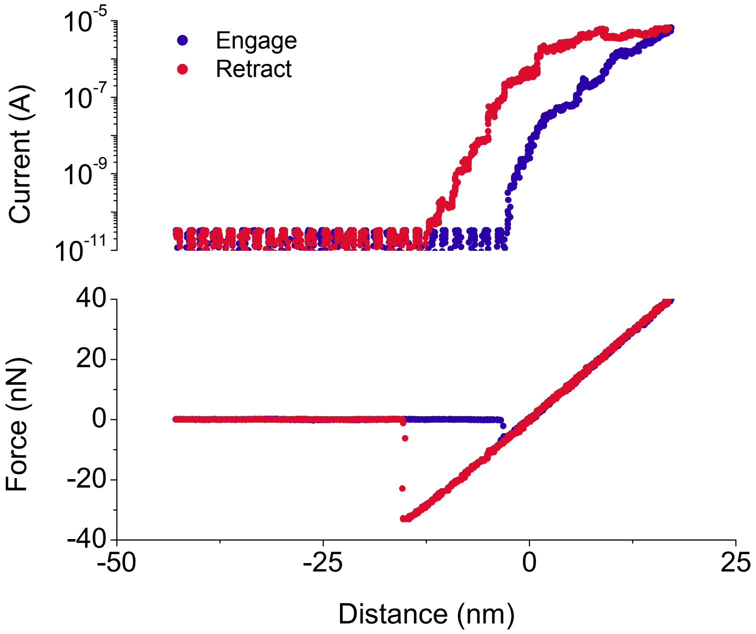

Figure 3.1: (Bottom) Force versus distance (FvD) and (top) current versus distance (IvD) measurements for a Pt-coated AFM probe on a Pt surface at a location of high conductivity. The probe was brought into (blue) and out of (red) contact with the surface and force (bottom) and current (top) were measured simultaneously. The snap-in and pulloff instabilities are both evident. The pulloff force (lowest force measurement) was used as measure of the adhesion of this Pt/Pt interface. These measurements were collected at an engage/retraction speed of 100 nm/s.

FvD/IvD measurements like that shown in figure 3.1 yield three quantities of importance in this work. The current at maximum load (40 nN in figure 3.1) is used to as one measure of the conductivity of the interface. The load of 40 nN for protocol P2 and 15 nN for protocol P1 were chosen because they fall within the range of contact forces expected for NEMS logic switches. Other measures of conductivity could have been selected such as the current response integrated over the load range or maximum conductivity during the loading curve (as opposed to conductivity at maximum load). However, NEMS logic switches generally operate under a fixed closure force (fixed actuation voltage). Therefore, conductivity at a fixed, or in this case, maximum load is the most reasonable parameter for the determination of contact resistance as it might be encountered in a real switch. In protocol P1 and protocol P2, 25 and 1146 FvD/IvD curves, respectively, were collected at periodic time points during cycling. The evaluation of contact resistance at many locations was chosen because Pt surfaces exposed to air in the tests presented here demonstrated significant variations in conductivity that spanned several orders of magnitude. Thus, a single measurement of conductivity at a fixed point is meaningless. The average and median value of conductivity data of each ensemble of data is reported at each cycling point. Using Ohm's Law, conductivity was converted to contact resistance. The pull off force, the minimum point of the FvD measurement, is used to report force of adhesion. Knowledge of the probe tip radius can then be used to determine the work of adhesion.

Conductivity and resistance extracted from the maximum load during FvD/IvD curves and contact mode C-AFM scans were observed to have distributions over a logarithmic domain. Figure 1.2 shows representative histograms of conductivity at maximum load for contacts cycled using protocol P2.

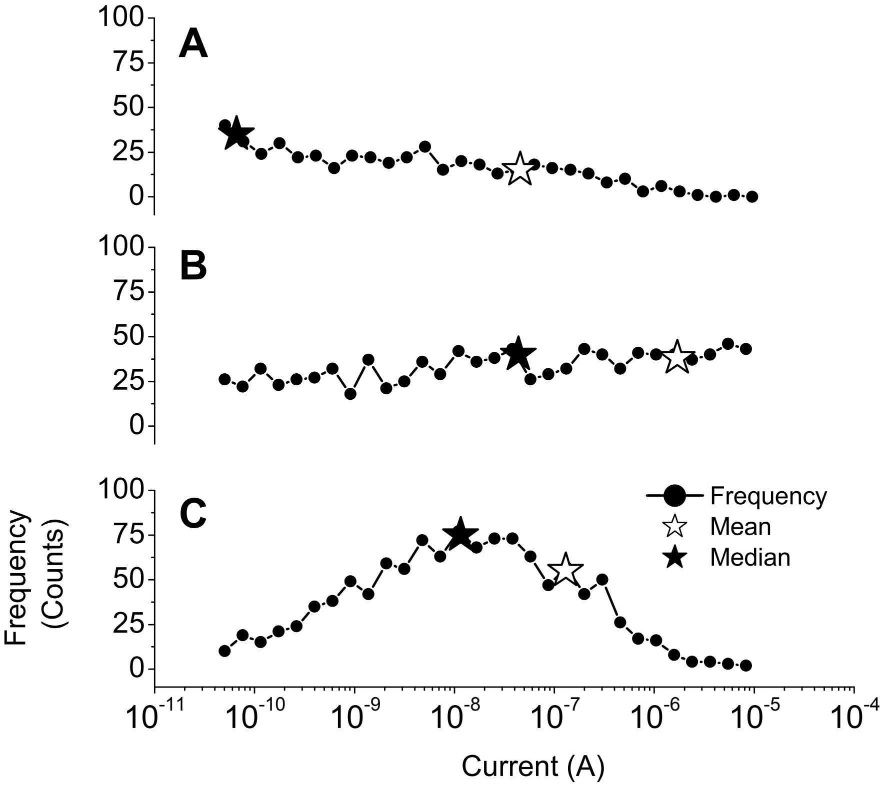

Figure 3.2: Various distributions of conductivity at maximum load observed during protocol P2 testing of contacts. Data skewed towards (A) low currents, (B) high currents, and (C) with a log-normal distribution have all been observed. In all cases, the mean and median of the data is often separated by several orders of magnitude. In (A), conductivity below the noise floor of the current amplifier (<40 pA) results in significant data with negative current values and leads to significant divergence between the mean and median values. All distribution shown here are composed of 1156 FvD/IvD measurements.

Figure 3.2 shows that current measured at maximum load at regularly-spaced points across a Pt surface demonstrates a remarkably large spread over a logarithmic range. Consequently, the mean and median of conductivity data represent two different figures of merit. Resistance calculations based on the mean conductivity of an ensemble of IvD measurements emphasizes low resistance values while the median more accurately represents the expectation value of all tested locations. Reliance on either the mean or the median has implications for the interpretation and context of the ensemble of data as shown in figure 3.3. Two electrical contact surfaces are shown. The first represents a simple model of a multiasperity contact indicative of MEMS-like switch contacts. In this example, *N* number of asperities all of radius *R* and corresponding to the number of IvD measurements performed, conduct in parallel. For a device of *N* contacting asperities, contributions to conductivity are dominated by the most conductive (*i.e*. the least resistive) elements. Thus, the mean represents the effective contact resistance of this electrical interface. Alternatively, *N* devices, each composed of a single asperity, which represents the fundamental contact unit of an interface, may also be tested. In this case, the expectation value for an ensemble of devices is more reliably represented by the median response. Thus, the average conductivity or resistance from an ensemble of IvD measurements is useful when comparing the measurements here to microscale, multiasperity work whereas the median is preferred when discussing device operation based on single asperity contacts. Both the mean and median will be reported in the following work with the first and third quartiles indicated for all median values.

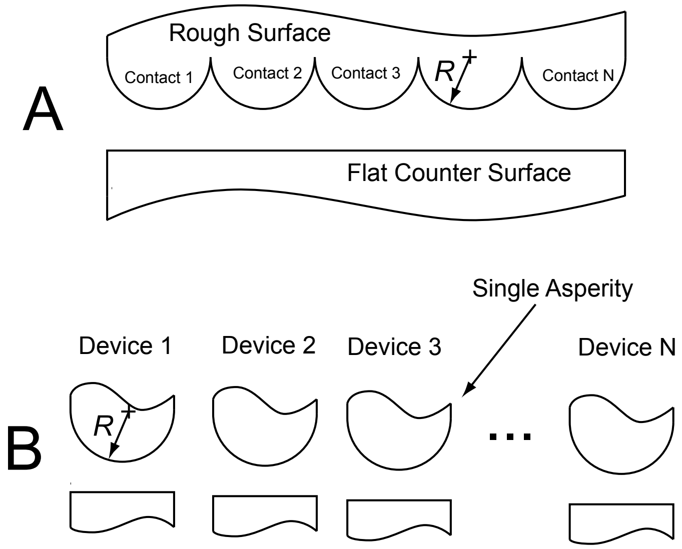

Figure 3.3: An ensemble of contacts in (A) a MEMS device with N parallel conducting contacts of radius R and (B) N number of NEMS devices with single asperity contacts of radius R.

3.3 The Effect of Voltage during Cycling on Single Asperity Platinum/Platinum Contact Lifetime

Prototypes of NEMS logic switches have been demonstrated with source-drain voltages ranging from several mV [19] up to several V [108]. Scaling analysis of NEMS logic switches has shown that the source-drain voltage will scale with the size of device – as NEMS logic switches become smaller and faster, lower operating voltages are necessary. In order to investigate the role of decreasing source-drain voltages on contact failure mechanisms and device robustness, single-to-several asperity Pt/Pt contacts were cycled using AFM for up to 2 billion interactions while applying a voltage (a modification voltage), V_m, of 100 mV to 2 V between Pt-coated AFM probes and a Pt substrate. Pt was selected as the test material because of its widespread use in existing mutiasperity, microscale switches and in prototype NEMS logic switches.

3.3.1 Contact Forces, Contact Stresses, and Contact Time during Cycling

Tests performed to investigate the effect of voltage on electrical contact lifetimes are labeled test series A and were undertaken using protocol P1 detailed in section 2.6.1. Contact cycling was split into two regimes. Early lifetime cycling (FvD cycling, $<10^6$ cycles) was undertaken using fast (~10 Hz) FvD curves with a maximum loading force of 15 nN. Late lifetime cycling (dAFM cycling, $>10^6$) was achieved using dAFM at the AFM probe resonance and large oscillation amplitudes (A_0>150 nm) in order to ensure tip-surface interaction during cycling. This resulted in peak forces of 80 – 128 nN for all interactions above 10^6 cycles. Table 3.1 identifies the voltages, tip radii, contact forces, and contact stresses during test series A.

Table 3.1: The modification bias, radii before and after cycling, and stresses during FvD and dAFM cycling for test series A. Peak normal stresses were calculated using DMT contact mechanics and the contact forces are compared in figure 3.4.

Test Identifier	**Modification voltage, V_m**	**Radius, before cycling (nm)**	**Radius, after cycling (nm)**	**Peak stress during FvD cycling (GPa)**	**Peak force during dAFM cycling (nN)**	**Peak stress during dAFM cycling (GPa)**
A1	100 mV	26 ± 5.7	31 ± 16	2.0 – 2.1	103 - 114	3.3 – 3.5
A2	100 mV	32 ± 12	28 ± 9.2	1.8 – 2.0	104 - 109	3.2 – 3.4
A3	500 mV	45 ± 25	41 ± 27	1.5 – 1.6	86 – 89	2.3 – 2.5
A4	1 V	21 ± 4.3	24 ± 4.9	2.2 - 2.4	108 - 112	3.8 – 4.2
A5	2 V	50 ± 20	21 ± 2.5	1.3 – 2.3	81 - 117	2.1 – 4.2
A6	2 V	31 ± 10	49 ± 14	1.5 - 2.0	93 - 128	2.3 – 3.4

The application of a voltage between the tip and sample during dAFM cycling leads to an additional electrostatic force that can be on the same order as van der Waals (vdw) interactions (see figure 2.5 for a comparison). Therefore, the peak forces and stresses during dAFM cycling quoted in table 3.1 were modeled using the method described in section 2.1.5 to account for variations in dAFM load due to V_m during cycling. The range of contacts times during dAFM cycling for tests A1 through A6 was found to be 262 – 333 ns from modeling. These ns interaction times, the high electrical time constant imposed by the low bandwidth of the logarithmic current amplifier, large contact resistances, and capacitances and inductances from the AFM voltage source can lead to a high electrical time constant, τ_e, and thus only a fraction of the current expected during slow tip-surface interaction [109]. To the limit of τ_e=0 and contact resistance, R_c, of 0, the charge distribution between the tip and sample will equilibrate immediately upon contact and is termed a non-persistent electrostatic interaction (NE) here. However, for τ_e=∞ or R_c =∞, the charge between the tip and surface will persist during contact and is referred to as persistent electrostatic interaction (PE). In order to bound the possible range of tip-surface force interactions, forces due to vdw-only (VDW), PE, and NE interactions were modeled using the method described in section 2.1.5. Figure 3.4 shows the peak forces and stresses at the beginning and end of dAFM cycling for all series A measurements.

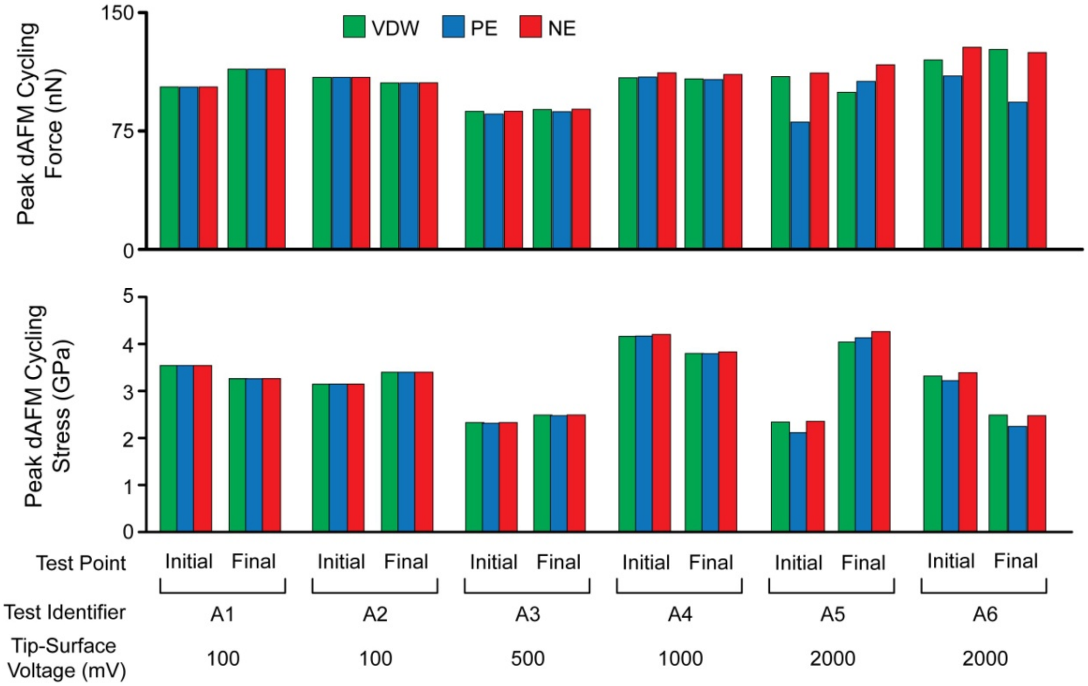

Figure 3.4: (Top) Peak force and (bottom) peak normal stress during dAFM cycling for measurements series A cycled using protocol P1. All calculations are based on average probe radii shown in table 3.1 and work of adhesion described in figure 3.11. Solutions for vdw-only (green), persistent electrostatic (blue), and non-persistent electrostatic (red) tip-surface interactions are shown for tip-surface conditions after 100 cycles (initial) and $2x10^9$+ cycles (final). These solutions assume E_t=E_s=130 GPa, v_t=vs=0.3, a_0=0.2 nm, A_r = 0.57. A_0 and K_{cant} as measured experimentally. Only tip-surface (modification) voltages above 1 V have a significant effect on the peak tip-surface interaction force.

Figure 3.4 shows that the electrostatic contribution to peak tip-surface interaction force is negligible below 1 V for the range of probe tip radii and dAFM cycling parameters investigated here. However, a 2 V potential between the tip and surface resulted in force variations of up to approximately 10%. The peak dAFM interaction forces and stresses quoted in table 3.1 are taken from the minimum and maximum of these values. The resulting peak tip-surface stresses were calculated from DMT contact mechanics and are within the range of 2.1 to 4.2 GPa for all dAFM cycling, which is below the hardness measured for thin Pt films in the work of Chen *et al*. [50]

(~5.3 GPa) and as measured by collaborators (5.2 – 5.5 GPa) for films deposited using the same sputterer and sputtering conditions as here. Furthermore, stresses during FvD and dAFM cycling were not significantly different for different V_m, suggesting that variations in contact stress do not account for differences in contact resistance changes that will be described later.

3.3.2 The Effect of Cycling on Resistance and Adhesion and the Initial Chemical State of the Contact Interface

Contact resistance during testing was observed to initially exceed theoretical predictions and increase as a function of cycling for all V_m. Figure 3.5 shows the average contact resistance and figure 3.6 shows the median conductivity as a function of the number of cycles for all series A tests. Figure 3.7 summarizes the magnitude of resistance increase from resistance measured after the first 100 cycles (R_i) and the resistance after approximately 2×10^9 cycles (R_f). The probing bias, V_p, during all FvD/IvD measurements was 50 mV and each data point represents the average (figure 3.5) or median (figure 3.6) of 25 regularly-spaced FvD/IvD measurements over a 1 x 1 μm^2 surface area. Two plots are shown for contact resistance and are delineated by low modification voltage ($V_m \leq 500$ mV) and high modification voltage ($V_m \geq 1$ V) for clarity.

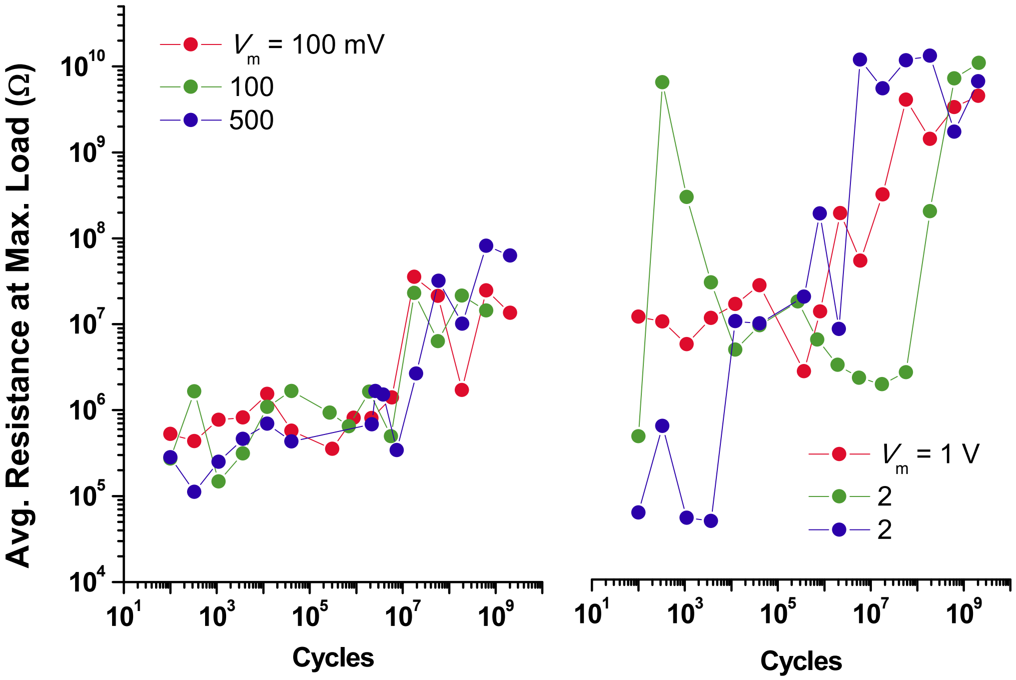

Figure 3.5: Average resistance at maximum FvD load as a function of number of tip-surface interaction cycles for data series A collected using protocol P1. Data for low modification voltage, V_m, is shown on the left and high V_m on the right. The vertical scales for the left and right plots are the same. Each data point represents the average of 25 regularly-spaced FvD/IvD measurements for a total of 350 measurements for each curve. Each data series was collected with a new Pt-coated probe tip at a new Pt surface location.

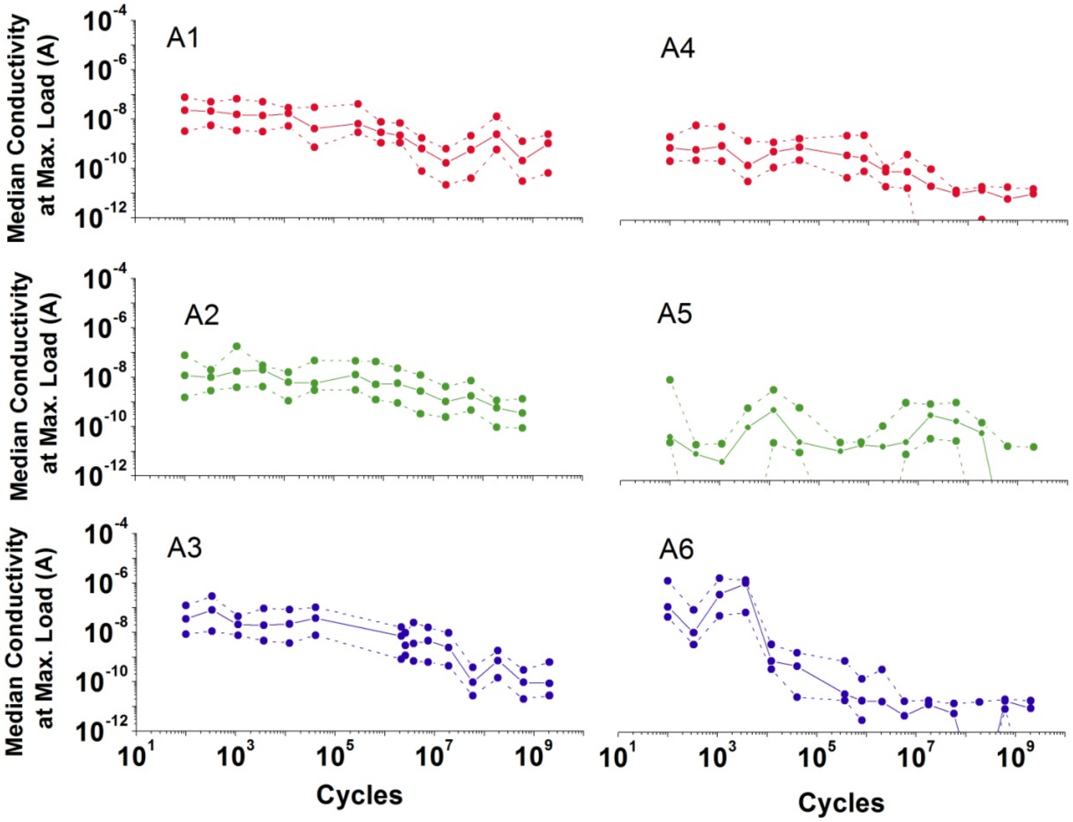

Figure 3.6: Mean, lower quartile, and upper quartile current at maximum FvD load as a function of number of tip-surface interaction cycles for data series A collected using protocol P1. All measurements have been separated into individual plots for clarity. Points below the y-axis range indicate negative currents that were below the noise floor of the logarithmic current amplifier.

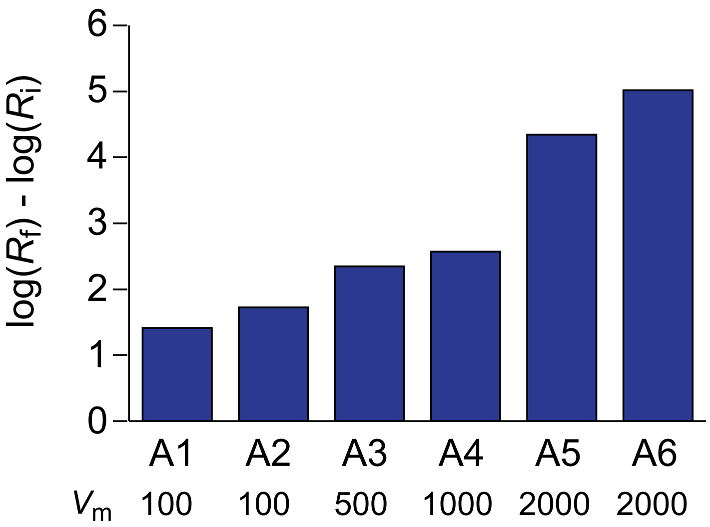

Figure 3.7: The magnitude of resistance increase as measured at maximum FvD load for data series A collected using protocol P1. The initial contact resistance, R_i, is taken from conductivity measured after 100 contact cycles and final contact resistance, R_f, from conductivity measured at the end of the test (~2x10^9 cycles).

Figures 3.5 – 3.7 show a significant increase in contact resistance (decrease in conductivity) as a consequence of cycling the contact. For low modification voltages ($V_m \leq 500$ mV), contact resistance increased 1.4 – 2.3 orders of magnitude over ~2x10^9 cycles. Cycling under high modification voltage ($V_m \geq 1$ V) resulted in larger resistance increases, 2.6 – 5 orders of magnitude, for the same number of cycles. These observations indicate that NEMS devices composed of nanoscale Pt/Pt interfaces will undergo less contact degradation as source-drain voltages decrease. The origin and details of these resistance increases will be discussed later.

The intial contact resistance of Pt/Pt interfaces investigated here significantly exceeds theory. For example, the constriction resistance for a clean Pt/Pt contacts under ballistic conduction [110] (electron mean free path, l_e, is less than the contact radius) with an effective contact radius of 20 nm ≤ R ≤ 100 nm and assuming l_e = 30 nm, resistivity of 105 nΩ-m, the mechanical and adhesive parameters of Pt measured in this work, and DMT contact mechanics is approximately 90 to 475 Ω. The average initial contact resistance measured here exceeds theoretical predictions by three to four orders of magnitude.

The high resistances observed at the beginning of testing were hypothesized to be the result of contaminant layers on the Pt surfaces contributing to an additional insulating film resistance. Adsorbed carbon and oxygen have been perviously observed on noble metals exposed to ambient and and inert atmosphers, including the Pt-Ir kilogram standard [111] and microscale Pt contacts [50]. In order to verify the chemical nature of the initial contact, X-ray photoelectron spectroscopy (XPS) was performed on a Pt film deposited using the same parameters and stored in similar conditions to that tested in cycling studies here. Figure 3.8 shows both carbon 1s and oxygen 1s edges measured in XPS for an as-deposited Pt substrate stored in an N_2-purged dessicator for 4 months and a Pt substrate cleaned with Pirahna within 10 minutes of insertion into the XPS vacuum chamber. Pirahna cleaning was performed in an attempt to aggresively remove any large-scale and adsorbed organic contaminants from the surface.

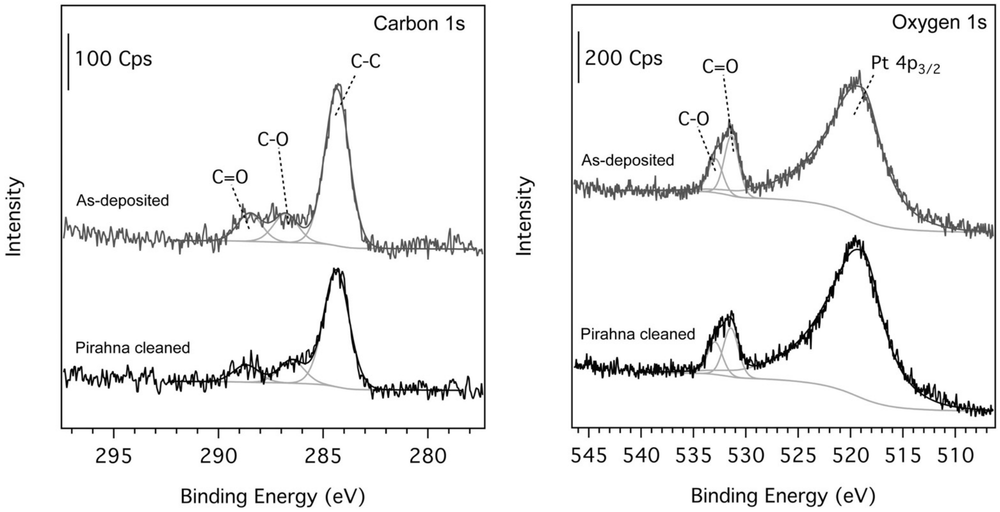

Figure 3.8: (Left) Carbon 1s and (right) oxygen 1s spectra of as deposited and Pirahna cleaned Pt surfaces obtained via XPS.

XPS showed similar magnitudes of adsorbed carbon and oxygen contamination on both the as-deposited and Pirahna cleaned samples. Survey scans revealed no significant concentrations of other contaminants and, as expected, Pt was also observed. Using the method described in section 2.4.1, the thickness of O and C contamination was estimated at 1.3 nm for for the as-deposited sample and 1.0 nm for the Pirahna cleaned sample. Under the assumption that Pirahna cleaning removes the majority of adsorbed organic contamination, these results show the re-adsorbtion of organic contaminants occurs within at least minutes. Enachescu *et al*. had previously shown at least an order of magnitude variation in conductivity between areas of clean Pt and Pt covered in C and O adsorbates using AFM in clean, ultra-high vacuum conditions [112]. Thus, the high resistances observed before contact cycling are attributed to adsorbed organic contamination of several nm-thickness that is likely present on both the tip and sample and is unavoidable with exposure of the samples to laboratory air.

The force of adhesion was measured simulataneously with conductivity, is shown in figure 3.9, and was found to span 2.0 to 12 nN for all tests. Significant variations or overarching trends in the force of adhesion were not observed with the exception of test A6 (V_m=2 V). The force of adhesion during test A6 decreased steadily during FvD cycling (10^2 – 10^6 cycles) and then returned to initial adhesion levels at the beginning of dAFM cycling (10^6 cycles). The origins of this change in adhesion will be discussed with reference to probe tip shape observed using TEM in the following section.

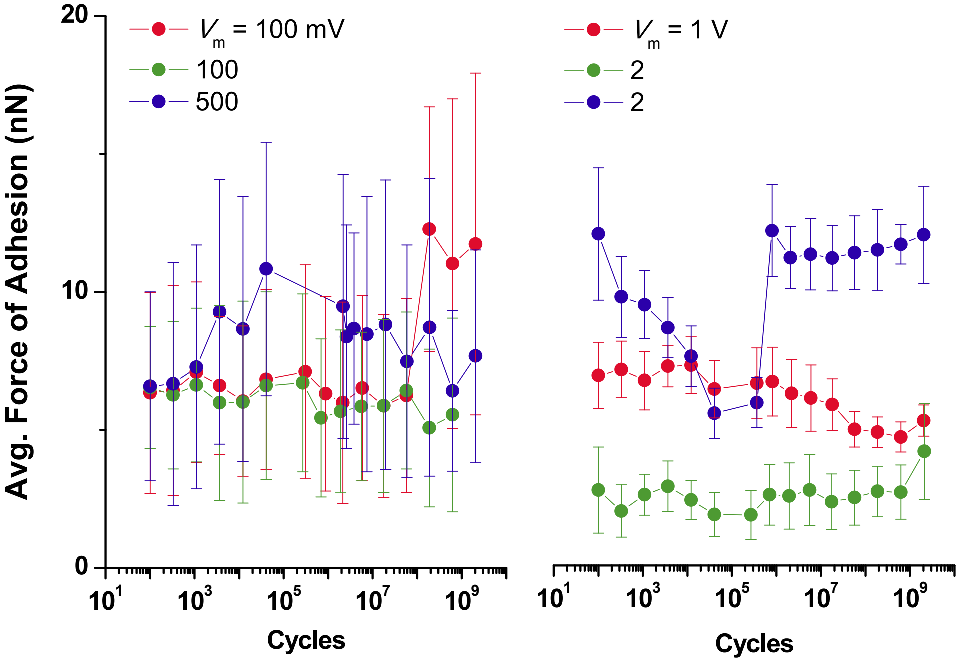

Figure 3.9: Average force of adhesion as a function of number of tip-surface interaction cycles for data series A collected using protocol P1. The error bars indicate the standard deviation of 25 measurements at each point for a total of 350 measurements for each curve. Significant variations in force of adhesion only occured for V_m≥1 V.

The adhesion values observed for all series A tests support the observation of adsorbed organic contamination on the electrical contacts. In order to decouple the geometry of the contact from the force of adhesion, the work of adhesion was extracted using eq. 2.12, which assumes DMT contact mechanics and uses the probe tip profiles measured using TEM (shown in section 3.3.3 and listed in table 3.1).

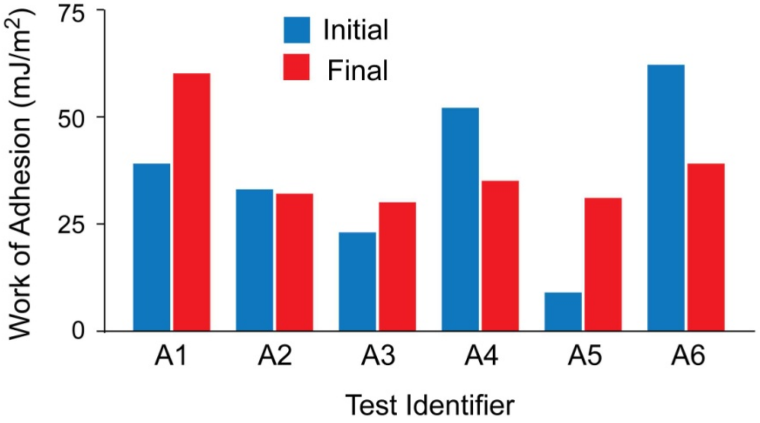

Figure 3.10: Work of adhesion after 100 cycles (initial) and ~2x10^9 cycles (final) for data series A collected using protocol P1. The probe tip radii used to extract the work of adhesion from the force of adhesion were calculated from TEM profiles before and after cycling and are listed in table 3.1.

The work of adhesion was found to vary between 9 and 62 mJ/m^2 for all tests. Experimental measurements of work of adhesion for typical metals are in the range of 400 to 2200 mJ/m^2 [113, p. 205]. Thus, the work of adhesion here is up to two orders of magnitude smaller than expected for metals and only slightly larger than expected for carbon, oxygen, and hydroxyl group-containing compounds [113, p. 204]. It is worthwhile to note that the work of adhesion shown in figure 3.10 assumes an ideally flat substrate. However, the Pt counter surface possesses roughness that can affect the contact area during adhesive pulloff. However, even if estimates of effective radius of the contact (which would include surface roughness) were overstated by one order of magnitude, the maximum calculated work of adhesion measured here would just begin to approach that of the least adhesive metals. Taken together, the work of adhesion, XPS, and resistance measurements indicate that the contact stresses investigated during cycling and probing were not sufficient to establish direct Pt-to-Pt contact through adsorbed O and C contamination.

3.3.3 Probe Tip Profiles Before and After Cycling and Evidence of Tribopolymer Formation

To further understand contact resistance degradation shown in figure 3.5 and changes to adhesion shown in figure 3.9, profiles of the probe were acquired with TEM both before and after cycling and are shown in figure 3.11.

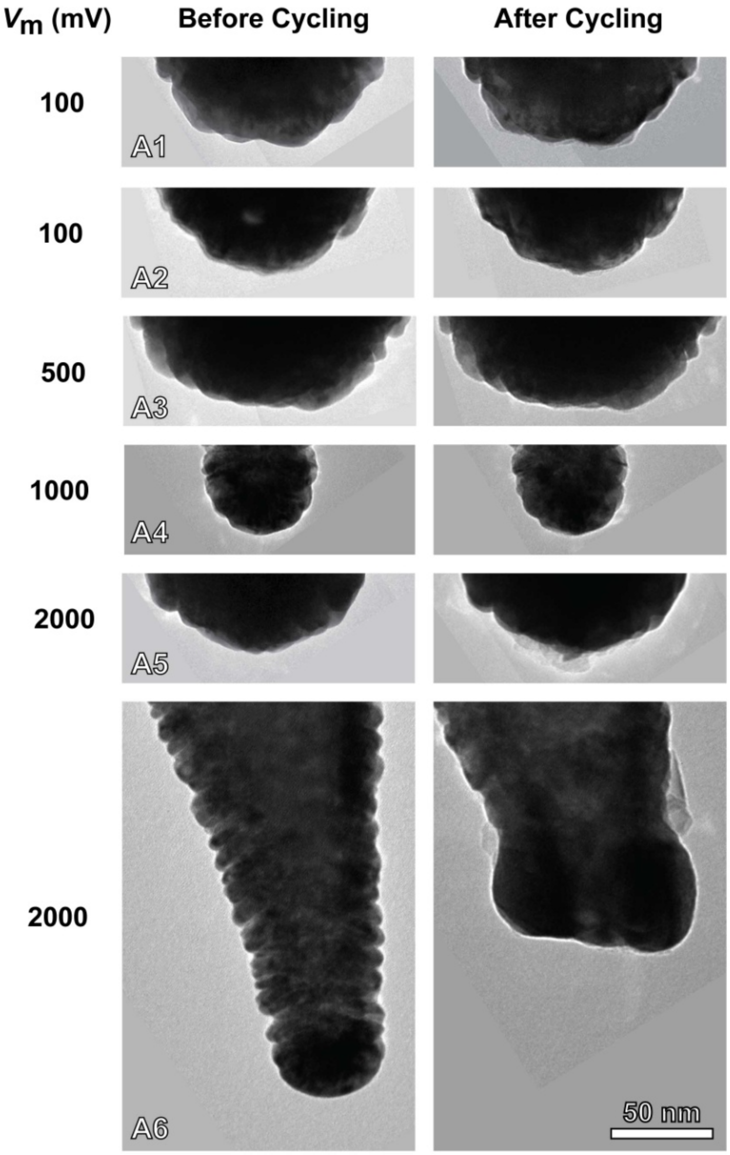

Figure 3.11: Probe tip profiles obtained by TEM for measurement series A cycled with protocol P1. (Left) Before and (right) after cycling for ~2x10^9 cycles. The tip-surface voltage during cycling (probing voltage) is listed on the left. All scale bars are the same. Gross changes to tip shape were only observed for A5 and A6 (V_m = 2 V).

TEM profiles show that gross changes to the probe tip shape only occurred in the case of V_m=2 V (A5 and A6). A6 demonstrated erosion of Pt more than 60 nm into the Pt tip shank whereas A5 demonstrated redistribution or the addition of material at the very tip. Despite these tip shape changes, the resistance data and high tip contrast in TEM suggest overall retention of the Pt coating for all probes, including A5 and A6.

Of note was a lack of tip wear in the absence of high electrical power. Vahdat *et al*., using a similar dAFM contact cycling technique, observed significant wear in brittle material systems at stresses exceeding material hardness (8 – 50 GPa) and over similar cycling periods [114]. Wear has been shown to positively correlate with interaction stress in these systems [115]. However, the interaction stresses encountered in the tests here were below the hardness of Pt and considered representative of contact asperities in NEMS logic switch interfaces. This suggests that wear, erosion, or gross deformation of the contact interface will not be a significant failure mechanism for Pt/Pt NEMS logic contacts operating at low voltages and moderate contact stresses.

Observation of the probe tip shape in conjunction with chemical and adhesion data permit interpretation of the resistance increases seen during cycling. The force of adhesion (with the one exception of test A6) and the probe tip radii before and after testing suggest little variation in the geometry of the contact as a result of cycling. Contact resistance depends inversely on the radius of contact. Thus, in the absence of changes to the probe tip radius (contact area) contact resistance would be expected to remain constant, which contradicts contact resistance increases seen as a result of cycling. This discordance was addressed through higher resolution TEM imaging of the probe tip profiles. Figure 3.12 shows high resolution TEM images of the probe from test A1 before and after cycling.

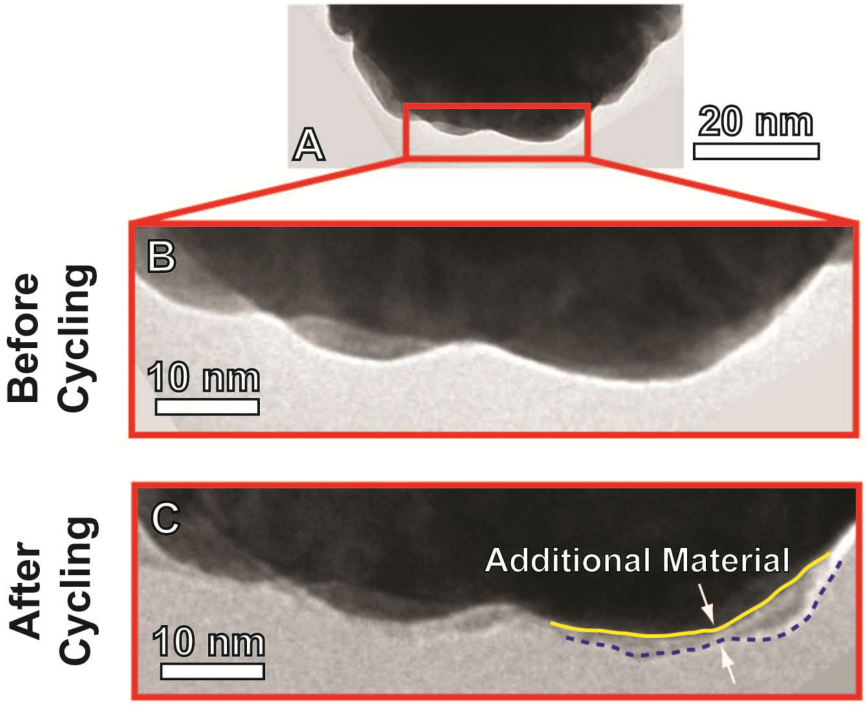

Figure 3.12: (A) Probe tip profile from series A measurement A1. High resolution image of the contact point (B) and (C) after cycling for $2\text{x}10^9$ cycles with V_m=100 mV. Additional low density material appeared in the contact zone. The edge of the original tip profile and the added material are indicated by a yellow and blue dashed line, respectively, in (C).

High resolution TEM images of all series A probes unambiguously show the formation of additional, low density product on the probe tip of up to 5 nm in thickness. This material appears to form both at the direct zone of contact and up to several to tens of nm away from the point of tip-surface interaction. This material will be referred to as tribopolymer (TP) in this work. In accordance with the findings of Hermance and Egan [105], Chen *et al*. [50], and Czaplewski *et al*. [49], this material is believed to be composed of short-chain hydrocarbons that result from mechanochemical interactions during electrical contact interaction. The present, limited understanding of the TP growth mechanism suggests that stress, electrical power, and sources of contamination and adsorbed material in the surrounding environment lead to growth of an insulating film on the contact surface composed C, H, and O species [50]. Electron energy loss spectroscopy (EELS) using TEM was unsuccessfully attempted to determine the chemical composition of these low density films. In particular, the highly focused electron beam required for EELS was found to remove the product and interpretation of the aerial density of chemical species was complicated by the conical AFM tip profile.

Resistance increases due to the formation of insulating species on the tip and, potentially on the counter surface, are supported by the fundamental physics of conduction across a physical gap. Tunneling current through an insulating film has an exponential relation to insulator thickness for many material systems. Thus, each additional thickness unit of TP would be expected to yield an exponentially related unit of contact resistance increase. Two assumptions could be posed for the rate of TP growth at the contact. TP growth could be linearly related to the number of contact cycles if it occurs directly at the interface. However, if TP formation is assisted by catalytic activity and stress at the Pt/TP interface, the growth rate would likely be logarithmic (self-limiting) due to the need for environmental contaminants to penetrate the existing TP film [111]. In either case, variations in contact resistance due to cycling would occur over logarithmic scales like that observed in the single asperity Pt/Pt cycling tests presented here.

While all series A cycling tests demonstrated a progressive increase in resistance during some portion of the test, the V_m=2 V tests (A5 and A6) demonstrated abrupt changes in resistance or adhesion and geometric changes to the tip shape. The origin of these changes are presumed to be tip melting due to joule heating. This observation is not surprising since Lo & Bain [83] have observed melting of Pt-coated AFM probes of similar tip radii at voltages below 1 V. Calculation of the contact supertemperture due to Joule heating using the method employed by Brand *et al*. [52] revealed potential temperature increases ranging from 10 ˚C for tip-surface voltages of 100 mV up to ~5000 ˚C for tip-surface voltages of 2 V at the lowest measured resistances during FvD/IvD measurements.

For the case of A6, resistance and adhesion data indicates dramatic changes in the state of the contact within the first 100 contact cycles and at the transition to dAFM cycling (10^6 cycles). Average contact resistance for test A6 was the lowest for all series A measurements, which was unexpected as the initial tip radius was similar to all other A series tests and the initial chemical state (adsorbed C and O) expected to be similar. Additionally, high adhesion after the first 100 cycles was similar to the final adhesive interaction. This suggests that the contact evolved to a smaller, less contaminated, but more adhesive contact radius that expressed metal-like adhesion and conductivity after only 100 contact cycles. This is supported by observations from Schimkat [116] and Andzane *et al*. [117] that heat generation at the contact due to high voltages and current can evaporate contaminants and that the contact area changes due to joule heating will evolve to a smaller equilibrium size [118]. Further FvD cycling of the probe (10^2-10^6 cycles) led to a decrease in adhesion that is consistent with reformation of tip-surface contaminants and is supported by simultaneous observation of increased contact resistance over the same cycling period. The transition to dAFM cycling (10^6 cycles) resulted in an increased peak interaction force from 15 to 93 – 128 nN. Thus, the significant increase in adhesion and decrease in resistance at 10^6 cycles indicates contact broadening and further TP formation. While the contact force is higher during dAFM cycling, gross changes to the tip shape due to Joule heating are less expected due to the low electrical time constant imposed by the current amplifier and fast cycling speeds. These results indicate that the ablation of the contact occurred within the first 100 contact cycles, exposed a more conductive interface, and was followed by re-contamination of the contact interface. Increased forces during late lifetime cycling (10^6+ cycles) then led to broadening of this new tip geometry.

3.4 The Effect of Environment and Voltage on Platinum/Platinum Contact Lifetime

In section 3.3 (test series A), the role of voltage between the contacts on nanoscale Pt/Pt contact degradation in N_2-purged, low humidity environments was investigated as it might be encountered in packaged devices. However, hermetic sealing of devices would contribute to higher device manufacturing costs [49]. Thus, it is desirable to understand the long-life performance of these contact in other atmospheres, including air. With this motivation, contact cycling was performed in both N_2 environments and laboratory air.

The tests performed in this section are referred to as test series B through E, and were undertaken using protocol P2 described in section 2.6.1. In these tests, the number of FvD/IvD measurements during each tip-surface adhesion and conductivity evaluation was increased to 1156 (compared to 25 for protocol P1 tests) in order to improve statistical representation of the data. In order to increase tip-surface interaction during conductivity interrogation, and based on the observation in section 3.3 that 80 nN+ loads did not lead to significant wear of the probe tip, the loading force during FvD/IvD measurements was also increased from 15 nN used in section 3.3 to 40 nN. Because the increased number of FvD/IvD measurements required significant testing time, initial FvD cycling was omitted for these tests to enable test completion in reasonable timeframes (10-16 hours). Heavily-scaled NEMS logic devices will likely demonstrate source-drain voltages of just several mV [19]. In order to probe the failure mechanisms below the point of probe melting observed in section 3.3 (at 2 V) and the effect of low voltage during cycling, mechanical cycling ($V_m = 0$ V) and hot cycling at 1 V were interrogated.

Several additional improvements were instituted for data collection in measurement series B through E. In order to improve collection of conductivity data during IvD curves, the probing bias was increased from 50 mV used in section 3.3 to 200 mV here. Observation of negligible differences in 100 mV to 500 mV cycling tests in section 4.3 suggest that this probing voltage increase will not adversely affect the results. A_r was decreased from 0.57 (the point of peak interaction force) to 0.25 in order to ensure tip-surface interaction deep into the repulsive tip-surface interaction regime during every cycle. TEM images of the probe tip profile were not acquired before testing. Therefore, in order to determine repulsive tip-surface force interactions, AvD measurements were performed before testing to experimentally determine the minimum dAFM amplitude required for repulsive tip-surface interaction (phase < 90˚). This amplitude was then increased by 150% during cycling to ensure repulsive tip-surface interaction even under changes to the tip-surface interaction during cycling (for instance, due to probe tip geometry changes). Finally, the surface of the contact was scanned under ~15 nN load before cycling as described in section 2.6.1, in order to remove adsorbed contaminants.

3.4.1 Peak Contact Forces, Peak Contact Stresses, and Contact Time during Cycling

Four independent test series consisting at least three repeated test were conducted for the four combinations of environment (N_2 purged vs. laboratory air) and cycling type (mechanical cycling – V_m = 0 V vs. hot cycling - V_m = 1 V). Table 3.2 lists the environment, cycling type, peak dAFM cycling forces, and peak dAFM cycling stresses for these tests. Peak forces and stresses during cycling are plotted in figure 3.13.

Table 3.2: The test identifier name, environment during testing, tip-surface voltage during cycling, final radius, and peak forces and stresses during dAFM cycling for measurement series B through E cycled using protocol P2. Peak normal stresses are calculated using DMT contact mechanics and force ranges are taken from the results plotted in figure 3.13.

Test Identifier	**Environment**	**Modification Bias, V_m**	**Probe radius after cycling (nm)**	**Peak force during dAFM cycling (nN)**	**Peak stress during dAFM cycling (GPa)**
B1	Low humidity, N2 purged, <4% RH	0 V, mechanical cycling	24 +/- 1.8	117	3.9
B2			26 +/- 4.4	181	4.3
B3			38 +/- 17	209	3.5
C1	Laboratory air (13 – 21 % RH)		46 +/- 9.5	155	2.8
C2			39 +/- 19	205	3.4
C3			57 +/- 18	390	3.3
D1	Low humidity, N2 purged, <4% RH	1 V, hot switching	30 +/- 4.6	150 – 157	3.7
D2			127 +/- 33	106 - 153	1.2 – 1.4
D3			41 +/- 9.2	206 - 216	3.3 – 3.4
D4			44 +/- 6.6	242 – 254	3.3 – 3.4
E1	Laboratory air (17 – 33 % RH)		73 +/- 21	114 – 137	1.8 – 2.0
E2			29 +/- 2.3	238 - 244	4.4
E3			39 +/- 2.2	208 - 216	3.4 – 3.5

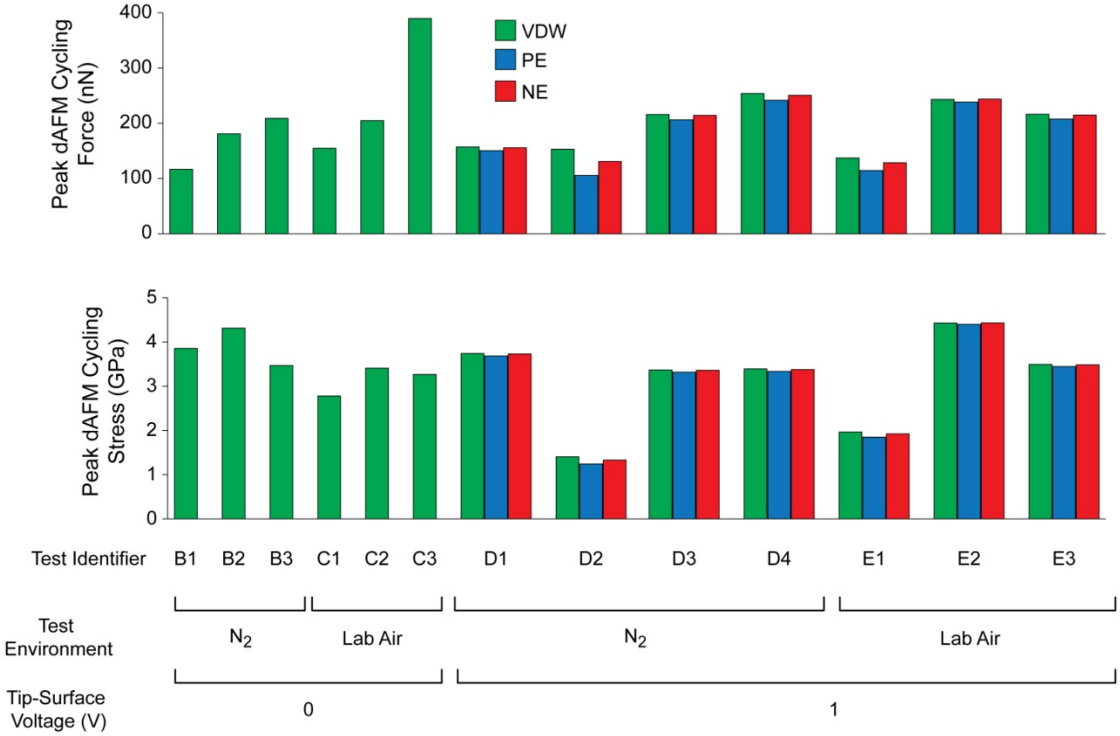

Figure 3.13: (Top) Peak force and (bottom) peak normal stress at the end of dAFM cycling for measurements series B through E cycled using protocol P2. All calculations are based on average probe radii shown in table 3.2 and work of adhesion shown in figure 3.19. Solutions for vdw-only (green), persistent electrostatic (blue), and non-persistent electrostatic (red) tip-surface interactions are shown. Electrostatic solutions are not shown for tests performed under mechanical cycling. These solutions assume E_t=E_s=130 GPa, v_t=vs=0.3, a_0=0.2 nm, A_r = 0.25. K_{cant} was measured experimentally via thermal calibration.

The dAFM cycling forces and stresses for the B through E series measurements span 114 - 390 nN and 1.2 – 4.4 GPa, respectively. Like test series A, all stresses during testing were below the hardness of Pt. Furthermore, tip-surface voltages of 1 V were observed to have little effect on tip-surface stresses and forces. Contact time during all cycling was similar to that of series A tests.

3.4.2 The Effect of Environment and Voltage on Resistance and Adhesion during Nanoscale Platinum/Platinum Contact Cycling

As in the series A tests, the series B through E tests showed a general increase in average contact resistance due to cycling. Figure 3.14 shows average contact resistance as a function cycling and figure 3.15 summarizes the magnitude of contact resistance change from the first 10^6 to ~10^9 cycles for all tests. Results are separated by testing environment and voltage during cycling.

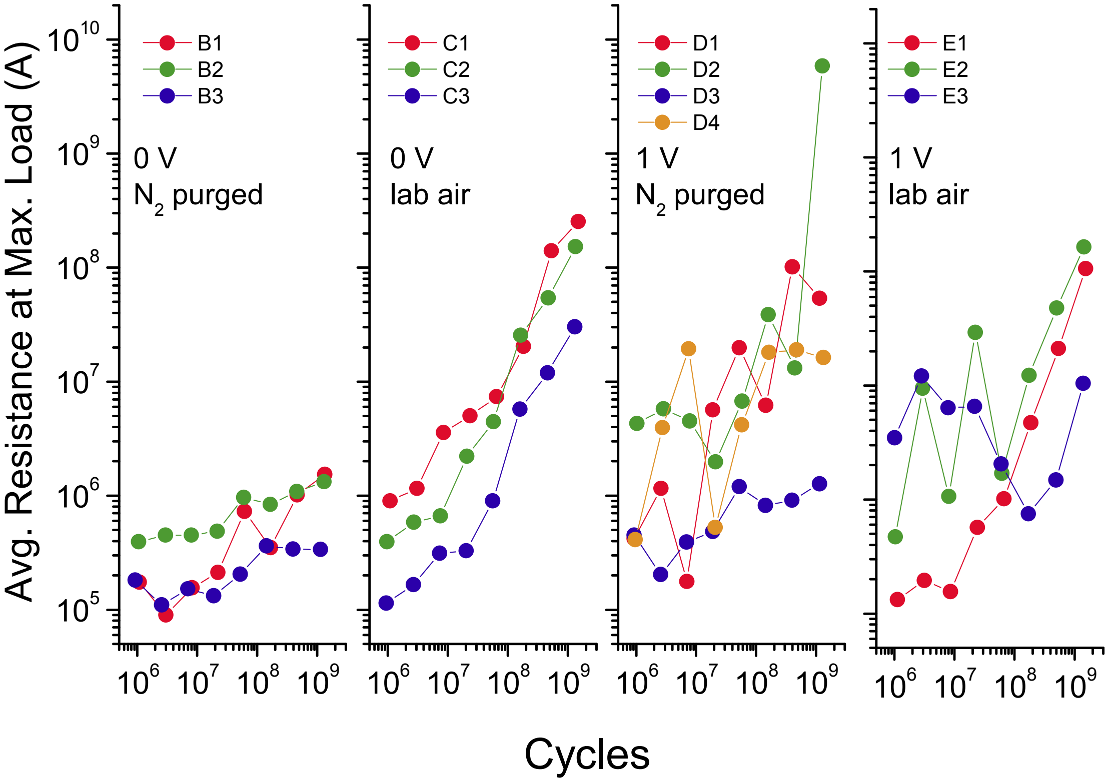

Figure 3.14: Average resistance measured from probing FvDs at maximum load (40 nN) for cycling in various environments (N_2 purged and laboratory air) and voltage between tip and sample (0 V, mechanical cycling, and 1 V, hot switching). Each data point represents the average of 1156 regularly-spaced FvD measurements collected over a 1 x 1 μm^2 surface region. The tip-surface probing voltage, V_p, for all measurements was 200 mV. Each curve represents a new probe at a new Pt surface location.

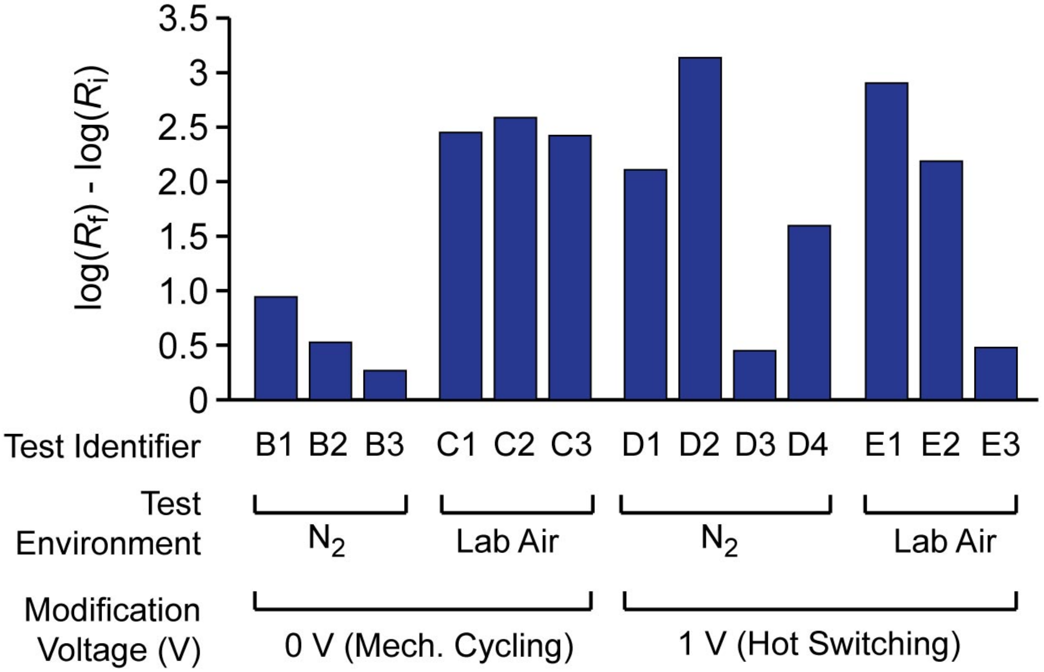

Figure 3.15: The magnitude of resistance increase as measured at maximum FvD load for data series B through E collected using protocol P2. Initial contact resistance, R_i, is taken from conductivity measured after ~10^5 contact cycles and final contact resistance, R_f, from conductivity measured at the end of the test (~$1x10^9$ cycles).

Repeated testing of Pt/Pt contacts under different environmental and voltage conditions revealed several patterns. Contact resistance increases were consistently the lowest under mechanical cycling in an N_2-purged environment. However, similar testing in laboratory air, which includes oxygen, water vapor, and environmental contaminants, consistently resulted in the largest increases. Hot switching at 1 V in both N_2 and laboratory air yielded highly fluctuating resistance behavior. The origins of this degradation will now be discussed.

Testing of metals (including Pt) in clean, high vacuum chambers and controlled addition of organic compound has shown dramatic effects on TP formation for organic contaminant concentrations as low as 50 ppm [105]. Interestingly, the increased degradation seen for mechanical cycling in N_2 and air suggests there is significant variability when organic environmental contaminants are varied over much larger ranges. For instance, cycling in a N_2-purged environment like that of series B cycling and assuming 1 – 4% RH at standard temperature and pressure results in around 100 ppm of water vapor. However, increasing the relative humidity to 20% RH, as was the case for C series cycling, results in around 900 ppm of water vapor. Clearly, the increased water content in the surrounding environment or additional contaminants had a profound effect on nanoscale Pt/Pt contact degradation. This implies that operation in inert environments and limiting environmental contaminants can have a large impact on Pt/Pt electrical degradation, an observation that has been reported for Au/Pt microscale electrical contact testing [49].

Like in test series A, larger contact resistance increases were periodically observed under hot cycling conditions. However many hot cycling tests (C3, C4, D2, and D3) exhibited periods of increasing conductivity. Recent observations for microscale Pt/Pt contacts have suggested that the application of an electric fields across TP films can result in dielectric breakdown of the film, rendering it less resistive [52]. Such behavior may have occurred in the present tests. In addition, the application the presence of electrical power may have lead to Joule heating of the interface that resulted in thermal breakdown of the TP. Alternatively, stresses at the contact may displace the insulating film during cycling. However, no repeatable correlations were observed between stress and contact resistance increases in these tests. Furthermore, series C measurements showed large resistance degradation and no contact resistance decreases, yet only differed from hot cycling tests in that no voltage was applied during cycling. These observations suggest that breakdown or thermal degradation of insulating TP as the more likely explanation for the variations seen during hot cycling tests.

The large number of FvD/IvD measurements performed during series B through E testing (1156 during each evaluation) permit visualization of the conductivity statistics and reveal details not seen in the average resistance plot (figure 3.14). Conductivity histograms were extracted from conductivity measured at maximum load during each set of FvD/IvD measurements. These histograms were collapsed into a three dimensional representation of conductivity changes for each cycling test, which we call heat maps. The heat maps were generated as described in figure 3.16. Heat maps for series B through E tests are shown in figure 3.17.

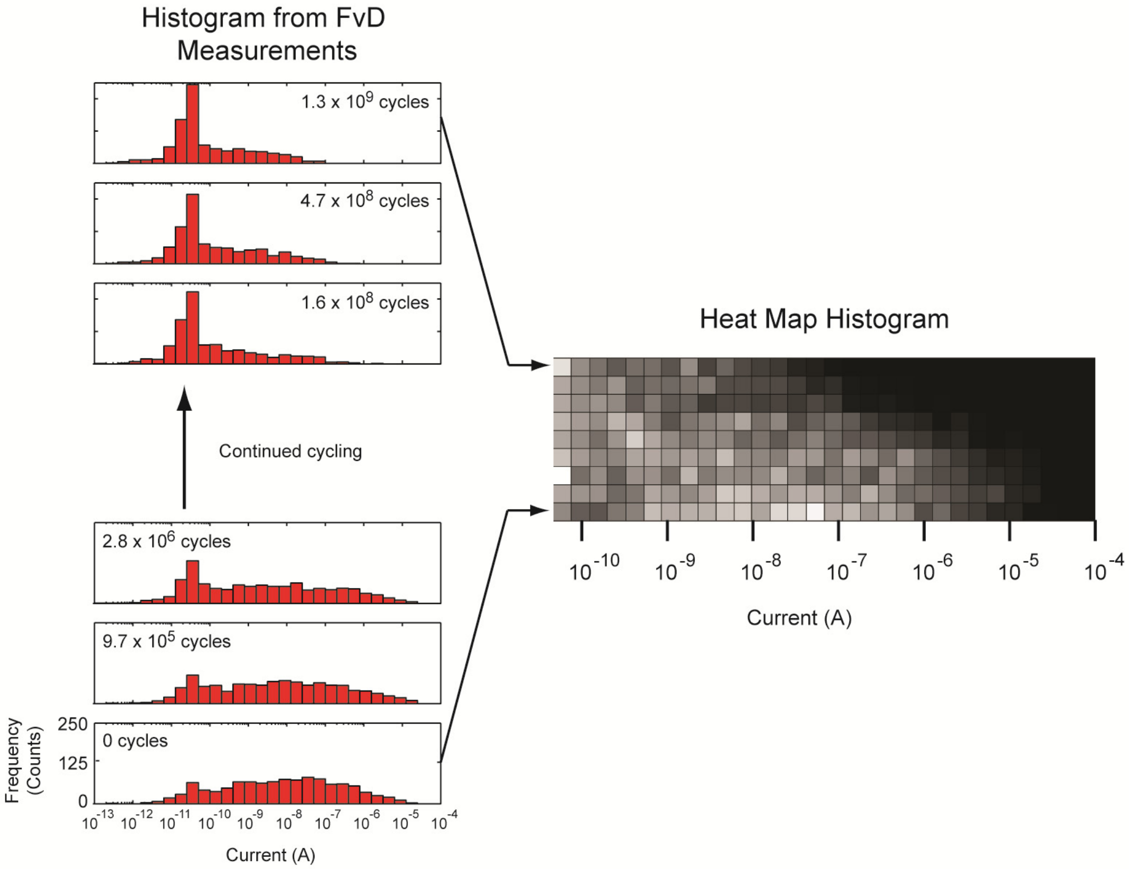

Figure 3.16: Relationship between conductivity histograms (left) and heat map histograms (right). (Left) Histograms with a logarithmic conductivity ranges were constructed from conductivity measured at maximum load during engage (40 nN) for FvD/IvD probing measurements before cycling and at various time points during cycling. The bottom histogram represents the distribution of surface conductivity measured before cycling while the top histogram represents the distribution after 1.3 billion contact cycles. (Right) Heat maps represent histogram distributions as a function of the number of tip-surface interactions. Each horizontal row of the heat map represents a single conductivity distribution with the color representing the frequency of points within each bin range. The bottom row represents the distribution before cycling and the top row represents the distribution after test completion (~1.3 billion cycles). The lowest current

represented on the heat map is 40 pA, which corresponds to the noise floor of the logarithmic current amplifier.

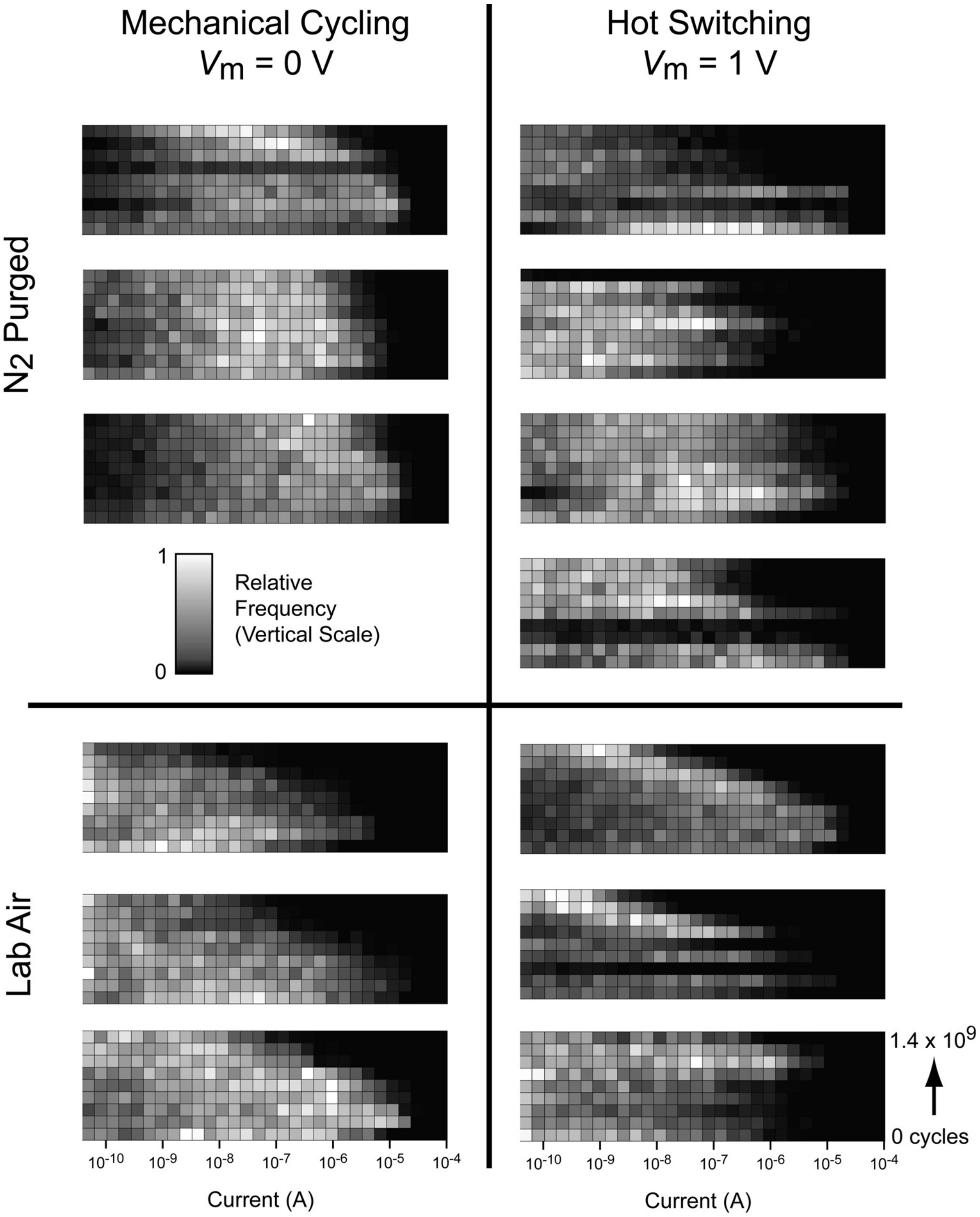

Figure 3.17 Histogram heat maps for measurement series B through E cycled using protocol P2. Current is taken from conductivity measured at maximum FvD/IvD load of 40 nN. The heat maps show a recession of the current front with continued cycling that reflects resistance increases observed during cycling. A shift in conductivity from lower to higher currents from the first to second row (0 cycles to ~10^5 cycles) demonstrates a cleaning of the contact or evolution of the interface geometry due to cycling.

While the heat map histograms reveal the same general trends for conductivity as average resistance shown in figure 3.14, the inclusion of pre-testing conductivity information consistently reveals a decrease in contact resistance after the first ~10^5 cycles (with some fluctuations in this overall trend). Contact degradation in these maps is revealed through recession of the conductive front and is observed in all tests at the final number of cycles. However, in most cases, an increase in conductivity was observed from 0 to ~10^5 cycles. This phenomenon would indicate either cleaning of the contact through removal of initial contamination, or broadening of the contact area due to enlargement of the tip. Test series A, which was conducted under similar contact stresses, revealed no gross changes to the tip for conditions corresponding to V_m used in test series B and D shown here. Therefore, this initial contact regeneration effect is attributed to either nanoscale variations in tip geometry that were not observable in TEM or a cleaning of the contact. The latter is supported by run-in that has been observed in microscale tests of electrical contact materials [59].

As in test series A, adhesion was simultaneously tracked during cycling for all series B through E tests. Figure 3.18 shows the average force of adhesion as a function of contact cycles.

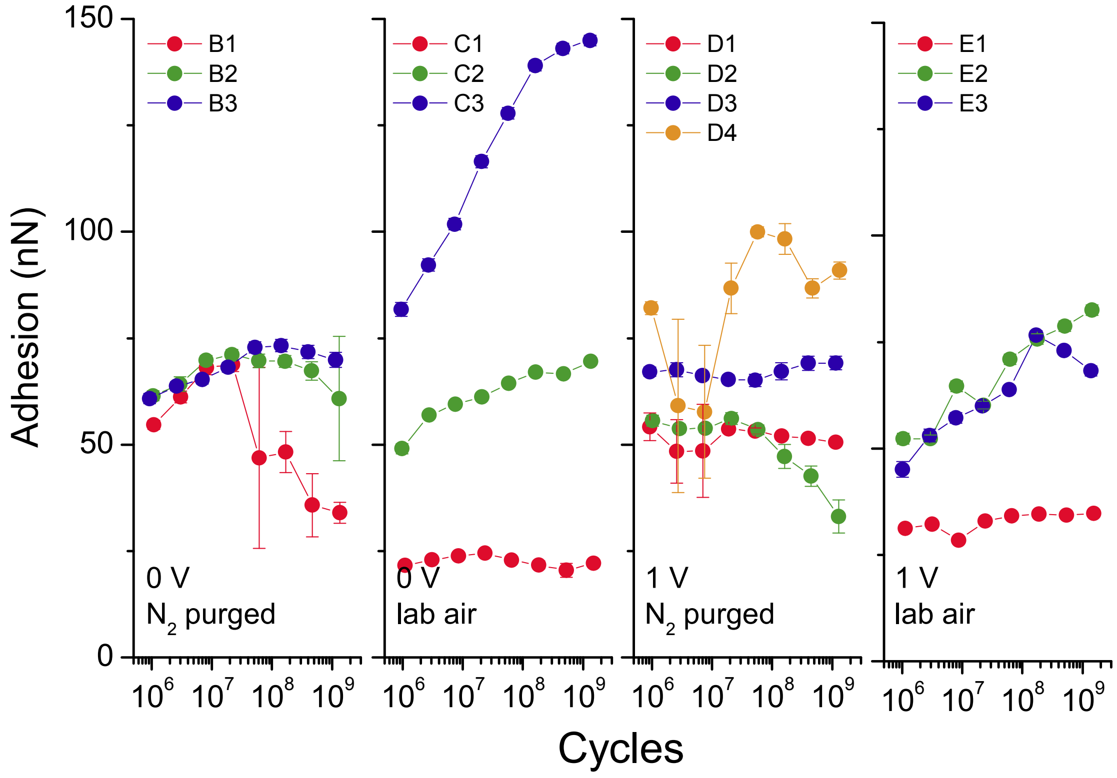

Figure 3.18: Average force of adhesion for cycling in various environments (N_2 purged and laboratory air) and voltage between tip and sample (0 V, mechanical cycling, and 1 V, hot switching) using protocol P2 for data series B through E. The data sets and colors used in this plot correspond to those used in figure 3.14. Error bars correspond to the standard deviation of 1156 regularly-spaced FvD measurements collected over the same 1 x 1 μm^2 surface region.

The adhesion behavior does not exhibit consistent trends, and therefore, reliable conclusions can not be drawn to relate resistance changes with adhesion for test series B through E. The force of adhesion was found to increase with decreased conductivity for some tests (notably, B3) and yet decrease in other instances (notably, C2). C3 was an outlier that demonstrated a measureable increase in adhesion. More striking is that the force of adhesion was much larger for series B though E tests than for series A tests. In order to investigate the origin of this observation, the work of adhesion is shown in figure 3.19 and representative surface scans for the test surface in series A and series B through E measurements are shown in figure 3.20.

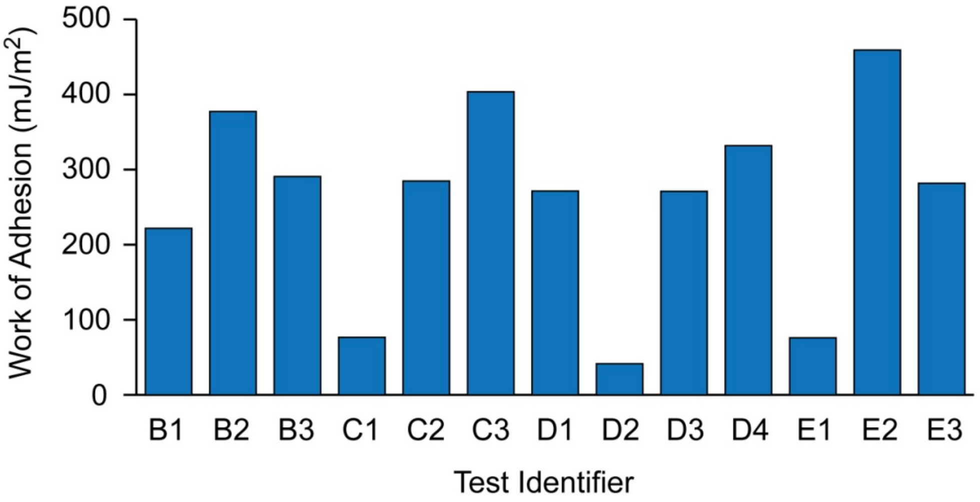

Figure 3.19: Work of adhesion measured at the end of testing (after ~10^9 cycles) for test series B through E cycled with protocol P2. The probe tip radii used to extract the work of adhesion from the force of adhesion were calculated from TEM profiles after cycling and are listed in table 3.2.

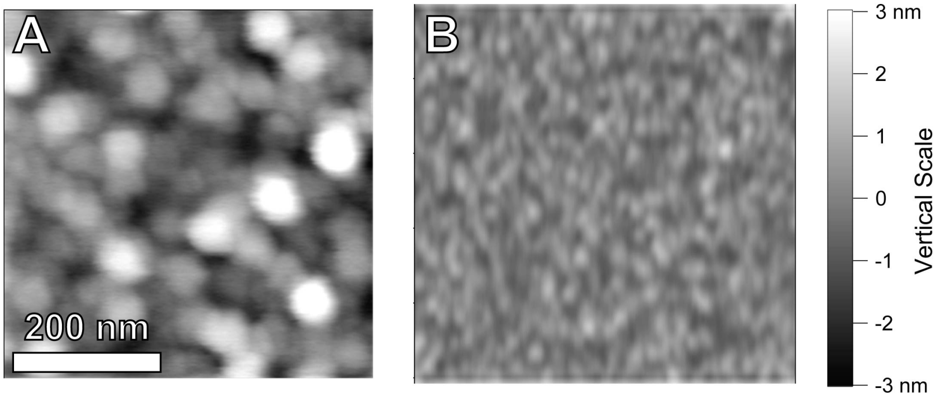

Figure 3.20: Height profiles of (A) the Pt counter surface used during cycling for series A measurements and (B) series B through E measurements. Pt surfaces in (A) were deposited on glass cover slides that resulted in higher film roughness. Both scans were performed over a 500 x 500 nm^2 region while collecting 256 x 256 data points. First order line fits were applied to both sets of data.

The work of ahdesion at the end of testing for series B through E was found to be 41 – 460 mJ/m^2, while that of series A was 9 – 62 mJ/m^2. Recall that all test series were performed on Pt/Pt interfaces and the work of adhesion extracted by measuring probe tip radii using the same method. The origin of the differences in measured force of adhesion and work of adhesion is thus hypothesized to arise from the roughness of the substrate. Pt depositions for the series A tests were performed on glass cover slides, while those of series B through E tests were performed on 100 Si wafers. The roughness measured over a 500 x 500 nm^2 scan for the films deposited on glass slides and Si substrates were measured at 1.2 and 0.49 nm RMS, respectively. Because the deposition conditions were similar for all series, the additional roughness in the series A films is attributable to the underlying substrate roughness. Jacobs *et al*. [119] have shown that nanoscale roughness can have a large (order of magnitude) effect on the measured work of adhesion. The work of adhesion for measurement series B through E demonstrates that even for low roughness Pt countersurfaces, the work of adhesion only just approaches that expected for metallic surfaces, and thus adsorbed organic contamination has a measureable effect on reducing the adhesive forces between these surfaces.

3.5 Degradation Mechanisms of Nanoscale Platinum/Platinum Contacts

Based on the observations of sections 3.3 and 3.4, three mechanisms of degradation for single asperity Pt/Pt contacts were observed and a schematic of these machenisms are shown in figure 3.21.

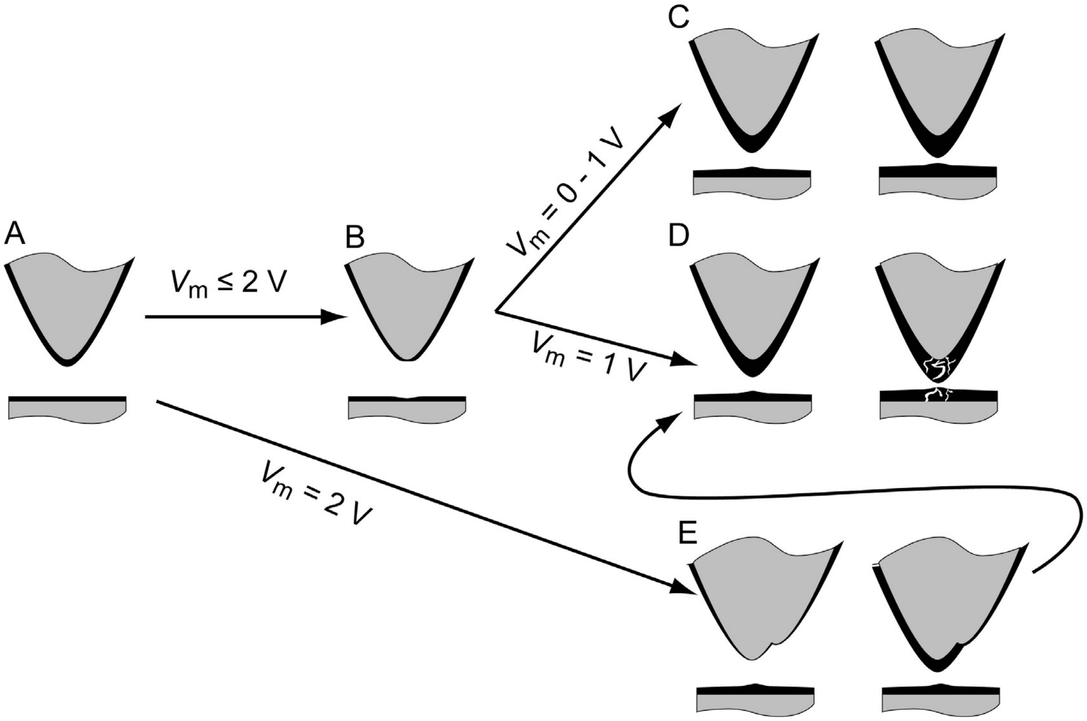

Figure 3.21: Degradation mechanisms observed for single asperity Pt/Pt interfaces cycled under mechanical and hot switching. (A) Adsorbed organic contaminants (C and 0) of ~1.3 nm-thickness were present on the Pt surfaces due to exposure to laboratory air. (B) Initial cycling of the contact resulted in removal of adsorbed material and/or broadening of the contact area that resulted in increased conducitivity. (C) Continued cycling of the contact under low to moderate voltages resulted in growth of TP and an increase in contact resistance. (D) Cycling under moderate voltages lead to periods of TP formation and periodic loss or breakdown of TP resulting in decreased contact resistance. (E) High electrical power during cycling resulted in gross changes to tip shape and, in one case, lower contact resistance attributed to the exposure of a cleaner Pt interface. Continued cycling of the probe resulted in eventual formation of TP and an increase in contact resistance.

The three failure mechanisms shown in figure 3.21 depend on electrical power applied to the contact. In all cases, exposure of the Pt surfaces to laboratory air resulted in adsorpotion of 1 to 1.3 nm of organic (C and O) contamination. For cycling under low power ($V_m \leq 1$ V), an initial run-in, which likely includes nanoscale deformation of the contact, an increase in nanoscale roughness of the tip and surface, and initial removal of adsorbed contamination resulted in an initial increase in conductivity. Continued cycling led to the generation of TP at the contact interface that increased contact resistance. Normal contact stresses of several GPa were not sufficient to fully penetrate these layers. Under moderate electrical power (V_m = 1 V), TP formed during cycling was found to either ablate, break down ,or thermally degrade resulting in periods of increased conductivity. Despite this regeneration of the contact, trends indicated this higher electrical power demonstrated the potential for more TP generation. At high power (V_m = 2 V) the interface was observed to degrade through gross material loss likely originating from Joule heating of the interface. Deformation of the tip was found, in one case, to expose less contaminated tip material. However, the new equilibrium tip shape was then found to contaminate with TP that resulted in large resistance increases. In all cases, TP formation was the dominant mechanism of contact resistance increase.

3.6 Comparison of Single Asperity Results to Multiasperity Systems

Qualitative agreement can be showed between results of the single asperity Pt/Pt tests here and existing multiasperity contact work. Figure 3.22 shows the results of single asperity Pt/Pt contacts mechanically cycled in laboratory air (test series C) re-plotted with data from Chen *et al*. [50]. In their work, a custom-fabricated AFM probe with a ~2.5 µm-diameter flat punch profile and coated with Pt was cold cycled (voltage only applied after contact closure) in ambient laboratory conditions against a Pt substrate.

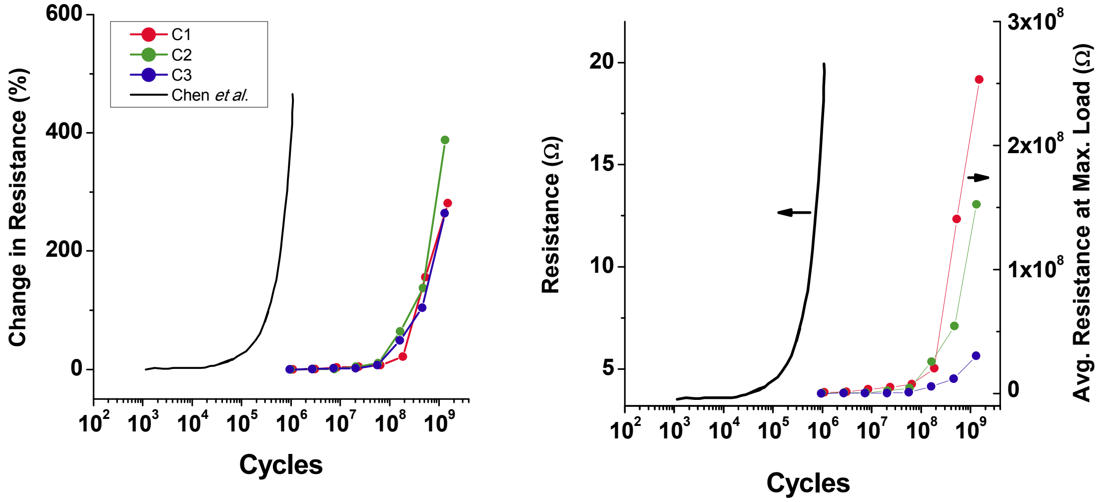

Figure 3.22: (Left) Change in resistance as a function of contact cycles and (right) absolute resistance as a function of cycles for (left axis) the data obtained by Chen *et al*. [50] for multiasperity Pt/Pt contact and (right axis) single asperity Pt/Pt contacts investigated here. The change in resistance (right) is of similar magnitude for multiasperity and single asperity contacts. However, initial resistance of both contacts differs by ~10^4 for multiasperity vs. single asperity tests.

The mulitasperity contacts investigated in Chen *et al*. [50] demonstrate dramatically lower contact resistance. Initial contact resistance was around 3 Ω, approximately four orders of magnitude lower than for single asperity testing. This is attributed to the larger contact areas and local stresses encountered in multiasperity testing. For instance, a lower bound for contact area in the work of Chen *et al*. [50] can be estimated by assuming the loading force is a product of the material hardness and real contact area. On this basis, the ratio of theoretical contact resistance between single asperity testing here and multi-asperity work is on the order of $10^{-3} – 10^{-4}$. Therefore, the size of the contact almost entirely accounts for differences in initial contact resistance between the two studies. Additionally, it has been shown that the highest asperities on a multiasperity surface can encounter stresses above the hardness of the material that can lead to significant deformation. This deformation can displace contaminant films after the first few contacts [59] leading to a more conductive interface. Finally, due to the roughness of multiasperity surfaces, regions not in interpenetrating contact but close to each other may contribute to tunneling sites that reduce the overall resistance of the contact. This comparison demonstrates that the initial condition of the single asperity Pt/Pt contacts investigated here express similar initial contact resistance to existing multiasperity work when accounting for scale.

When plotted with over a logarithmic cycle scale and linear resistance scale (as in Chen *et al*. [50]), both the single asperity Pt/Pt tests here and muliasperity work show the same qualitative resistance changes. Low contact resistance is seen to dramatically increase at some critical number of cycles. However, this increase is seen at ~10^6 cycles for multasperity cycling and ~10^8 cycles for single asperity contacts cycled in series C measurements. This transition point is also higher for series A measurements (~10^7 cycles, not shown in figure 4.24). Recall that series A measurements included slower FvD cycling from 100 – 10^6 cycles. Furthermore, the measurements shown here for mulitasperity Pt/Pt contacts were performed at several Hz. The earlier degradation seen in series A measurements when compared to series C measurements and the longer lifetimes of both series A and C measurements when compared to multiasperity Pt/Pt cycling suggest that cycling frequency may have an impact on TP formation. In addition, cycling in the single asperity tests presented in this thesis was subject to lateral AFM drift (measured to be ≤ 400 nm during the duration of testing) during protocol P1 testing or intentionally performed over a 1 x 1 μm^2 surface region during protocol P2 testing. This means that TP formation was likely limited to only the probe tip, which could delay the onset of contact increased contact resistance.

3.7 Contact Regeneration under Shear Loading

In sections 3.4 and 3.5, insulating TP formation was observed due to contact cycling in a variety gaseous and electrical environments. In order to demonstrate the potential for removal of this insulating film, scanning under load, shear, and electrical bias was performed on test sample C1 after cycling and TEM imaging. This probe tip had previously demonstrated an increase in contact resistance of ~2.5 orders of magnitude. In order to regenerate the contact, the probe tip was taken to a new Pt surface location and scanned at a load of 15 nN over a 2 x 2 μm^2 area under a tip-surface electrical bias of 200 mV. Significant current response was observed after only several scan lines. Figure 3.23 shows the current distribution measured between the Pt-coated probe tip and Pt counter surface before cycling, after cycling for ~10^9 tip-surface interactions, and after shear regeneration of the contact.

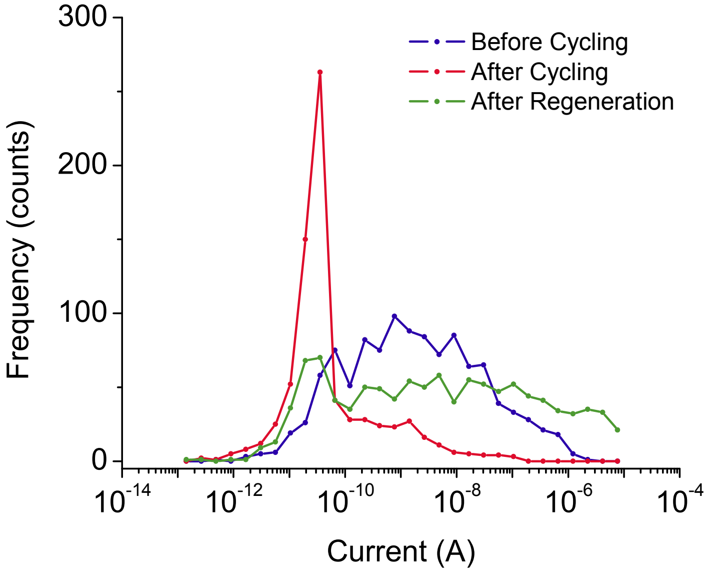

Figure 3.23: The current distribution measured at a maximum contact force of 40 nN from 1156 FvD/IvD measurements taken before contact cycling, after contact cycling for ~10^9 cycles, and after the application of load, shear, and electrical bias to the probe tip C1. A significant improvement in tip-surface conductivity is observed after applying shear to the contact.

Figure 3.23 shows that significant decrease in contact resistance may be achieved by shearing the contact interface. In this figure, a significant decrease in conductivity is observed after 10^9 contact cycles such that the majority of measured current was found to be within the noise floor of the current amplifier (~40 pA). Application of a shear load led to current responses exceeding pre-cycling measurements.

The effect of conductivity improvement due to shear loading was also repeatedly observed before cycling occurred. In protocol P2, cleaning contact scans performed before contact testing preceded initial FvD/IvD loading of the interface. The cleaning scans were performed by rastering the Pt-coated probe tip across the Pt sample surface. FvD/IvD measurements were then performed over the same Pt surface location by bringing the tip into and out of the surface without the direct application of shear loads. All FvD/IvD measurements were performed within 40 minutes of scanning the surface under shear load. Figure 3.24 shows the current distribution measured during the last cleaning scan (of three total scans) of a Pt/Pt contact at 15 nN and the conductivity at 15 nN load of 1156 FvD/IvD measurements corresponding to measurement B2 described in table 3.2

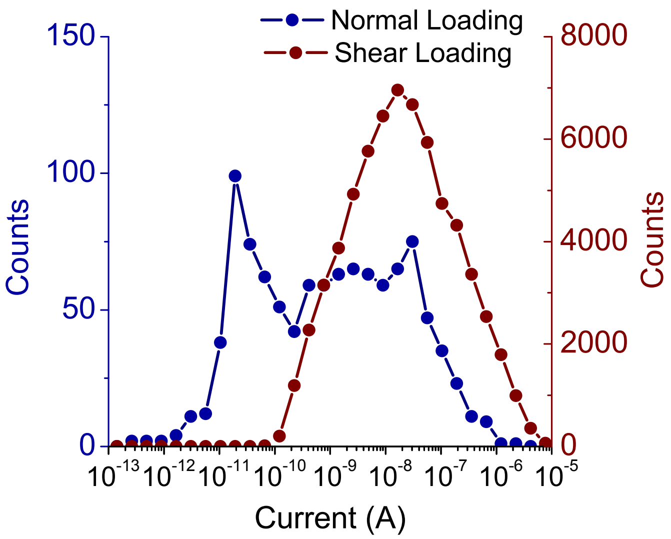

Figure 3.24: The current distribution measured at a contact force of 15 nN for lateral scanning of a Pt surface (shear loading) and 1156 FvD/IvD measurements taken without applying shear (normal loading). All measurements were taken before cycling of the contact interface and with a tip-sample bias of 200 mV. Current measured during shear scanning of the interface demonstrates lower average contact resistance.

Figure 3.24 shows that the application of shear during contact significantly improves conductivity at the Pt/Pt interface. Tip-surface conductivity measurements within just minutes after shear loading already exhibit a significant increase in contact resistance. This corroborates observations from XPS in that Pt surfaces aggressively cleaned with Piranha rapidly re-contaminate. These findings suggest that shear during contact closure may be used to both decrease contact resistance during every closure cycle of a nanoscale electrical contact interface and regenerate the contact after TP formation.

3.8 Final Remarks

This chapter detailed the results of testing Pt/Pt single asperity contacts in N_2-purged and laboratory air environments both with and without the application of a tip-surface electrical bias. Contact resistance increases due to the formation of low density insulating films on the probe tip were correlated with high tip-surface electrical bias during cycling and operation in humid, aerobic environments. It was observed that operation in N_2 environments can significantly reduce TP formation at the contact. Shearing of the contact was then demonstrated to result in a significant contact resistance improvement for contacts affected by TP formation and that re-adsorption of contamination on surfaces cleaned by shear occurs within minutes. With this motivation, the next chapter investigates the response of Pt and N-UNCD, a potential next-generation contact material, under load, shear, and electrical bias.

CHAPTER 4: RESULTS AND DISCUSSION FOR NITROGEN-INCORPORATED ULTRANANOCRYSTALLINE DIAMOND AND PLATINUM CONTACTS SUBJECTED TO LOAD, SHEAR, AND ELECTRICAL BIAS

4.1 Overview: The Effect of Load, Shear, and Electrical Bias on Pt/Pt and Pt/Nitrogen-incorporated Ultrananocrystalline Diamond Contacts

In section 3.7, it was shown that shearing of a Pt/Pt nanocontact results in lower contact resistance and could be utilized to regenerate a contact. With this motivation, both Pt and a conductive variant of diamond, nitrogen-incorporated ultrananocrystalline diamond (N-UNCD), were evaluated under load, shear, and electrical bias in order to mimic electrical contact effects as they might be encountered in a nanoscale switch with wiping action. N-UNCD was investigated because similar thin films have demonstrated properties useful for electrical contacts - high hardness, small grains that are amenable to micro-/nanofabrication techniques [120], robustness to sliding in both humid and dry environments [121], and ohmic electrical contact behavior with metals [101].

This chapter presents the results of scanning both Pt/Pt and Pt/N-UNCD contacts under load, shear, and electrical bias. Section 4.2 describes the effect of scanning Pt-coated AFM probes over N-UNCD and Pt at loads ≤50 nN. Section 4.3 describes the effect of scanning with Pt/N-UNCD interfaces with loads ≥50 nN and reports chemical information from these regions.

4.2 Current Response of Platinum/Platinum and Platinum/Nitrogen-incorporated Ultrananocrystalline Diamond Interfaces Subject to ≤50 nN Normal Load, Shear, and Voltage in Laboratory Air and Nitrogen Purged Environments

To evaluate the response of Pt and N-UNCD nanocontacts under load, shear, and electrical bias as they might be encountered in NEMS logic switches, scans were performed using AFM with the method described in section 2.7.1. Briefly, commercial contact mode Si AFM cantilevers were coated with 70 – 85 nm of Pt using the Explorer14 sputter coater described in section 2.5.1. These probes were brought into contact with Pt and N-UNCD flat surfaces and multiple scans (referred to as modification scans) were performed over 1 x 1 μm^2 regions in order to evaluate changes to conductivity due to load, shear, and electrical bias. In order to subject the surfaces to conditions representative of a wiping electrical switch contact, a modification bias, V_m, was applied between the tip and surface with the tip serving as the cathode. Scans of increasing voltage were conducted, each at a new location spaced 1 μm from the previous scan. V_m was increased at each scan location from a minimum value 0.25 V for all tests up to a maximum of 8 V for Pt/N-UNCD interfaces and 2 V for Pt/Pt interfaces. The maximum voltage for the tests was selected to to ensure tip failure due to melting.

Probing scans of 1 x 1 um^2 size with a moderate (non-perturbing) probing voltage, V_p, were conducted before each modification scan, and at the end of testing at a location off-site from the modification scans, in order to check the electrical integrity of the probe. All scans were performed with an applied load of 50 nN for Pt/N-UNCD interfaces and 25 nN for Pt/Pt interfaces. All scans were performed in the lateral scanning direction, at a scan rate of 0.2 Hz, a total of 64 scan lines per surface image, and while collecting 1024 scan points per line. Scans of approximately 7 minutes in length were taken with the probe out of contact from the surface before beginning probing or modification scans in order to minimize lateral and load drift. The cantilever baseline load offset was evaluated before every probing and modification scan in order to ensure accurate loading during the scanning process.

A total of three tests were conducted using an automated scanning routine programmed in the Igor Pro language (WaveMetrics, Inc., OR, USA) and undertaken on an Asyulm MFP-3D. Current was recorded during scanning using the logarithmic amplifier described in section 2.2. Probe stiffness was determined using thermal calibration and the tip was gently brought into contact with the counter surface using the soft engage method described in 2.6.1. Table 4.1 describes the contact material pairs, environment, and probing voltages investigated for tests on Pt and N-UNCD in this section and are referred to as M series tests.

Table 4.1: Test identifier, counter surface material, modification voltage range, environment, and scan load during modification and probing scans for series M measurements. A new Pt-coated AFM probe and surface location were investigated for each test.

Test Identifier	Counter surface material	Modification voltage, Vm, range	Environment	Load during scanning (nN)
M1	N-UNCD	0.25 – 8.0	Laboratory air	50
M2			N2 purged	
M3	Pt	0.25 – 2.0	Laboratory air	25

Figure 4.1 shows a typical series of current images taken during modification scans for measurement M1 under a modification voltage of 2 V. Current decreased due to load, shear, and voltage as scanning progressed. Histograms of current for the first and seventh scan are also shown in figure 4.1 and demonstrate a significant shift towards a lower current response.

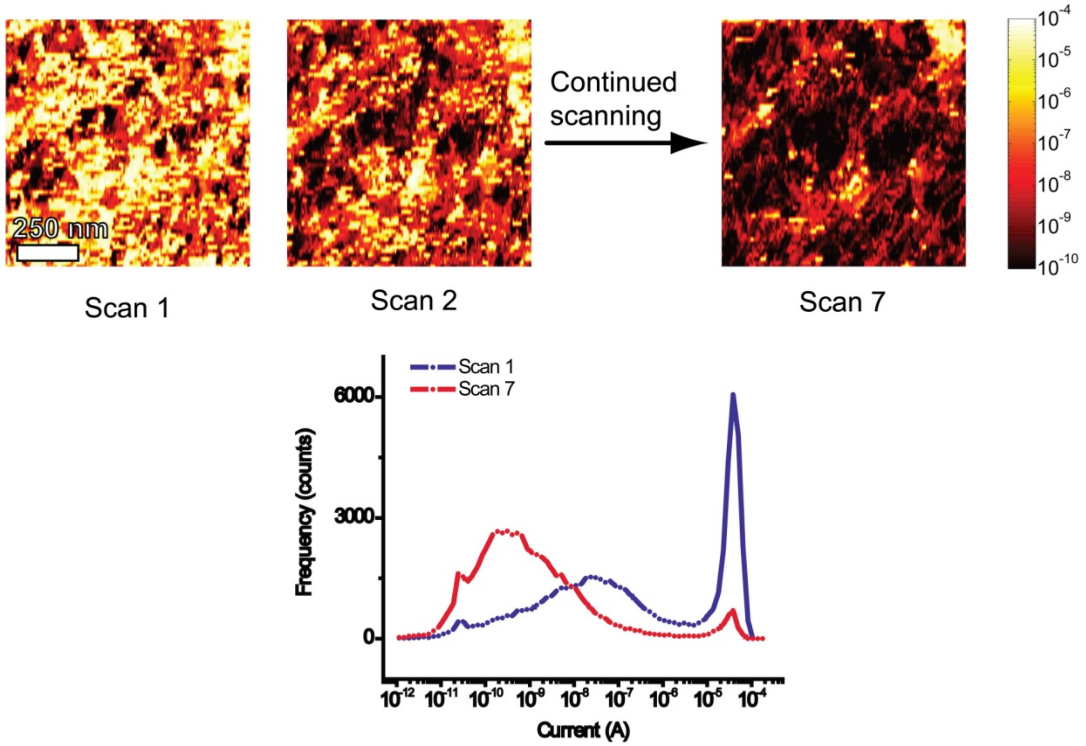

Figure 4.1: Modification scan of N-UNCD with a Pt-coated AFM probe. (Top) Seven scans of 64 scan lines and 1024 scan points at a rate of 0.2 Hz were performed at 1 x 1 μm^2 location of N-UNCD. Current was measured during scanning at a modification voltage, V_m, of 2 V for these images, and corresponds to conductivity data shown for measurement location 6 in figure 4.2 with a scan load of ~50 nN. (Bottom) The conductivity histogram over a logarithmic range for scan 1 and scan 7 demonstrates an overall reduction in current due to load, shear, and electrical power. The histogram peak that appears at ~40x10^{-11} A for both the first and final scan represents low current noise contributions from the current amplifier that dominate during high contact resistance.

Figure 4.1 shows that distribution of surface conductivity of N-UNCD spanned several orders of magnitude much like that of Pt surfaces exposed to air. Like the Pt/Pt interfaces investigated in chapter 3, these variations in surface conductivity of N-UNCD are attributed to the nanostructure of the film, surface roughness, and adsorbed surface contamination. However, in the case of N-UNCD, the structure of the film may dominate the surface conductivity response.

Bhattacharyya *et al*. [100] found that addition of nitrogen to UNCD results in significantly larger grain boundaries and proposed that conduction occurs via these grain boundaries. Thus, non-conductive regions of the film may originate at grain sties. In addition, the surface studied here demonstrated significant roughness (~ 40 nm RMS over a 1 x 1 μm^2 area). Therefore, some of the variation in conductivity across the surface may be ascribed to sampling of conductive grain boundaries, non-conductive grains, and complex geometric interactions between the sharp probe tip and rough surface.

Current was measured during scanning, which permits the real time observation of changes to conductivity of the interface as a result of load, shear, and electrical bias. Figure 4.2 and figure 4.3 show current measured during multiple modification scans, each at a new location and of increasing V_m, and for single probing scans with bias V_p performed before each modification scan for tests M1 (laboratory air, 28.3 – 42.7 %RH during testing) and M2 (N_2 purged, 2.3 – 4.6% RH during testing). The median, lower quartile, and upper quartile current response based are reported for all measurements. Scanning was performed with a 50 nN applied load.

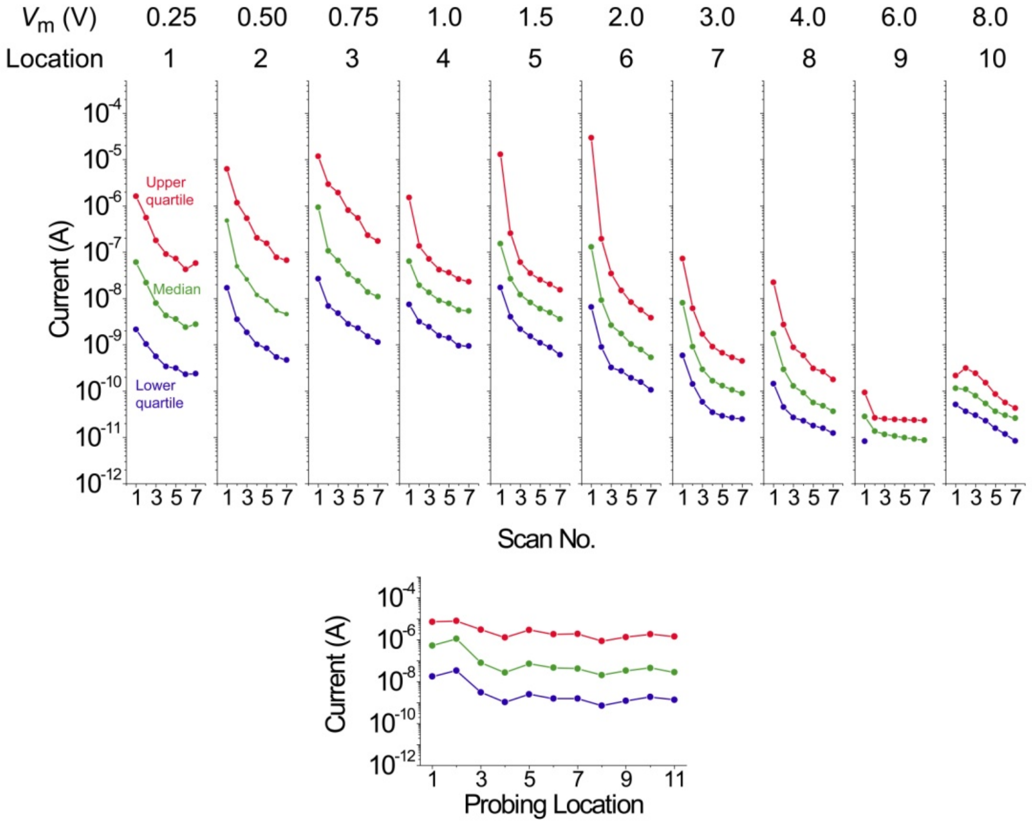

Figure 4.2: (Top) Median, upper quartile, and lower quartile current from data measured during repeated scanning of 1 x 1 µm^2 regions of N-UNCD with a Pt-coated AFM probe at a load of 50 nN in laboratory air (measurement M1). 10 independent locations were scanned for seven passes under load, shear, and electrical bias with increasing modification voltage, $V_{m,}$ at each new location. Conductivity of the interface decreased with continued scanning at each given location, and conductivity was progressively reduced overall at higher V_m. The lack of lower quartile data (blue line) for V_m = 6.0 V (location 9) occurred because the lower quartile data was below zero (within the noise floor of the amplifier) and cannot be represented on a logarithmic y-axis. (Bottom) Conductivity of the probe tip-surface interface was evaluated before each modification scan and after all tests were completed by scanning previously untested regions of the film near the modification regions in order to check the electrical integrity of the probe tip. The voltage during all probing scans, V_p, was 1 V, load was 50 nN, scan rate was 0.2 Hz, and 64 scan lines and 1024 scan points were collected. Each probing location number identifies the tip integrity evaluation scan performed before the modification scan of the same location number. For instance, probing location one was measured next to (but not intersecting) modification scan location one before data for modification scan location one was collected.

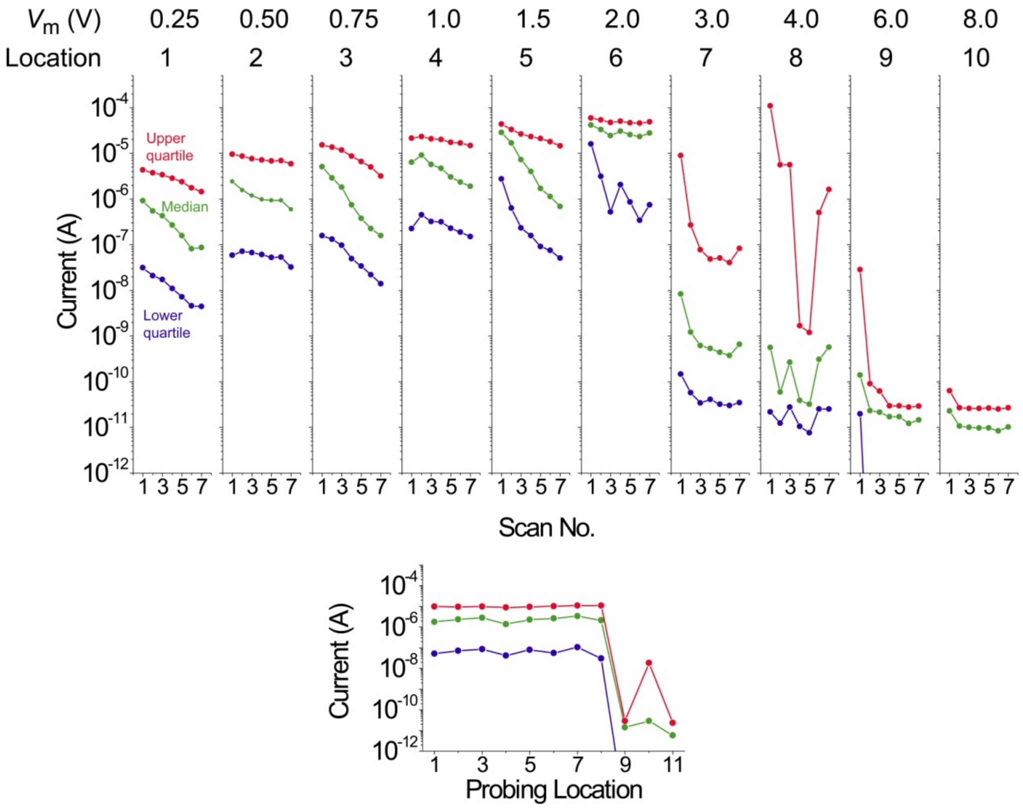

Figure 4.3: (Top) Median, upper quartile, and lower quartile current from data measured during repeated scanning of 1 x 1 μm^2 regions of N-UNCD with a Pt-coated AFM probe at a load of 50 nN in an N2 purged environment for measurement M12. 10 independent locations were scanned under load, shear, and bias for 7 scans each with increasing modification voltage, $V_{m,}$ at each new location. Conductivity of the interface decreased with continued scanning at each given location, and conductivity was progressively reduced overall at higher V_m. However, unlike in air, the conductivity did not show an overall decrease with applied bias until 3.0 V was applied, at which point a large decrease was observed, which continued at subsequent voltages. (Bottom) Conductivity of the probe tip-surface interface was evaluated before each modification scan and after all tests were completed by scanning previously untested regions of the film near the modification regions in order to check the electrical integrity of the probe tip. The voltage during all probing scans, V_p, was 1 V, load was 50 nN, scan rate was 0.2 Hz, and 64 scan lines and 1024 scan points were collected. Each probing location number identifies the tip integrity evaluation scan performed before the modification scan of the same location number. For instance, probing location one was measured next to (but not intersecting) modification scan location one before data for modification scan location one was collected.

Significant electrical degradation of the interface was observed for modification scans in both laboratory air (figure 4.2) and N_2 (figure 4.3). This manifested as a decrease in contact resistance as multiple scans were performed over a modification region. The extent of contact resistance increase under load, shear, and electrical bias appeared to correlate with the electrical power applied across the contact during scanning. Higher voltages and currents during modification scanning (larger V_m) resulted in larger decreases in contact resistance regardless of the surrounding environment.

Voltages up to 8 V were applied during scanning for measurements M1 and M2. Loss of the Pt-coating on the AFM probe tip was presumed to occur during modification scanning of test M2 at location 8 (V_m = 4 V) as indentified by a substantial decrease in conductivity during probing scan 9 that was performed after the V_m = 4 V modification scan. High contact resistance and irregular behavior were seen for the following modification scans at 6 and 8 V. The origin of this sudden increase in contact resistance was hypothesized to occur from Joule heating, mechanical deformation (fracture, plastic deformation, and delamination) due to shear, or a combination of both that resulted in loss of the Pt coating from the Si cantilever tip.

Why loss of the conductive tip occurred when scanning in N_2 and not laboratory air is not clear. Heat dissipation at an AFM probe tip-surface interface has been shown to depend on and conductive and radiative mechanisms that are attributed to the contact and surrounding meniscus layer [122]. Furthermore, the meniscus formed between a probe tip in contact with a counter surface depends on the relative humidity in the surrounding environment [123]. Therefore, heat transfer may increase and contact softening decrease for tip-surface interfaces operating in humid environments due to the presence of water at the contact interface. Thus, a meniscus may have been present during the experiments in air, which permitted more heat dissipation through the contact and thus reduced thermally-induced deformation mechanisms or wear of the tip.

Changes to Pt/N-UNCD interface conductivity due to load, shear and electrical bias were found to extend beyond or occur immediately at the contact zone for measurements of high V_m in both N_2 and laboratory air. Tip-surface current was expected to increase with increasing V_m.

However, median current measured during the first modification scan for both M1 and M2 for V_m≥3.0 V was lower than that measured for V_m<3.0 V. For test M1, this behavior was observed for modification scans above 3.0 V even though probing scans clearly revealed the continued existence of a highly conductive probe tip.

The origin of the immediate decrease in Pt/N-UNCD interface conductivity observed while scanning with a tip-surface voltage ≥3.0 V has two potential explanations. The mechanism leading to decreased interface conductivity may occur immediately under the probe tip location as it is rastered over a particular N-UNCD surface location. Alternatively, the mechanism driving interface conductivity decreases may extend outside of the immediate tip-surface contact zone such that each subsequent line pass during scanning experienced a surface location already degraded by the previous scan line. The probe tip profiles in this study were not measured using TEM. However, because the probe tips used to conduct these experiments were fabricated in a similar fashion to those tested in section 3.4, it is reasonable to assume probe tip radii on the order of 10 – 120 nm. For a 50 nN load and assuming reasonable mechanical parameters for the contact materials[8], the contact diameter according to DMT theory would be in the range of 1.5 to 7.7 nm. The separation distance between scan lines during modification scans was ~16 nm. Therefore, the lower median current measured during the first modification scan for V_m≥3 V indicates that the formation of an insulating interface occurred as the probe tip was passing over the surface or that insulating interface formation extended to a zone outside of each individual scan line that affected conductivity measurements on each subsequent scan line. This result has implications for multiasperity contacts of Pt/N-UNCD in that even if the highest points of asperity contact (the real contact area) do not mechanically interact laterally, contact resistance increases due to the presence of a critical voltage may be felt some distance away from the immediate zone of contact.

---

[8] Parameters reasonable for the contact between Pt and N-UNCD were assumed. Here E_t = 130 GPa, E_s = 600 GPa, v_t = 0.3, v_s = 0.1, and W = 30 mJ/m^2.

In order to compare the response of the Pt/N-UNCD interface to electrical power under similar loads in N_2 and laboratory air environments, the degradation in current response of the interface was compared to the electrical power through the contact for measurements M1 and M2. In figure 4.4, the reduction in median conductivity from a previous modification scan is plotted as a function of the median power through the contact and is fit using a logarithmic relation of the form

$$\frac{I_{med,f} - I_{med,i}}{I_{med,i}} = k \log(V_{med} \cdot I_{med,i}) + b \qquad \text{Eq. 4.1}$$

where $I_{med,i}$ and $I_{med,f}$ represent the median current during the i^{th} scan and and $i^{th} + 1$ scan, k is the slope, and b is the offset. The data plotted in figure 4.4 excludes scans for $V_m > 2.0$ V (for which tip-surface conductivity decreases were immediate) as the degradation for high voltage scanning was immediate and not incremental as observed during low voltage scanning.

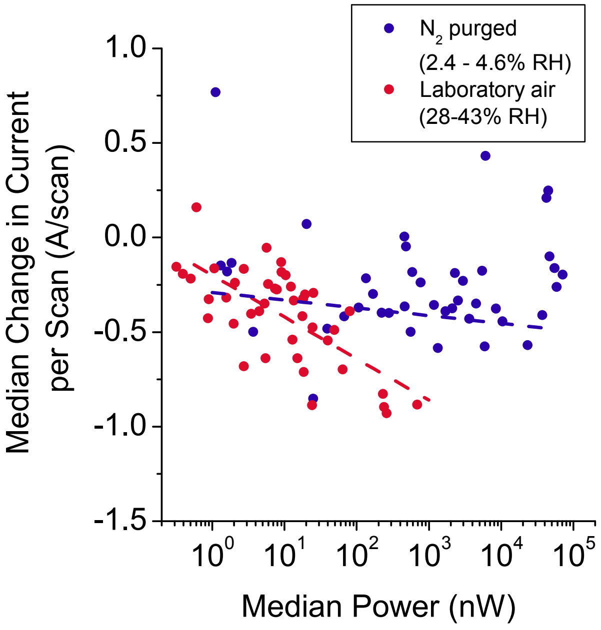

Figure 4.4: Median change in current from surface current maps measured from the initial scan to the present scan as a function of median power during the initial scan for scanning in an N_2 purged environment (blue) and laboratory air (red). Under comparable load, shear, and electrical power, scanning in laboratory air leads to larger changes in conductivity than in N_2.

Figure 4.4 shows that the magnitude of conductivity degradation is dependent on the operating environment and power through the contact. The slope of the conductivity data fit to a logarithmic function reveals an average of a decade of relative conductivity decrease per nW of power per scan of 0.22 and 0.04 for N-UNCD exposed to load, shear, and electrical bias in laboratory air and N_2, respectively. For instance, at 100 nW of power, the conductivity of N-UNCD scanned under 50 nN would decrease by one order of magnitude for every scan in laboratory air and every five scans in N_2. The implication of these results is that electrical contacts of Pt/N-UNCD exposed to load, shear, and electrical bias will experience less degradation in interface conductivity when operated in inert environments.

Based on the results of M1 and M2, it was not clear if degradation of conductivity observed between N-UNCD and Pt contacts was the result of film buildup, indicative of a chemical diffusion processes at the contact, or of atomic-scale modification of the N-UNCD sample itself. The conductivity in N-UNCD is well-established to result from the presence of nitrogen in the grain boundaries of the film. These grain boundaries are amorphous and have a high fraction of carbon bonded in the sp^2 hybridization. However, the binding energy of N inclusions in the grain boundaries has not been described, and given the amorphous nature of the grain boundaries, a distribution of binding energies of the N atoms is expected. It is possible that under sufficient energy (stress and voltage) field-driven diffusion of poorly-bound N atoms in the grain boundaries could result in depletion of carriers and a reduction of conductivity of the interface. Alternatively, well-characterized systems such as Si, which readily forms an oxide in air, have demonstrated voltage-assisted oxidation. The results of tests M1 and M2 do not lead to a clear interpretation of the exact degradation mechanism, although the observation that oxygen and water in the test environment lead to decreased conductivity suggest oxidation or a surface film as the likely culprit.

To place the effects of load, shear, and electrical bias on Pt/N-UNCD contacts in context of degradation mechanisms observed in chapter 3 for Pt/Pt contacts, similar probing and modification scans were performed between Pt/Pt interfaces. Figure 4.5 shows the results of scanning a Pt-coated AFM probe in contact with the same Pt substrate interrogated in chapter 3 under a load of 25 nN and in laboratory air (29.0 – 37.0 % RH during testing). Laboratory air was chosen in order to replicate the electrical contact environment that led to the largest degradation of the Pt/N-UNCD interface. Modification voltages below 2 V were used in testing of Pt/Pt interfaces as the results of chapter 3 cycling at 2 V suggested tip-surface melting would occur at or near this voltage.

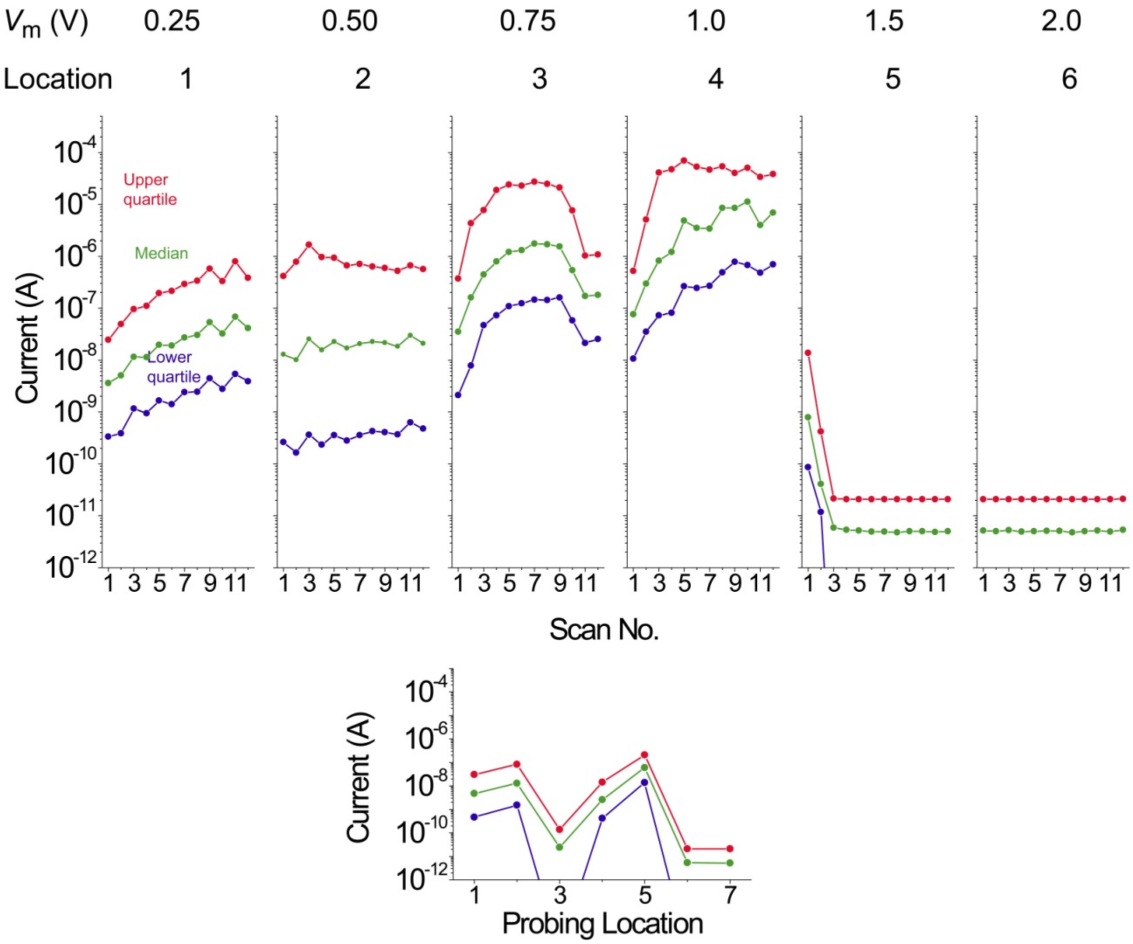

Figure 4.5: (Top) Median, upper quartile, and lower quartile current from data measured during repeated scanning of 1 x 1 μm^2 regions of Pt with a Pt-coated AFM probe at a load of 25 nN in laboratory air. 6 independent locations were scanned with increasing modification voltage, V_m. Conductivity of the interface increased with continued scanning. (Bottom) Conductivity of the probe tip-surface interface was evaluated before each modification scan and after all tests were completed in order to check the electrical integrity of the probe tip. The voltage during all probing scans, V_p, was 0.25 V, load was 25 nN, scan rate was 0.2 Hz, and 64 scan lines and 1024 scan points were collected.

In contrast to Pt/N-UNCD scans under higher loads and voltages, which demonstrated a significant decrease in conductivity, Pt/Pt interfaces scanned at biases of 1 V or less demonstrated a progressive increase in conductivity. This suggests that the contact is being cleaned by the scanning process. In figure 4.5, all modification scans demonstrated increasing conductivity with the exception of the final two modification scans of for $V_m \geq 1.5$ V. In the case of $V_m = 0.75$, conductivity degradation is ascribed to the adherence of a particle of contamination on the probe tip that persisted even after moving to new probing locations (probing scan locations 3 and 4 on the bottom plot of figure 4.5). Contact degradation for $V_m \geq 1.5$ V is attributed to melting or fracture of the probe tip. This was expected based on AFM and TEM probe tip profiles for V_m = 2 V measurements shown in chapter 3, which showed evidence of melting of the probe tip for $V_m > 1$ V and the work of Lo and Bain [83] that showed similar loss of Pt coatings on AFM probes at similar voltages [83]. When compared to the Pt/N-UNCD scans, Pt/Pt interfaces scanned under load, shear, and electrical bias demonstrated similar initial contact resistances but did not experience the degradation mechanism observed on N-UNCD surfaces.

4.3 Friction and Current Response of Platinum/Nitrogen-incorporated Ultrananocrystalline Diamond Interfaces Exposed to ≥50 nN Normal Load, Shear, and Electrical Bias in Humidified Nitrogen and Nitrogen Purged Environments

In section 4.2, it was shown that contact, shear, and electrical bias leads to conductivity degradation at a Pt/N-UNCD interface. Comparison of Pt/N-UNCD to Pt/Pt interfaces suggested that the origin of this effect was the buildup of insulating films unique to the Pt/N-UNCD interface and catalyzed by the presence of the N-UNCD surface. In order to explore the chemical origins of this insulating film and attempt to reduce its effect, the N-UNCD film investigated in section 4.2 was interrogated using AFM with loads of 50 nN and greater and the scan area interrogated chemically using photoemission electron microscopy (PEEM), a laterally-resolved variant of near edge X-ray adsorption fine structure (NEXAFS) spectromicroscopy.

All scanning in this section was performed using a Veeco Dimension 3100 AFM, described in section 2.1.2, using series CSC 37 contact mode probes from µMasch (Innovative Solutions Bulgaria Ltd., Bulgaria). The probes were coated with Pt using the EMITech K575X sputter coater described in section 3.5.1. A Pt thickness of approximately 50 nm was used in all cases. Measurements at low humidity were performed by nitrogen purging the clamshell AFM housing to below 4% RH. Because of the low environmental humidity at the time of testing (<20 % RH), the relative humidity of the chamber was increased for high humidity tests by blowing N_2 through a humidifier filled with DI water. Chemical spectroscopy measurements with PEEM provide a minimum theoretical lateral resolution 50 nm. However, to obtain regions of statistically significant chemical data, scan areas were increased from 1 x 1 μm^2 used in section 4.2 to 4 x 4 μm^2 here. Each modification scan series was performed at a new N-UNCD surface location with a new probe tip. Five consecutive modification scans at a modification voltage, V_m, were performed at each location and a final probing scan was performed over an 8 x 8 μm^2 area. This final probing scan provided a baseline comparison of changes in friction and current from the modified region to the unmodified regions. Current, trace friction, and retrace friction (the maximum number of data channels on the Dimension 3100) were simultaneously obtained. Current was measured using the integrated extended TUNA current amplifier described in section 2.2. In contrast to section 4.2, the initial load on the probe tip was prescribed at 50 nN but allowed to drift to higher loads (typically 70 – 150 nN) due to AFM system drift. Measurements of the baseline load offset of the AFM cantilever before and after scanning were used to determine the extent of load variation during testing.

A total of 11 measurements were performed with modification voltages ranging from 0 V (mechanical contact only) to 10 V. These measurements are referred to as series N measurements here and table 4.2 lists the environment, modification voltage, and load at the end of testing.

Table 4.2: Test identifier, humidity range during testing, modification voltage during testing, and load at the end of scanning for test series N used to evaluate the current and friction response of Pt/N-UNCD at loads of 50 nN and larger. The nominal load at the beginning of the test was 50 nN for all N series measurements. Current was not maintained, presumably due to loss of the Pt-coated AFM tip during some of the V_m=10 V scans.

Test identifier	**Relative humidity range during modification and probing scans (%)**	**Modification voltage, V_m (V)**	**Current maintained during all modification scans**	**Load at end of test (nN)**
N1	<4 (N_2)	0	Yes	41.0
N2	39 - 42	0	Yes	103
N3	17 - 19	0.5	Yes	101
N4	35 - 44	1	Yes	131
N5	<4 (N_2)	1	Yes	143
N6	<4 (N_2)	10	Yes	117
N7	33 - 34	10	Yes	128
N8	38 - 43	10	Yes	73
N9	26 - 44	10	No	80
N10	42 - 45	10	No	60
N11	36 - 41	10	No	113

Changes to current and friction resulting from load, shear, and electrical power were calculated from the final probing scan that overlaid the initial modification region. Figure 4.7 shows the trace-retrace friction and current measured during a probing scan of test N6.

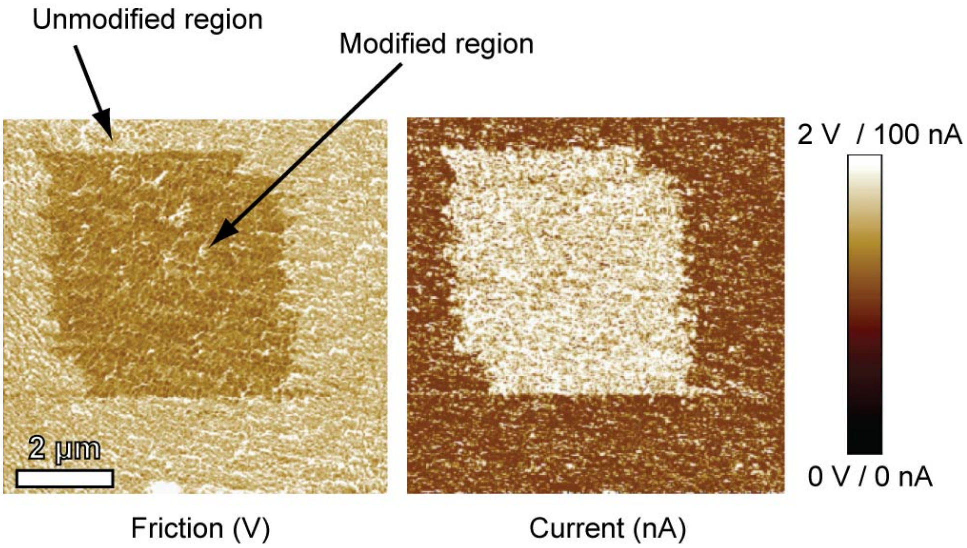

Figure 4.6: (Left) Trace-retrace friction and (right) current measured during the probing scan of measurement N6 with a Pt-coated AFM probe tip on N-UNCD. The modified region located at the center of the image (brightly colored in the current map) was scanned under an initial load of 50 nN that drifted to 117 nN at the end of testing in a N_2 purged environment. Friction decreased and conductivity increased due to load, shear, and electrical power through the contact.

Differences between friction and current in the modified and unmodified region were characterized as a function of modification voltage, V_m, and environment. Figure 4.7 shows trace-retrace friction in the modified and unmodified regions for tests N1 through N8. These correspond to tests where conductivity during the probing scans indicated retention of the Pt tip (continued conductivity of the probe tip-surface during all modification and the final probing scan). In tests N9 – N11, loss of the conductive tip was observed (discussed later) and prevented collection of conductivity data at the end of the test. Figure 4.8 shows the change in current, ΔI, as a function of the change in friction, ΔF_f, for tests N1 through N8. Both values were calculated by subtracting the average value of the modified region from that of the unmodified region. Thus, decreases in friction or current are associated with lower values in the modified region.

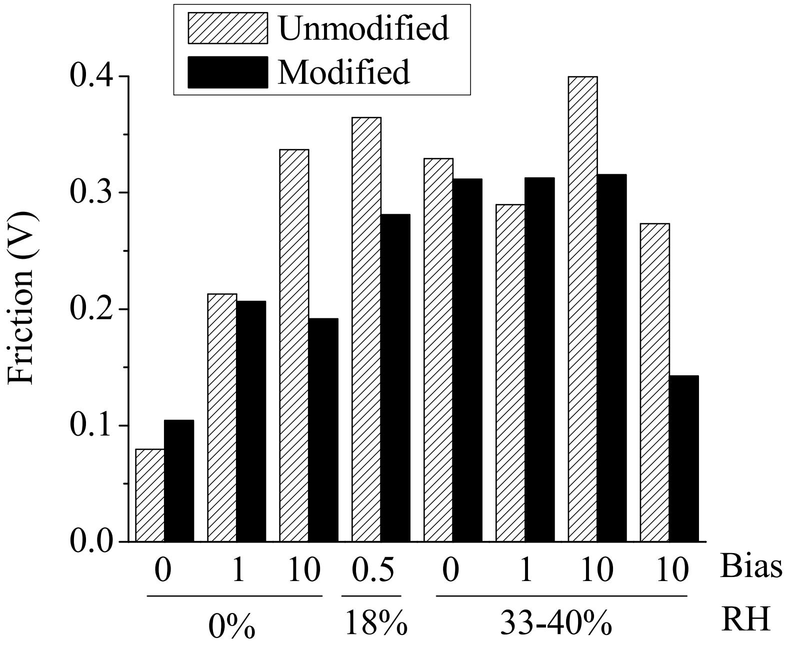

Figure 4.7: Friction force (uncalibrated, but on the same scale for all measurements) in the modified and unmodified regions for tests N1 through N8. Most tests demonstrated a decrease in friction after modification.

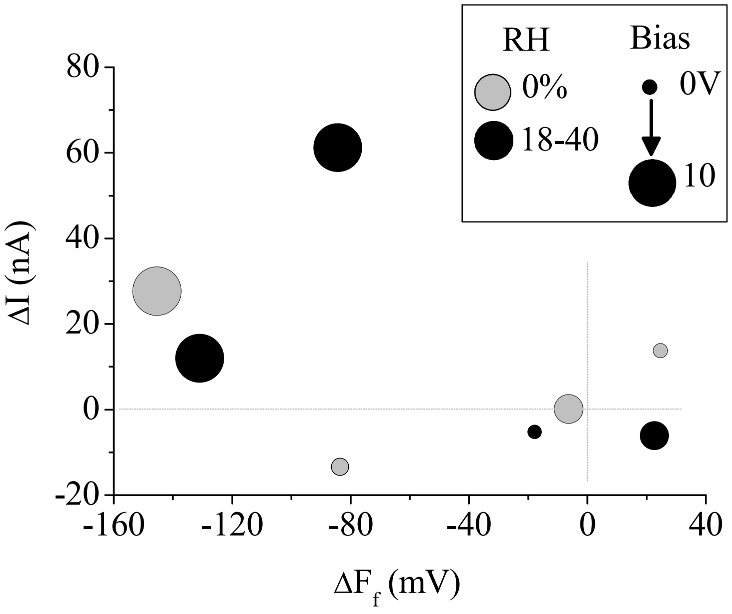

Figure 4.8: Change in current as a function of change in friction for tests N1 through N8. The color of the data point indicates the relative humidity during testing and the size of the data point represents the magnitude of V_m.

Figures 4.7 and 4.8 show that friction decreased and conductivity increased as a result of scanning under load, shear, and electrical bias for the majority of tests. Scanning with high voltages led to the most dramatic increases in current and were generally associated with stronger decrease in friction. The largest conductivity increase due to scanning under load, shear, and electrical bias (10 V, >33% RH) resulted in a modified region with an average conductivity 1.7 times greater than that of the unmodified region. This data indicates that shear of Pt/N-UNCD interfaces under large (>50 nN) or increasing forces removes surface contamination and/or insulating tribolayers formed due to load, shear, and electrical bias.

The chemical state of the scanned surfaces was interrogated using PEEM using the method described in section 2.4.2. The C 1s, O 1s, and N 1s x-ray absorption edges were investigated to evaluate any changes to the structure of the film or N carriers involved in N-UNCD conductivity. During these tests, as mentioned above, some tips lost conductivity (tests N9, 10, 11). In these cases, the Pt coating on the probe tip was found to have melted or fractured as identified in TEM, to expose the underlying Si probe tip. Figure 4.9 shows a representative example of conductivity maintained (test N8) and lost (test N11) during scanning. As we will discuss below, chemical differences in the modified region were directly correlated with the integrity of the Pt contact material on the probe tip. PEEM data is shown in figures 4.10 through 4.12 for surface regions scanned with a 10 V bias. The data is specifically acquired within the modified regions, and for comparison, spectra from an unmodified region is included. Scans performed solely under mechanical loading (no voltage applied during scanning) are not included as the regions could not be identified during PEEM measurements, which indicated little to no changes to the chemical structure at the surface of the N-UNCD film.

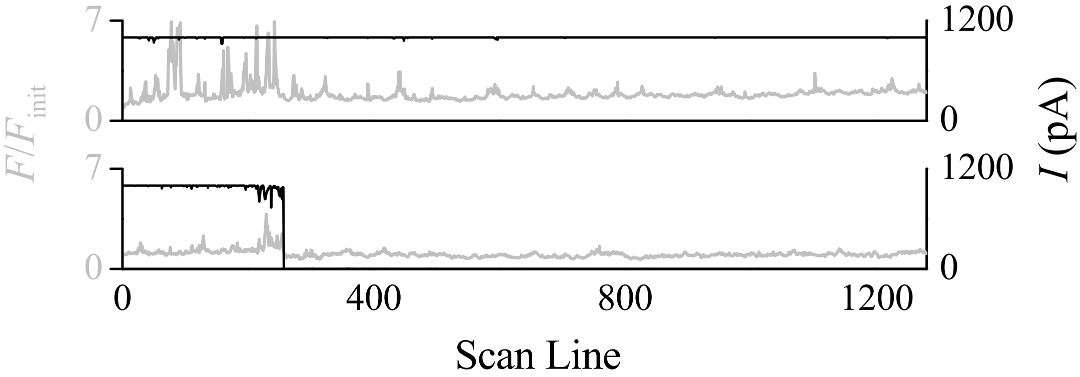

Figure 4.9: (Left axis) Trace-retrace friction averaged for each scan line and (right axis) current during surface modification scanning with V_m = 10 V with relative humidity >33% RH. (Top) Current persisted during scanning and (bottom) loss of the probe tip due to wear, fracture, or melting resulted in a sudden loss of current. The linear current amplifier was set to high sensitivity during modification scans in order to observe these events, which resulted saturation of the current signal during low resistance tip-surface interaction.

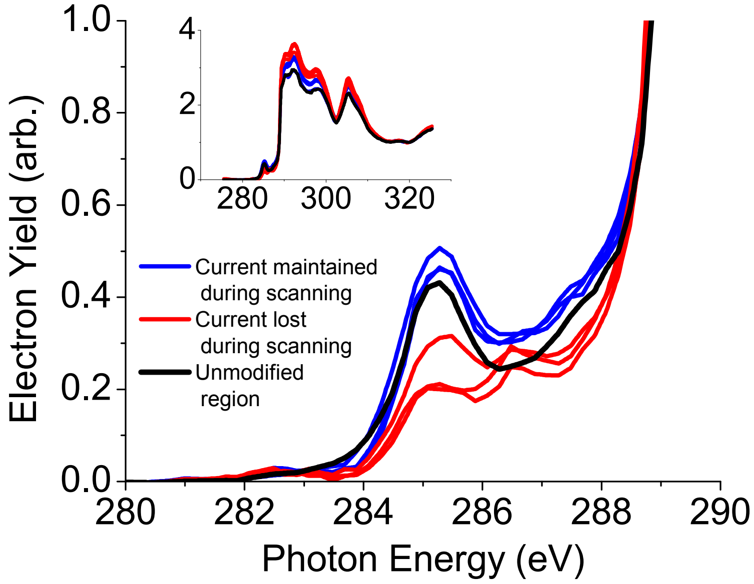

Figure 4.10: C1s NEXAFS data from inside the modified contact region for scans performed with V_m = 10 V and relative humidity from <4 – 45% RH with comparison to an unmodified region. (Blue) Scans in which current persisted during modification and probing scans, (red) scans resulting loss of the Pt probe tip during modification scans, and (black) an unmodified region of N-UNCD are shown. (Inset) The full carbon edge as measured by PEEM.

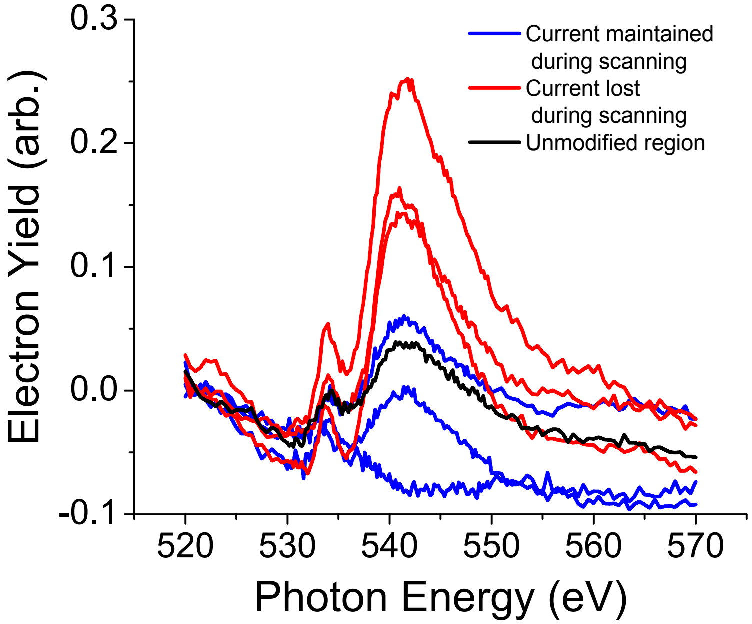

Figure 4.11: O1s NEXAFS data from inside the modified contact region for scans performed with V_m = 10 V and relative humidity from <4 – 45% RH with comparison to an unmodified region. (Blue) Scans in which current persisted during modification and probing scans, (red) scans resulting loss of the Pt probe tip during modification scans, and (black) an unmodified region of N-UNCD are shown.

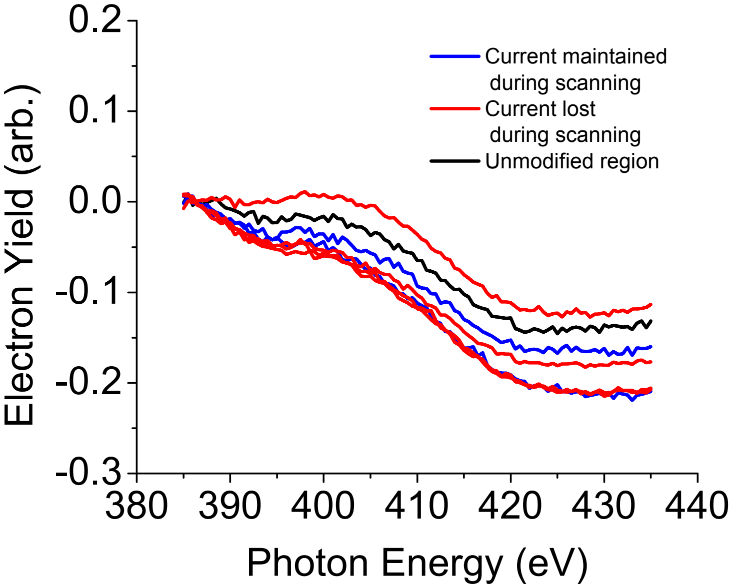

Figure 4.12: N1s NEXAFS data from inside the modified contact region for scans performed with V_m = 10 V and relative humidity from <4 – 45% RH with comparison to an unmodified region. (Blue) Scans in which current persisted during modification and probing scans, (red) scans resulting loss of the Pt probe tip during modification scans, and (black) an unmodified region of N-UNCD are shown.

The spectra shown in figures 4.10 – 4.12 indicate changes to the N-UNCD film only when loss of conductivity between the Pt tip and surface occurred. A transition from 1s-π* bonding (285 eV), which is unique to sp^2-bonded carbon, a decrease in C-O bond signals at 286.7 and 288.6 eV, and the C-H bond signal at 287.5 eV indicate increased oxidation of the N-UNCD when current was lost during scanning. This is corroborated by the increased oxygen peak at ~542 eV when probe tip-surface conductivity was lost. In all cases, no significant changes in nitrogen content of the scanned surface region were observed. These results suggest the loss of Pt coating and exposure/wear of the underlying Si probe material during scanning was the origin of the most dramatic chemical changes. Thus, changes to the N-UNCD film were not observed under load, shear, and electrical bias for load >50 nN when the Pt tip remained intact. Furthermore, degradation of the tip-surface current observed in section 4.2 cannot be attributed to loss nitrogen at the conductive interface and instead indicative of the formation of an insulating surface layer.

CHAPTER 5: CONCLUSIONS AND OPPORTUNITIES

This thesis presented the interrogation of robustness of nanoscale electrical contacts composed of Pt and nitrogen-incorporated ultrananocrystalline diamond (N-UNCD) using atomic force microscopy (AFM) with application to nanoelectromechanical systems (NEMS) logic switches. Pt/Pt single asperity contacts were cycled for up to 2 billion contact events and contact resistance was observed to increase due to the formation and/or transfer of insulating material to the AFM probe tip. Pt/Pt and Pt/N-UNCD contacts were then scanned under load, shear, and electrical bias to show that shear during contact results in higher conductivity, may be used to remove insulating contaminants at the contact, and, in the case of N-UNCD, can lead to insulating contaminant films below a critical contact force.

AFM afforded several advantages for testing electrical contacts for NEMS logic switches. The ubiquity of AFM, which is now a standard technique at most research institutions, means that the methods presented here could be easily adopted by other researchers. The reliance on off-the-shelf components (existing hardware, commercially available AFM probes, standard measurement techniques) for contact testing were used in lieu of time consuming and costly fabrication of devices with new, unproven electrical contact materials. Forces and electrical parameters during testing were prescribed in accordance with those expected at the NEMS logic contact interface.

This chapter briefly summarizes the main observations and contributions of the thesis and relates the findings of this work to an understanding of NEMS logic switch electrical interface degradation at the single asperity level. Section 5.1 summarizes the results of Pt/Pt contact cycling described in chapter 3 and implications for nanoscale NEMS logic switches composed of Pt/Pt interfaces. Section 5.2 summarizes the results of Pt/N-UNCD and Pt/Pt interfaces exposed to load, shear, and electrical power as might be encountered in a wiped electrical contact. Finally, possible extensions of this work are outlined in section 5.3.

5.1 Conclusions: Gigacycle Testing of Single Asperity Platinum/Platinum Contacts using Atomic Force Microscopy

Single asperity Pt/Pt contacts were cycled using AFM in order to mimic repetitive contact of NEMS switch electrical interfaces. The high force sensitivity and sharp probe tip of the AFM technique enabled probing of the electrical interfaces as might be encountered at the most fundamental unit of the the NEMS switch – the single asperity. Cycling of the interface below ~10^5 cycles was achieved using force versus distance (FvD) measurements at ~10 Hz interaction frequency and above 10^5 cycles using amplitude modulated AFM (AM-AFM) at the resonant frequency of the AFM cantilever (~40 – 75 kHz). The combination of these standard AFM techniques permitted 2×10^9 contact cycles to be achieved in a 10-16 hours – a number of interactions that would typically takes days to years using previously demonstrated scanning probe microscopy or nanoindentation testing techniques. Cycling of the interface was periodically slowed so that FvD measurements at a rate of ~0.5 Hz could be taken to interrogate the adhesion and electrical conductivity of the interface with high fidelity. The contact resistance of the Pt/Pt interfaces examined here demonstrated contact resistances that varied over orders of magnitude across the surface of the film. Therefore, a logarithmic current amplifier with a range of several pA to mA was used to measure current while collecting large ensembles of data (25 to 1156 FvD measurements) at each cycling point to provide reasonable statistics of contact resistance. This cycling technique revealed failure mechanisms of Pt/Pt electrical interfaces as they might be encountered in NEMS switches without the need for time-consuming or costly device fabrication.

The presence of a voltage between the Pt/Pt electrical contacts during cycling was investigated to determine if degradation mechanisms of high voltage, prototype NEMS logic devices will differ from that of nanoscale, low-voltage NEMS logic devices. NEMS logic switches are expected operate with a continuous voltage across the source and drain electrodes contacts during cycling (hot switching). The magnitude of this voltage is tied to the size of the device. Decreases in NEMS logic switch size confer faster switching speeds, require lower operating voltages, and result in lower source-drain voltages. Prototype NEMS logic switches have typically utilized source-drain voltages of several volts, however, recent work has been presented for switching using only a few mV [19]. Understanding changes to the electrical contact degradation mechanisms as voltage between the contacts is decreased is, therefore, critical for predicting how the lifetime of NEMS logic devices will vary under device and voltage scaling. With this motivation, cycling was performed in section 3.3 with voltages ranging from 100 mV to 2 V applied across the contacts during cycling.

Packaging NEMS logic switches in inert or hermetic environments adds complexity and cost to fabrication process. The ideal electrical contact would ensure a highly conductive interface upon closure even in the presence of environmental contaminants. In order to investigate the effects of environment on nanoscale electrical contact degradation, testing in section 3.4 was performed in both N_2-purged and laboratory air environments. Voltage between the AFM probe and counter surface was varied between 0 V (mechanical cycling) and 1 V to investigate the effects of environment and electrical power on electrical contact degradation. Mechanical cycling was performed in this study because it represents the ultimate limit of the contribution of just mechanical stress to contact degradation mechanisms.

Of critical need in this work was the use of interaction forces representative of NEMS logic switch interfaces. This requires peak tip-surface interactions from several to hundreds of nN during cycling of the contacts. The application of a voltage between the AFM probe tip and counter surface adds an additional loading term to the tip-surface force interaction during AM-AFM. It was shown that static tip-surface forces due to electrostatic interactions can exceed van der Waals (VDW) tip-surface force contributions for reasonable tip-surface separations, probe dimensions, and voltages (≤2 V) utilized in the cycling experiments in this thesis. However, a dynamic model of the peak interaction stresses during AM-AFM cycling revealed that electrostatic loading only resulted in a maximum variation in peak contact stress of ~13% in comparison to VDW-only solutions for the largest voltages investigated (1 – 2 V). Below a 1 V tip-surface potential, variations in peak contact stress were modest (< 1%). Thus, future investigations performed using AM-AFM cycling of interfaces need not account for electrostatic loading provided tip-surface voltages are maintained below several hundred mV.

Pt/Pt single asperity contacts cycled using static AFM and AM-AFM encountered similar degradation mechanisms during repetitive interaction as has been observed for microscale, multiaperity platinum group metal contacts. Low density TP formation was observed via transmission electron microscopy on the AFM probe tip, was found to dominate contact performance through increases in contact resistance, and was correlated to the number interaction cycles and voltage between the electrical contacts during cycling. In section 3.3, the magnitude of this resistance increase was found to depend on the voltage applied between the contacts during cycling. While the exact mechanism of this TP formation voltage dependence is not understood, it was hypothesized that the presence of a tip-surface voltage during cycling may lead to contact supertemperatures that drive TP production or attract non-local polar species and contaminants in the environment that become adhered to and interact at the contacting interfaces. Despite the uncertainty in the physical mechanism of degradation, the results presented in this thesis suggest that TP formation at nanoscale Pt/Pt electrical contacts decreases as the voltage across the contact decreases. Consequently, NEMS logic switches composed of Pt/Pt interfaces would be expected to experience less TP formation as the source-drain voltage of the device (size of the device) decreases.

Single asperity Pt/Pt contacts cycled in the presence of an electric field demonstrated periods of decreasing contact resistance that were not observed during mechanical cycling. Contact resistance during mechanical cycling increased monotonically and predictably. Regardless of the environment (laboratory air or N_2), hot cycling of Pt/Pt contacts under similar conditions as that of mechanical cycling (*i.e.* similar contact stresses) but with a tip-surface voltage of 1 V resulted in periods of contact resistance increases that were interspersed with periods contact resistance decreases that were not observed during mechanical cycling. In light of recent observations in multiasperity work [52], these periods of decreasing contact resistance were hypothesized to result from field-induced electrical breakdown or temperature-assisted loss of the TP.

The effects of TP formation were most prevalent in humid, aerobic environments (laboratory air) and were significantly inhibited, but still present, in N_2-purged environments. Similar environmental effects have been observed through the controlled addition of various environmental contaminants in sliding electrical contacts [105], microscale electrical contacts cycled in benzene [52], and Au cycled in laboratory and N_2-purged environments [59]. These results demonstrate that minimization of environmental contaminants can have a large impact on contact resistance changes and suggest that packaging of NEMS logic devices in inert and hermetic environments may be necessary to achieve robust electrical contact behavior.

Initial degradation for the largest tip-surface voltages investigated in this thesis during hot cycling (2 V) was notably different from that of cycling under lower voltages. TEM profiles of AFM probes acquired before and after cycling for 2 billion cycles while applying 2 V between the contacts revealed gross deformation of the probe tip geometry not encountered during lower voltage hot cycling. This probe deformation was presumed to occur via ablation or softening and fracture of the tip as a consequence of joule heating. Analysis of the contact supertemperature for the range of typical contact resistances encountered during testing revealed potential contact temperatures up to several thousand ˚C above ambient. The contact resistance and adhesion data during cycling suggested that these gross geometric changes occurred early in the contact lifetime, led to a new equilibrium geometry, and that subsequent cycling of the contact was then dominated by TP formation. This observation is consistent with an ablation or fracture failure. The single asperity hot cycling tests with a 2 V tip-surface voltage infer that the source-drain voltage of NEMS logic switches must scale below 2 V if the electrical contact area of the device approaches the single asperity level in order to avoid potential loss of the electrical contact.

The initial (pre-cycling) contact resistance of the Pt/Pt contacts investigated in this thesis was substantially larger than predicted by theory for clean metal contacts. Pt exposed to laboratory air was found to develop 1.0 – 1.3 nm of C and O contamination within minutes of exposure (potentially less). Contact resistances three to four orders of magnitude larger than predicted by theory was ascribed to this adsorbed, adventitious layer of contamination. This has been routinely observed in microscale contacts exposed to laboratory air [50], [59]. Interestingly, comparison of the initial contact resistance measured in multiasperity tests of Chen *et al*. [50] to that of the single asperity contacts in this work revealed that the discrepancy between the magnitude of contact resistance in each work (3 – 4 Ω for mulitasperity and an average of 10^5 – 10^6 Ω for single asperity) could be almost entirely attributed to the difference in contact area between single and multiasperity tests. This suggests that the effect of adsorbed contaminant layers on contact resistance scales with contact area and even brief exposure of NEMS logic switch electrical interfaces to laboratory air or sources of C and O contamination will result in immediate adsorption of the contaminant material.

In order to sample the average tip-surface interaction, tip-surface conductivity was evaluated at regularly spaced intervals over a 1 x 1 μm^2 area of the Pt counter surface at periodic intervals during cycling. The contact resistance during these measurements varied over a wide range from several kΩ to >5 GΩ (the noise floor of the amplifier) and was described in section 3.2. These large variations in contact resistance were ascribed to adsorbed contamination on the Pt surfaces, the interaction of the single asperity probe tip with the roughness of the counter surface, and, potentially, variations in conductivity of the Pt films resulting from the micro-/nanostructure of the Pt film. The large range of contact resistances measured across the Pt surfaces revealed that fabrication of NEMS logic devices with Pt/Pt interfaces would likely encounter stochastic mechanisms resulting in significant variations in contact resistance for each device. In particular, one could take the measurement of resistance at each surface location as that of a single device in an ensemble of single asperity NEMS logic switch interfaces. These results identify the need for new electrical contact films that do not readily adsorb contaminant layers and/or demonstrate predictable and homogenous conductivity across the surface will be required for NEMS logic switches composed of single asperity contacts.

Adhesion did not vary appreciably with cycling, was lower than predicted for metallic contacts, and supported chemical evidence of an initial C and O contamination layer on the surfaces. Changes to adhesion during cycling were minimal and, in conjunction with before and after cycling TEM profiles, support the observation that contact broadening did not occur in the majority of the tests. The work of adhesion calculated from TEM measurements of the probe tip radii and force of adhesion varied from 9 – 62 mJ/m^2 in section 3.3 to 41 - 460 mJ/m^2 in section 3.4. These work of adhesion values are significantly lower or just approach that expected for metallic contacts and demonstrate that adsorbed contaminant layers of nanoscale thickness can have a dramatic impact on adhesion. The higher work of adhesion observed in section 3.4 was attributed to the lower roughness of the Pt counter surface, which was assumed to be perfectly flat when calculating the work of adhesion. The counter surfaces in section 3.3 were deposited on glass cover slips, which resulted in a root-mean-square (RMS) roughness of ~1.2 nm, whereas those of section 3.4 were deposited on Si resulting in a RMS roughness of ~0.49 nm. Interestingly, the increased roughness of counter surface in section 3.3 resulted in minimal contact resistance penalty. Thus, for NEMS logic switches, engineered roughness of the contact surfaces could enable low adhesion contacts while not sacrificing contact resistance.

The results of this thesis show that to the limit of a single asperity contacts of Pt/Pt, wear will likely not be a considerable concern. Forces of 81 to 390 nN were applied to contacts of 21 to 127 nm radii in contact with rough surfaces and resulting in peak normal contact stresses of 1.2 to 4.4 GPa did not result in wear of the asperity for upwards of 2 billion contact cycles. These results indicate that wear will not be a concern for electrical interfaces interacting at stresses below the hardness of the film.

Finally, it was shown that shear of Pt/Pt interfaces may be used to remove TP formed during cycling and shear loading of the contact leads to lower contact resistance than normal loading of the contact even before TP formation. A Pt probe cycled for $>10^9$ cycles and experiencing a significant increase in contact resistance demonstrated significantly lower contact resistance (in excess of its conductivity before cycling) after rastering across a previously untested Pt surface location. It was also shown that Pt/Pt contacts exposed to normal loading only minutes after shearing of the contact demonstrate considerable increases in contact resistance. This suggests that shear loading of the contact plays a fundamental role in removing adsorbed contaminants that immediately form at the contact interface. These results suggest that shear displacement of the electrical contact interfaces in NEMS logic switches could be used to increase source-drain conductivity during every closure cycle and remove buildup of TP to yield longer effective device lifetimes.

5.2 Conclusions: Subjecting Nitrogen-incorporated Ultrananocrystalline Diamond and Platinum to Load, Shear, and Electrical Bias

Chapter 3 demonstrated that shear of nanoscale Pt/Pt contacts resulted in lower contact resistance than normal loading and could be used to remove TP formed at the contact. With this motivation, Pt/N-UNCD and Pt/Pt contacts were investigated in chapter 4 under extended periods of applied load, shear, and electrical bias using AFM. N-UNCD was investigated as a counter surface because similar diamond films have demonstrated robustness under shear loading in a variety of environments. In this study, Pt-coated AFM probes were laterally rastered across Pt and N-UNCD surfaces under mechanical contact and while applying voltages up to 10 V between the probe tip and counter surface in order to replicate wiping behavior in a NEMS logic switch interface. The behavior of the Pt/N-UNCD interfaces under load, shear, and electrical bias were evaluated in both low humidity (N_2 purged) and high humidity (laboratory air and humidified N_2) environments. In section 4.2, N-UNCD and Pt surfaces were rastered under well-controlled applied loads of 50 nN and 25 nN, respectively. In section 4.3, rastering was performed on N-UNCD surfaces with applied loads starting at 50 nN, which were then allowed to drift to higher loads during the scanning process. Photoemission electron microscopy (PEEM) was then performed in section 4.3 to characterize the chemical identity of the N-UNCD surface after exposure to load, shear, and electrical bias.

Application of a 50 nN applied normal load and electrical bias between Pt-coated AFM probes and N-UNCD counter surfaces overwhelmingly showed increased contact resistance of the interface under repeated scans of a surface. The magnitude this contact resistance increase was shown to depend on the electrical power applied to the contact interface and the surrounding gas environment. Higher electrical power and humid environments led to larger increases in contact resistance. Electrical degradation of the contact interface was also observed to occur immediately at the contact interface or extend beyond the immediate contact zone for voltages larger than 2 V applied between the tip and counter surface for applied normal loads of 50 nN. Scanning of Pt/N-UNCD interfaces under loads set to 50 nN and allowed to increase during scanning up to 60 to 143 nN demonstrated markedly different behavior. For these tests, contact resistance of the Pt/N-UNCD interfaces decreased under high electrical power. Chemical interrogation of N-UNCD regions scanned under ≥50 nN load and high electrical bias (10 V) revealed minimal changes to the structure of the film in absence of wear through or fracture of the Pt-coated probe tip. Interestingly, Pt surfaces rastered with Pt-coated probes exhibited decreasing contact resistance at lower applied normal loads (25 nN). Thus, the generation of a insulating interface was unique to the Pt/N-UNCD contact pair and demonstrates the profound effect of a change in contact material pair can have on electrical interface longevity. Taken in concert, these finding suggest electrical degradation mechanism observed with a 50 nN applied load between Pt/N-UNCD interfaces could be suppressed under increasing and/or high loads.

The results of scanning Pt/N-UNCD surfaces under a range of loads and environments suggest electrical contacts composed of N-UNCD are suitable for low voltage, low power, moderate force, and low humidity electrical applications. Increased contact degradation in humid environments and the observation of minimal changes to the surface chemistry of the N-UNCD film under applied normal loads in excess of 100 nN suggest that electrical degradation of the N-UNCD film investigated here was due to a catalytic reaction that resulted in an insulating surface film. This insulating film was weakly bound to the surface and was removed under sufficient contact force.

5.3 Future Work and Opportunities

The experimental protocols and results described in this thesis demonstrated the utility of AFM for the interrogation of electrical contact materials before time consuming and costly fabrication of NEMS switches with unproven electrical contact materials. Nanoscale electrical contact testing methods utilizing AFM are attractive because they rely on existing, widely-available hardware and off-the-shelf components. Opportunities exist to adapt the protocols described in this thesis to extend the number of contact events from 10^9 to 10^{12} contact cycles in laboratory timeframes and to develop a fundamental understanding of the physical and chemical mechanisms of insulating tribopolymer (TP) formation.

While several billion contact cycles were demonstrated in this thesis, there still exists a large gap between the number of contact cycles required for the demonstration of commercially viable NEMS logic switch electrical contacts ($\sim 10^{16}$) and number of contact cycles achieved here. Furthermore, although the Pt/Pt materials investigated in this thesis demonstrated dramatic increases in contact resistance for $<10^9$ cycles, less reactive materials with superior performance may demonstrate stable contact resistance for $>10^9$ cycles. Two potential solutions exist to increase the number of cycles achieved in laboratory timeframes using AFM. Bimodal AFM techniques that drive dynamic cantilever oscillations at the second resonance of the AFM probe have been demonstrated and are now offered on some commercial AFM systems [124], [125]. With this technique, the AFM cantilever is driven at both its primary and secondary resonances to achieve approximately 6 X the number of interaction cycles typically achieved during AM-AFM measurements. Proksch [124] demonstrated the ability to achieve repulsive tip surface interactions in both the primary and secondary resonance regimes with cantilevers similar to those employed in this thesis. In addition, commercially available AFM probes with higher fundamental (and secondary) resonances (ranging from 300 – 3600 kHz) could be used to achieve 5 – 80 X the number of interaction cycles demonstrated in the work here. The use of bimodal resonance techniques, higher frequency probes, and extended test periods (several days) for promising contact materials would enable the investigation of up to 10^{12} contact cycles using AFM.

The AFM testing protocols developed in this thesis may also be used to understand the fundamental mechanisms that lead to TP formation. Brand *et al*. [52] proposed that the rate of TP formation for microscale electrical contacts of RuO_2 and Pt may be governed by a reaction rate mechanism with the activation energy of TP bond formation dominated by mechanical stress rather than the catalytic potential of the contact materials. However, a recent study investigated various metallic contact material pairs and reported an inverse relationship between the catalytic behavior of the materials and the proclivity for TP formation [49]. Thus, the role of contact material identity and stress on TP formation is still an unsettled question. AFM offers an advantage for studying the effect of stress on TP formation. The true contact area, which determines the mechanical stress at the contact, is obscured by the complex geometric interactions occurring at the microscale, multiasperity contact interfaces that have typically been investigated. Deposition of sufficiently smooth, thin, and conformal contact materials on AFM probes can yield hemispherical probe tips, and in conjunction with low roughness counter surfaces, may be used to prescribe well-controlled contact stresses using the cycling protocols developed here.

BIBLIOGRAPHY

[1] “International technology roadmap for semiconductors (2009 edition),” 2009.

[2] R. H. Blick, H. Qin, H.-S. Kim, and R. Marsland, “A nanomechanical computer - Exploring new avenues of computing,” *New J. Phys.*, vol. 9, p. 241, 2007.

[3] D. A. Czaplewski, G. A. Patrizi, G. M. Kraus, J. R. Wendt, C. D. Nordquist, S. L. Wolfley, M. S. Baker, and M. P. de Boer, “A nanomechanical switch for integration with CMOS logic,” *J. Micromech. Microeng.*, vol. 19, no. 8, p. 085003, Aug. 2009.

[4] “International technology roadmap for semiconductors (2011 edition).” 2011.

[5] “Building energy-efficient ICs from the ground up,” Cadence Design Systems, White paper, 2011.

[6] S. Borkar, “Exponential challenges, exponential rewards - The future of moore’s law,” in *Proceedings of the VLSI-SOC*, Darmstadt, Germany, 2003.

[7] N. S. Kim, T. Austin, D. Baauw, T. Mudge, K. Flautner, J. S. Hu, M. J. Irwin, M. Kandemir, and V. Narayanan, “Leakage current: Moore’s law meets static power,” *Computer*, vol. 36, no. 12, pp. 68–75, 2003.

[8] International Energy Agency and Organisation for Economic Co-operation and Development, *Gadgets and gigawatts: policies for energy efficient electronics*. Paris: OECD/IEA, 2009.

[9] J. M. Climatewire, “Soaring electricity use by new electronic devices imperils climate change efforts,” *The New York Times*, 14-May-2009.

[10] J. G. Koomey, “Estimating total power consumption by servers in the US and the world,” Oakland, CA, 2007.

[11] F. N. Najm, “A survey of power estimation techniques in VLSI circuits,” *IEEE Trans. Very Large Scale Integr. VLSI Syst.*, vol. 2, no. 4, pp. 446–455, 1994.

[12] I. Stojmenovic, *Handbook of Sensor Networks: Algorithms and Architectures*. John Wiley & Sons, 2005.

[13] Z. Guo, N. Sinha, G. Wabiszewski, G. Piazza, R. Carpick, and A. De Hon, “Energy efficient piezoelectric aluminum nitride nano switches for mechanical computing,” in *Government Microcircuit Application & Critical Technology Conference*, Orlando, FL, USA, 2011.

[14] N. Sinha, G. E. Wabiszewski, R. Mahameed, V. V. Felmetsger, S. M. Tanner, R. W. Carpick, and G. Piazza, “Piezoelectric aluminum nitride nanoelectromechanical actuators,” *Appl. Phys. Lett.*, vol. 95, no. 5, pp. 053106–3, 2009.

[15] R. Nathanael, V. Pott, H. Kam, J. Jeon, and T.-J. King Liu, “4-terminal relay technology for complementary logic,” in *2009 IEEE International Electron Devices Meeting (IEDM 2009)*, Piscataway, NJ, USA, 2009.

[16] M. Tabib-Azar, S. R. Venumbaka, K. Alzoubi, and D. Saab, “1 volt, 1 GHz NEMS switches,” presented at the IEEE Sensors, 2010, pp. 1424–1426.

[17] W. W. Jang, J.-B. Yoon, M.-S. Kim, J.-M. Lee, S.-M. Kim, E.-J. Yoon, K. H. Cho, S.-Y. Lee, I.-H. Choi, D.-W. Kim, and D. Park, “NEMS switch with 30 nm-thick beam and 20 nm-thick air-gap for high density non-volatile memory applications,” *Solid State Electron.*, vol. 52, no. 10, pp. 1578–1583, Oct. 2008.

[18] G. Piazza, "Alumimun nitride piezoelectric NEMS resonators and switches," in *Proc. SPIE 7679, Micro- and Nanotechnology Sensors, Systems, and Applications II*, Orlando, FL, USA, 2010, p. 76791L–76791L.

[19] U. Zaghloul and G. Piazza, "10 - 25 nm piezoelectric nano-actuators and NEMS switches for millivolt computational logic," in *IEEE 26th International Conference on Micro Electro Mechanical Systems (MEMS)*, Taipei, Taiwan, 2013, pp. 233–236.

[20] V. Pott, G. L. Chua, R. Vaddi, J. M.-L. Tsai, and T. T. Kim, "The shuttle nanoelectromechanical nonvolatile memory," *IEEE Trans. Electron Devices*, vol. 59, no. 4, pp. 1137–1143, 2012.

[21] Q. Li, S.-M. Koo, M. D. Edelstein, J. S. Suehle, and C. A. Richter, "Silicon nanowire electromechanical switches for logic device application," *Nanotechnology*, vol. 18, no. 31, p. 315202, Aug. 2007.

[22] S. N. Cha, J. E. Jang, Y. Choi, G. A. J. Amaratunga, D.-J. Kang, D. G. Hasko, J. E. Jung, and J. M. Kim, "Fabrication of a nanoelectromechanical switch using a suspended carbon nanotube," *Applied Physics Letters*, vol. 86, no. 8, p. 083105, 2005.

[23] S. W. Lee, D. S. Lee, R. E. Morjan, S. H. Jhang, M. Sveningsson, O. A. Nerushev, Y. W. Park, and E. E. B. Campbell, "A three-terminal carbon nanorelay," *Nano Lett.*, vol. 4, no. 10, pp. 2027–2030, Oct. 2004.

[24] O. Loh, X. Wei, C. Ke, J. Sullivan, and H. D. Espinosa, "Robust carbon-nanotube-based nano-electromechanical devices: Understanding and eliminating prevalent failure modes using alternative electrode materials," *Small*, vol. 7, no. 1, pp. 79–86, Jan. 2011.

[25] S. M. Kim, E. B. Song, S. Lee, S. Seo, D. H. Seo, Y. Hwang, R. Candler, and K. L. Wang, "Suspended few-layer graphene beam electromechanical switch with abrupt on-off characteristics and minimal leakage current," *Applied Physics Letters*, vol. 99, no. 2, pp. 023103–023103–3, Jul. 2011.

[26] G. E. Moore, "Cramming more components onto integrated circuits," *Proceedings of the IEEE*, vol. 86, no. 1, pp. 82–85, Jan. 1998.

[27] B. Calhoun, "Digital circuit design challenges and opportunities in the era of nanoscale cmos," *Proceedings of the IEEE (Special Issue on Integrated Electronics: Beyond Moore's Law)*, vol. 96, pp. 343–365, 2008.

[28] J. D. Meindl, Q. Chen, and J. A. Davis, "Limits on silicon nanoelectronics for terascale integration," *Science*, vol. 293, no. 5537, pp. 2044–2049, Sep. 2001.

[29] J. A. . Hutchby, G. I. . Bourianoff, V. V. . Zhirnov, and J. E. . Brewer, "Extending the road beyond CMOS," *IEEE Circuits and Devices Magazine*, vol. 18, no. 2, pp. 28–41, Mar. 2002.

[30] H. F. Dadgour and K. Banerjee, "Hybrid NEMS–CMOS integrated circuits: a novel strategy for energy-efficient designs," *IET Computers & Digital Techniques*, vol. 3, no. 6, p. 593, 2009.

[31] O. Y. Loh and H. D. Espinosa, "Nanoelectromechanical contact switches," *Nature Nanotechnology*, vol. 7, no. 5, pp. 283–295, 2012.

[32] F. Chen, H. Kam, D. Markovic, T. J. K. Liu, V. Stojanovic, and E. Alon, "Integrated circuit design with NEM relays," in *Proceedings of the 2008 IEEE/ACM International Conference on Computer-Aided Design*, 2008, pp. 750–757.

[33] D. A. Czaplewski, G. M. Kraus, and C. D. Nordquist, "Nanomechanical switches for power saving in CMOS applications," *Electronics Letters*, vol. 45, no. 11, pp. 550–551, 2009.

[34] V. Pott, Hei Kam, R. Nathanael, Jaeseok Jeon, E. Alon, and Tsu-Jae King Liu, “Mechanical computing redux: Relays for integrated circuit applications,” *Proceedings of the IEEE*, vol. 98, no. 12, pp. 2076–2094, Dec. 2010.

[35] M. Spencer, F. Chen, C. C. Wang, R. Nathanael, H. Fariborzi, A. Gupta, H. Kam, V. Pott, J. Jeon, T.-J. K. Liu, D. Markovic, E. Alon, and V. Stojanovic, “Demonstration of integrated micro-electro-mechanical relay circuits for VLSI applications,” *IEEE Journal of Solid-State Circuits*, vol. 46, no. 1, pp. 308–320, Jan. 2011.

[36] K. Akarvardar, D. Elata, R. Parsa, G. C. Wan, K. Yoo, J. Provine, P. Peumans, R. T. Howe, and H.-S. Wong, “Design considerations for complementary nanoelectromechanical logic gates,” in *Electron Devices Meeting, 2007. IEDM 2007. IEEE International*, 2007, pp. 299–302.

[37] A. M. Ionescu, V. Pott, R. Fritschi, K. Banerjee, M. J. Declercq, P. Renaud, C. Hibert, P. Fluckiger, and G. A. Racine, “Modeling and design of a low-voltage SOI suspended-gate MOSFET (SG-MOSFET) with a metal-over-gate architecture,” in *Quality Electronic Design, 2002. Proceedings. International Symposium on*, 2002, pp. 496–501.

[38] N. Sinha, T. S. Jones, Z. Guo, and G. Piazza, “Body-biased complementary logic implemented using aln piezoelectric MEMS switches,” *Journal of Microelectromechanical Systems*, vol. 21, no. 2, pp. 484–496, 2012.

[39] F. Fallah and M. Pedram, “Standby and active leakage current control and minimization in cmos vlsi circuits,” *IEICE Transactions on Electronics*, vol. E88–C, no. 4, pp. 509–519, Apr. 2005.

[40] E. Yablonovitch, “There are orders-of-magnitude power advantages in complementing the transistor with a milli-volt switch,” presented at the MTO Symposium, San Jose, CA, USA, 07-Mar-2007.

[41] N. Abele, R. Fritschi, K. Boucart, F. Casset, P. Ancey, and A.-M. Ionescu, “Suspended-gate MOSFET: bringing new MEMS functionality into solid-state MOS transistor,” in *Electron Devices Meeting, 2005. IEDM Technical Digest. IEEE International*, 2005, pp. 479–481.

[42] S.-W. Lee, R. W. Johnstone, and A. M. Parameswaran, “MEMS mechanical logic units: characterization and improvements of devices fabricated with MicraGEM and PolyMUMPs,” 2005, p. 60371A–60371A–10.

[43] T.-H. Lee, S. Bhunia, and M. Mehregany, “Electromechanical computing at 500 C with silicon carbide,” *Science*, vol. 329, no. 5997, pp. 1316–1318, Sep. 2010.

[44] C. Chen, R. Parsa, N. Patil, S. Chong, K. Akarvardar, J. Provine, D. Lewis, J. Watt, R. T. Howe, H. S. P. Wong, and others, “Efficient FPGAs using nanoelectromechanical relays,” in *Proceedings of the 18th Annual Acm/Sigda International Symposium on Field Programmable Gate Arrays*, 2010, pp. 273–282.

[45] Y. Zhou, S. Thekkel, and S. Bhunia, “Low power FPGA design using hybrid CMOS-NEMS approach,” in *Proceedings of the 2007 international symposium on Low power electronics and design*, 2007, pp. 14–19.

[46] W. Y. Choi, Hei Kam, D. Lee, J. Lai, and T.-J. King Liu, “Compact nano-electro-mechanical non-volatile memory (NEMory) for 3D integration,” in *2007 IEEE International Electron Devices Meeting (IEDM 2007)*, Washington, DC, USA, 2007, pp. 603–6.

[47] S. Fujita, K. Nomura, K. Abe, and T. H. Lee, “3-d nanoarchitectures with carbon nanotube mechanical switches for future on-chip network beyond cmos architecture,” *IEEE Transactions on Circuits and Systems I: Regular Papers*, vol. 54, no. 11, pp. 2472–2479, Nov. 2007.

[48] B. Charlot, W. Sun, K. Yamashita, H. Fujita, and H. Toshiyoshi, “Bistable nanowire for micromechanical memory,” *J. Micromech. Microeng.*, vol. 18, no. 4, p. 045005, Apr. 2008.

[49] D. A. Czaplewski, C. D. Nordquist, C. W. Dyck, G. A. Patrizi, G. M. Kraus, and W. D. Cowan, “Lifetime limitations of ohmic, contacting RF MEMS switches with Au, Pt and Ir contact materials due to accumulation of ‘friction polymer’ on the contacts,” *J. Micromech. Microeng.*, vol. 22, no. 10, p. 105005, Oct. 2012.

[50] L. Chen, H. Lee, Z. J. Guo, N. E. McGruer, K. W. Gilbert, S. Mall, K. D. Leedy, and G. G. Adams, “Contact resistance study of noble metals and alloy films using a scanning probe microscope test station,” *J. Appl. Phys.*, vol. 102, no. 7, pp. 074910–1, Oct. 2007.

[51] R. A. Coutu Jr., P. E. Kladitis, K. D. Leedy, and R. L. Crane, “Selecting metal alloy electric contact materials for MEMS switches,” *J. Micromech. Microeng.*, vol. 14, no. 8, pp. 1157–1164, 2004.

[52] V. Brand, M. S. Baker, and M. P. Boer, “Impact of contact materials and operating conditions on stability of micromechanical switches,” *Tribol. Lett.*, Jun. 2013.

[53] H. Kwon, D.-J. Choi, J.-H. Park, H.-C. Lee, Y.-H. Park, Y.-D. Kim, H.-J. Nam, Y.-C. Joo, and J.-U. Bu, “Contact materials and reliability for high power RF-MEMS switches,” in *20th IEEE International Conference on Micro Electro Mechanical Systems (MEMS 2007)*, Piscataway, NJ 08855-1331, United States, 2007, pp. 231–234.

[54] G. M. Rebeiz, *RF MEMS : theory, design, and technology*. Hoboken, NJ: J. Wiley, 2003.

[55] H. S. Newman, J. L. Ebel, D. Judy, and J. Maciel, “Lifetime measurements on a high-reliability RF-MEMS contact switch,” *IEEE Microwave and Wireless Components Letters*, vol. 18, no. 2, pp. 100–2, Feb. 2008.

[56] P. G. Slade, Ed., *Electrical Contacts: Principles and Applications*, 1st ed. CRC Press, 1999.

[57] Z. Yang, D. Lichtenwalner, A. Morris, J. Krim, and A. I. Kingon, “Contact degradation in hot/cold operation of direct contact micro-switches,” *Journal of Micromechanics and Microengineering*, vol. 20, no. 10, 2010.

[58] L. Chen, Z. J. Guo, N. Joshi, H. Eid, G. G. Adams, and N. E. McGruer, “An improved SPM-based contact tester for the study of microcontacts,” *Journal of Micromechanics and Microengineering*, vol. 22, no. 4, p. 045017, Apr. 2012.

[59] D. J. Dickrell and M. T. Dugger, “Electrical contact resistance degradation of a hot-switched simulated metal MEMS contact,” *IEEE Transactions on Components and Packaging Technologies*, vol. 30, no. 1, pp. 75–80, Mar. 2007.

[60] G. Binnig, C. F. Quate, and C. Gerber, “Atomic force microscope,” *Phys. Rev. Lett.*, vol. 56, no. 9, p. 930, Mar. 1986.

[61] Ben Ohler, “Practical advice on the determination of cantilever spring constants,” *Veeco Application Notes*, 2007.

[62] J. L. Hutter and J. Bechhoefer, “Calibration of atomic-force microscope tips,” *Rev. Sci. Instrum.*, vol. 64, no. 7, p. 1868, 1993.

[63] J. E. Sader, J. W. M. Chon, and P. Mulvaney, “Calibration of rectangular atomic force microscope cantilevers,” *Rev. Sci. Instrum.*, vol. 70, no. 10, pp. 3967–3969, 1999.

[64] D. A. Walters, J. P. Cleveland, N. H. Thomson, P. K. Hansma, M. A. Wendman, G. Gurley, and V. Elings, “Short cantilevers for atomic force microscopy,” *Rev. Sci. Instrum.*, vol. 67, no. 10, p. 3583, 1996.

[65] H. Butt and M. Jaschke, “Calculation of thermal noise in atomic force microscopy,” *Nanotechnology*, vol. 6, pp. 1–7, 1995.

[66] E. Meyer, H. J. Hug, and R. Bennewitz, *Scanning Probe Microscopy: The Lab on a Tip*. Springer, 2004.

[67] R. Garcia and R. Perez, “Dynamic atomic force microscopy methods,” *Surf. Sci. Rep.*, vol. 47, no. 6–8, pp. 197–301, 2002.

[68] R. Garcia and A. San Paulo, “Attractive and repulsive tip-sample interaction regimes in tapping-mode atomic force microscopy,” *Phys. Rev. B: Condens. Matter*, vol. 60, no. 7, pp. 4961–7, 1999.

[69] X. Xu, C. Carrasco, P. Depablo, J. Gomezherrero, and A. Raman, “Unmasking imaging forces on soft biological samples in liquids when using dynamic atomic force microscopy: a case study on viral capsids,” *Biophys. J.*, vol. 95, no. 5, pp. 2520–2528, Sep. 2008.

[70] V. Vahdat, D. S. Grierson, K. T. Turner, and R. W. Carpick, “Mechanics of Interaction and Atomic-Scale Wear of Amplitude Modulation Atomic Force Microscopy Probes,” *ACS Nano*, vol. 7, no. 4, pp. 3221–3235, Apr. 2013.

[71] S. Hu and A. Raman, “Analytical formulas and scaling laws for peak interaction forces in dynamic atomic force microscopy,” *Appl. Phys. Lett.*, vol. 91, no. 12, p. 123106, 2007.

[72] J. Melcher, D. Kiracofe, and S. Hu, “VEDA 2.0 (Virtual Environment for Dynamic AFM).” 2012.

[73] O. Cherniavskaya, L. Chen, V. Weng, L. Yuditsky, and L. E. Brus, “Quantitative noncontact electrostatic force imaging of nanocrystal polarizability,” *J. Phys. Chem. B*, vol. 107, no. 7, pp. 1525–1531, Feb. 2003.

[74] S. Patil, A. V. Kulkarni, and C. V. Dharmadhikari, “Study of the electrostatic force between a conducting tip in proximity with a metallic surface: Theory and experiment,” *J. Appl. Phys.*, vol. 88, no. 11, p. 6940, 2000.

[75] S. Hudlet, M. Saint Jean, C. Guthmann, and J. Berger, “Evaluation of the capacitive force between an atomic force microscopy tip and a metallic surface,” *Eur. Phys. J. B*, vol. 2, p. 5, Mar. 1998.

[76] B. Law and F. Rieutord, “Electrostatic forces in atomic force microscopy,” *Phys. Rev. B: Condens. Matter*, vol. 66, no. 3, Jun. 2002.

[77] W. N. Sharpe Jr., *Springer Handbook of Experimental Solid Mechanics*. Springer, 2008.

[78] K. L. Johnson, K. Kendall, and A. D. Roberts, “Surface energy and the contact of elastic solids,” *Proceedings of the Royal Society of London. Series A, Mathematical and Physical Sciences*, vol. 324, no. 1558, pp. 301–313, Sep. 1971.

[79] D. S. Grierson, E. E. Flater, and R. W. Carpick, “Accounting for the JKR–DMT transition in adhesion and friction measurements with atomic force microscopy,” *J. Adhes. Sci. Technol.*, vol. 19, no. 3, pp. 291–311, Mar. 2005.

[80] J. N. Israelachvili, *Intermolecular and Surface Forces*, 3rd ed. Academic Press, 2010.

[81] J. Liu, J. K. Notbohm, R. W. Carpick, and K. T. Turner, “Method for characterizing nanoscale wear of atomic force microscope tips,” *ACS Nano*, vol. 4, no. 7, pp. 3763–3772, Jul. 2010.

[82] J. Liu, D. S. Grierson, N. Moldovan, J. Notbohm, S. Li, P. Jaroenapibal, S. D. O’Connor, A. V. Sumant, N. Neelakantan, J. A. Carlisle, K. T. Turner, and R. W. Carpick, “Preventing nanoscale wear of atomic force microscopy tips through the use of monolithic ultrananocrystalline diamond probes,” *Small*, vol. 6, no. 10, pp. 1140–1149, May 2010.

[83] H. Lo and J. A. Bain, “Effects of high current density at nanoscale point contacts,” in *1st ASME Micro/Nanoscale Heat Transfer International Conference, MNHT08, January 6, 2008 - January 9, 2008*, Tainan, Taiwan, 2008, vol. PART A, pp. 493–502.

[84] D. P. Burt, N. R. Wilson, J. M. R. Weaver, P. S. Dobson, and J. V. Macpherson, “Nanowire probes for high resolution combined scanning electrochemical microscopy − atomic force microscopy,” *Nano Lett.*, vol. 5, no. 4, pp. 639–643, Apr. 2005.

[85] K.-H. Chung, Y.-H. Lee, and D.-E. Kim, “Characteristics of fracture during the approach process and wear mechanism of a silicon AFM tip,” *Ultramicroscopy*, vol. 102, no. 2, pp. 161–171, Jan. 2005.

[86] K.-H. Chung and D.-E. Kim, “Wear characteristics of diamond-coated atomic force microscope probe,” *Ultramicroscopy*, vol. 108, no. 1, pp. 1–10, Dec. 2007.

[87] B. Haochih Liu and C.-H. Chen, “Direct deformation study of AFM probe tips modified by hydrophobic alkylsilane self-assembled monolayers,” *Ultramicroscopy*, vol. 111, no. 8, pp. 1124–1130, Jul. 2011.

[88] G. Huttl, V. Klemm, R. Popp, F. Simon, and E. Muller, “Tailored colloidal AFM probes and their TEM investigation,” *Surf. Interface Anal.*, vol. 33, no. 2, pp. 50–53, Feb. 2002.

[89] D. L. Sedin and K. L. Rowlen, “Influence of tip size on AFM roughness measurements,” *Appl. Surf. Sci.*, vol. 182, no. 1, pp. 40–48, 2001.

[90] J. F. Watts and J. Wolstenholme, *An Introduction to Surface Analysis by XPS and AES*. Wiley, 2003.

[91] F. Mangolini, J. Åhlund, G. E. Wabiszewski, V. P. Adiga, P. Egberts, F. Streller, K. Backlund, P. G. Karlsson, B. Wannberg, and R. W. Carpick, “Angle-resolved environmental X-ray photoelectron spectroscopy: A new laboratory setup for photoemission studies at pressures up to 0.4 Torr,” *Rev. Sci. Instrum.*, vol. 83, no. 9, pp. 093112–093112–10, Sep. 2012.

[92] D. Briggs and J. T. Grant, *Surface Analysis by Auger and X-Ray Photoelectron Spectroscopy*. SurfaceSpectra, 2003.

[93] C. S. Fadley, “Solid state-and surface-analysis by means of angular-dependent X-ray photoelectron spectroscopy,” *Prog. Solid State Chem.*, vol. 11, pp. 265–343, 1976.

[94] M. Olla, G. Navarra, B. Elsener, and A. Rossi, “Nondestructive in-depth composition profile of oxy-hydroxide nanolayers on iron surfaces from ARXPS measurement,” *Surf. Interface Anal.*, vol. 38, no. 5, pp. 964–974, 2006.

[95] J. Scofield, “Hartree-Slater subshell photoionization cross-sections at 1254 and 1487 eV,” *J. Electron. Spectrosc. Relat. Phenom.*, vol. 8, no. 2, pp. 129–137, 1976.

[96] R. F. Reilman, A. Msezane, and S. T. Manson, “Relative intensities in photoelectron spectroscopy of atoms and molecules,” *J. Electron. Spectrosc. Relat. Phenom.*, vol. 8, no. 5, pp. 389–394, 1976.

[97] S. Anders, H. A. Padmore, R. M. Duarte, T. Renner, T. Stammler, A. Scholl, M. R. Scheinfein, J. Stohr, L. Seve, and B. Sinkovic, “Photoemission electron microscope for the study of magnetic materials,” *Rev. Sci. Instrum.*, vol. 70, no. 10, pp. 3973–3981, 1999.

[98] A. R. Konicek, D. S. Grierson, A. V. Sumant, T. A. Friedmann, J. P. Sullivan, P. U. P. A. Gilbert, W. G. Sawyer, and R. W. Carpick, “Influence of surface passivation on the friction and wear behavior of ultrananocrystalline diamond and tetrahedral amorphous carbon thin films,” *Phys. Rev. B*, vol. 85, no. 15, p. 155448, Apr. 2012.

[99] A. R. Konicek, “Tribochemical studies of hard carbon films as a function of load and environment,” University of Pennsylvania, Philadelphia, PA, 2010.

[100] S. Bhattacharyya, O. Auciello, J. Birrell, J. A. Carlisie, L. A. Curtiss, A. N. Goyette, D. M. Gruen, A. R. Krauss, J. Schlueter, A. Sumant, and P. Zapol, “Synthesis and characterization of highly-conducting nitrogen-doped ultrananocrystalline diamond films,” *Appl. Phys. Lett.*, vol. 79, no. 10, p. 1441, 2001.

[101] J. E. Gerbi, O. Auciello, J. Birrell, D. M. Gruen, B. W. Alphenaar, and J. A. Carlisle, “Electrical contacts to ultrananocrystalline diamond,” *Appl. Phys. Lett.*, vol. 83, no. 10, pp. 2001–3, Sep. 2003.

[102] R. Fuierer, “Asylum research MFP-3D procedural ‘manualette’ ver. 10.5.”Asylum Research, Santa Barbara, CA, Oct-2009.

[103] R. J. Cannara, M. J. Brukman, and R. W. Carpick, “Cantilever tilt compensation for variable-load atomic force microscopy,” *Rev. Sci. Instrum.*, vol. 76, no. 5, p. 053706, 2005.

[104] Nipun Sinha, “Piezoelectric aluminum nitride dual-beam relays for mechanical computing,” University of Pennsylvania, Philadelphia, PA, 2011.

[105] H. W. Hermance and T. F. Egan, “Organic deposits on precious metal contacts,” *Bell System Technical Journal*, vol. 37, no. 3, pp. 739–776, May 1958.

[106] S. Morgenthaler, “Surface-chemical gradients,” ETH Zurich, Zurich, Switzerland, 2007.

[107] S. Jeedigunta, P. Spagnol, J. Bumgarner, and A. Kumar, “Electrical contacts to nitrogen incorporated nanocrystalline diamond films,” *Diamond Relat. Mater.*, vol. 17, no. 12, pp. 2037–2040, Dec. 2008.

[108] N. Sinha, T. Jones, Z. Guo, and G. Piazza, “Demonstration of low voltage and functionally complete logic operations using body-biased complementary and ultra-thin ALN piezoelectric mechanical switches,” in *2010 IEEE 23rd International Conference on Micro Electro Mechanical Systems (MEMS)*, 2010, pp. 751–754.

[109] H. Bruzzone, “On the effect of finite closure time of switches in electrical circuits with fast transient behavior,” *Am. J. Phys*, vol. 57, no. 1, p. 63, 1989.

[110] B. Nikolic and P. B. Allen, “Electron transport through a circular constriction,” *Phys. Rev. B: Condens. Matter*, vol. 60, no. 6, pp. 3963–9, 1999.

[111] P. J. Cumpson and M. P. Seah, “Stability of reference masses. IV: Growth of carbonaceous contamination on platinum-iridium alloy surfaces, and cleaning by UV/ozone treatment,” *Metrologia*, vol. 33, p. 507, 1996.

[112] M. Enachescu, R. W. Carpick, D. F. Ogletree, and M. Salmeron, “The role of contaminants in the variation of adhesion, friction, and electrical conduction properties of carbide-coated scanning probe tips and Pt(111) in ultrahigh vacuum,” *J. Appl. Phys.*, vol. 95, no. 12, pp. 7694–7700, Jun. 2004.

[113] J. Israelachvili, *Intermolecular and surface forces*, 2nd ed. San Diego: Academic Press, 1992.

[114] V. Vahdat, D. S. Grierson, K. T. Turner, and R. W. Carpick, “Mechanics of interaction and atomic-scale wear of amplitude modulation atomic force microscopy probes,” *ACS Nano*, vol. 7, no. 4, pp. 3221–3235, Apr. 2013.

[115] T. D. B. Jacobs, B. Gotsmann, M. A. Lantz, and R. W. Carpick, “On the application of transition state theory to atomic-scale wear,” *Tribol. Lett.*, vol. 39, pp. 257–271, Jul. 2010.

[116] J. Schimkat, “Contact measurements providing basic design data for microrelay actuators,” *Sens. Actuators, A*, vol. 73, no. 1–2, pp. 138–143, 1999.

[117] J. Andzane, N. Petkov, A. I. Livshits, J. J. Boland, J. D. Holmes, and D. Erts, “Two-terminal nanoelectromechanical devices based on germanium nanowires,” *Nano Lett.*, vol. 9, no. 5, pp. 1824–1829, May 2009.

[118] R. Holm, *Electric Contacts: Theory and Application*. Springer, 2010.

[119] T. D. B. Jacobs, K. E. Ryan, P. L. Keating, D. S. Grierson, J. A. Lefever, K. T. Turner, J. A. Harrison, and R. W. Carpick, “The effect of atomic-scale roughness on the adhesion of nanoscale asperities: a combined simulation and experimental investigation,” *Tribol. Lett.*, vol. 50, no. 1, pp. 81–93, Apr. 2013.

[120] S. Srinivasan, J. Hiller, B. Kabius, and O. Auciello, “Piezoelectric/ultrananocrystalline diamond heterostructures for high-performance multifunctional micro/nanoelectromechanical systems,” *Appl. Phys. Lett.*, vol. 90, no. 13, p. 134101, 2007.

[121] A.R. Konicek, D.S. Grierson, P.U.P.A. Gilbert, W.G. Sawyer, A.V. Sumant, and R.W. Carpick, “Origin of ultralow friction and wear in ultrananocrystalline diamond,” *Phys. Rev. Lett.*, vol. 100, no. 23, p. 235502, Jun. 2008.

[122] Li Shi and A. Majumdar, “Thermal transport mechanisms at nanoscale point contacts,” *J. Heat Transfer*, vol. 124, no. 2, pp. 329–37, Apr. 2002.

[123] B. L. Weeks, M. W. Vaughn, and J. J. DeYoreo, “Direct imaging of meniscus formation in atomic force microscopy using environmental scanning electron microscopy,” *Langmuir*, vol. 21, no. 18, pp. 8096–8098, Aug. 2005.

[124] R. Proksch, “Multifrequency, repulsive-mode amplitude-modulated atomic force microscopy,” *Appl. Phys. Lett.*, vol. 89, no. 11, p. 113121, 2006.

[125] M. Baumann and R. W. Stark, “Dual frequency atomic force microscopy on charged surfaces,” *Ultramicroscopy*, vol. 110, no. 6, pp. 578–581, May 2010.